Non-synchronous Phenomena in Turbomachines

Christoph Brandstetter

Université Claude Bernard Lyon 1

ÉCOLE CENTRALE LYON

Numéro d'ordre : 2022

Habilitation de Recherche

Spécialité : Mécanique des Fluides

Soutenue publiquement le 28 mars 2022, par :

Christoph Stefan BRANDSTETTER

Non-synchronous Phenomena in Turbomachines

Devant le jury composé de :

Nicolas Cumpsty,	Emerit. Prof.	Imperial College, University of Cambridge, MIT
Roque Corral,	Professeur	Universidad Politécnica de Madrid
Nicolas Binder,	Professeur	ISAE-SUPAERO, ENSICA
Jean-Philippe Matas,	Professeur	LMFA, Université Claude Bernard Lyon I
Xavier Ottavy,	Directeur de Recherche, HDR	CNRS, LMFA, Ecole Centrale de Lyon

Thanks

The work presented in this manuscript would not have been possible without the invaluable contributions of a large and dedicated research group. It is difficult to adequately express my gratitude to everyone involved.

None of these results could have been achieved without the exceptional team that Xavier Ottavy assembled in Lyon. Xavier's specific way of leading such a strong and cohesive team is truly exemplary. He maintains the group spirit and is always of great personal and professional help. His support and guidance helped me to find my place in Lyon.

This gratitude also extends to Benoit Paoletti, who leads our technical team. The world-class test facility and methods he developed and built is outstanding. All our work is dependent on reliable data, and Benoit is the main reason that I have the confidence to pursue experimentally ambitious projects.

The core of this work concerns aeroelasticity, which I didn't even consider working on before I met Sina Stapelfeldt of Imperial College. Over the last decade, she taught me most of what I know today about all types of Fluid-Structure interaction, modeling and numerics. Without her enduring support in understanding physics, preparing and leading projects, writing papers, repairing my bad English and doubting my often overly ambitious approaches, I may have left the field long ago.

It has been a genuine pleasure to collaborate over the years with the core of our group around Gilbert Halter, Pierre Laucher, Lionel Pierrard, Sebastien Goguey, Cedric Desbois and Fatima El-Boukhrissi. Their expertise, reliability and friendship have been invaluable, and I am immensely thankful for their support and for welcoming me into their team. Sylvie Rault was of great help during the hard times of project acquisition and I still miss her support.

I would like to extend my special thanks to Anne-Lise Fiquet, who recently became an integral part of this group. While I had the privilege of supporting her during the supervision of her thesis—much of which forms the a main part of this manuscript—she was often already ahead of me in many respects.

The thesis of Valdo Pages is highly appreciated. Valdo did a great work in the aerodynamic and structural design of the test case ECL5. His thesis was directed by Stéphane Aubert and Pascal Ferrand of LMFA, and supported by Laurent Jablonsky from Safran Aircraft Engines. Regular exchanges with Alexis Giauque, Pierre Duquesne, Jerome Boudet and Isabelle Trebinjac of LMFA was of great value for this project. I express my gratitude to this constructive collaboration which builds the basis for ongoing projects. This extends to the general support of the aerodynamic and aeroelastic team of Safran Aircraft Engines, both on the technical and financial side.

The entirety of our projects was continuosly supported by the laboratory director Christoph Bailly and our research director Christoph Corre. To both, I would like to express my thanks for the professional advise and technical discussions that have been elementary.

I would like to thank Heinz-Peter Schiffer in Darmstadt for giving me the opportunity for post-doctoral research before I went to Lyon. The excellent work of Maximilian Jüngst has led to results presented here and the development of a new test facility with Jan Werner and Christian Kunkel helped me to advance on the methods to investigate aeroelastic phenomena. I am grateful that we still have regular exchanges between our laboratories and would like to particularly mention the ongoing collaboration with Fabian Klausmann, who develops optical methods which go beyond our current capabilities.

Special thanks go to all of our PhD students and interns who participate either directly to the technical work presented here, or by maintaining the great ambiance in our labo-

ratory. I am happy that Alexandra Schneider and Florent Kravtsoff are still working with us as post-doctoral researchers and keep the group together. I would like to thank Gabriel Mondin, Martin Rodrigues and Victor Moenne-Loccoz, who we lost to our industry partners, for the technical discussions and the good time we had. This list could go on for pages, and I excuse myself to all that should have been mentioned above, specifically the members of our laboratory.

Particular thanks go to the reviewers of this work. Nicolas Cumpsty of Imperial College gave me invaluable advise throughout the past years. In great detail, Prof. Cumpsty dug into our work and provided us with the most reliable and critical reviews, and I am very grateful for the extensive discussions we had. The same thanks go to Nicolas Binder of ISAE and Roque Corral of UP-Madrid who agreed to review this manuscript, and Jean-Philippe Matas of Lyon 1 for being a member of the jury. I am delighted that you all took the time.

Finally, thank you Nina, Anna and Philipp for always being there for me, enduring me coming home late, tired and angry and building me up again when it was too much. I am incredibly happy that we found a new home in France and you made this very easy. Without you, none of this would be possible.

Acknowledgements Our research group is grateful for the continuous collaboration and financial support of SAFRAN Aircraft Engines since the beginning of project CATANA, for which the test module MARLYSA was provided by SAFRAN.

The experimental research was financed through the European Union's Clean Sky 2 Joint Undertaking (JU) under grant agreement N864719, CATANA. The JU receives support from the European Union's Horizon 2020 research and innovation program and the Clean Sky 2 JU members other than the Union. The paper reflects only the author's view and the JU is not responsible for any use that may be made of the information it contains.

Assessment of the test facility was enabled through financial supports of Agence Nationale de la Recherche (ANR, Project d'EquipEx PHARE) and Conseil pour la Recherche Aeronautique Civile (CORAC - Programme CUMIN). Buildings and infrastructure were supported by ECL, instrumentation supported by Institut Carnot (INGENIERIE@LYON - Project MERIT) and SAFRAN Aircraft Engines.

Non-synchronous Phenomena in Turbomachines

Christoph Brandstetter

December 2021

Contents

Chapter 1

Introduction

1.1 Context

One of the main technological challenges of the present day is the sustainable use of primary energy sources. In the field of aerospace propulsion, no alternative to turbo-engines will be available within the next few decades, and regardless of their application, the efficiency of energy conversion systems is of utmost societal interest. Engines of the future must be efficient during flexible operation while emitting minimal pollutant gases and noise. A key factor to achieve these goals is to build larger turbojet engines to maximize the bypass flow while reducing the core size.

A step changing progress in the development of quiet and efficient jet engines has been enabled in the last decade with the availability of lightweight gearboxes, capable to transmit the power from the low-pressure turbine to the fan. This allows to increase the diameter of the fan and to optimize it independently from the required rotation speed of the turbine, enabling higher bypass mass flow at reduced pressure ratio and relative speeds which is beneficial for compression efficiency and noise generation. To avoid additional weight induced by larger fan blades, high-performant composite materials are necessary to fully exploit this potential.

Research has shown that with the application of modern lightweight blade geometries aeroelastic coupling phenomena tend to reduce the operating range of compressors and fans, leading to designs which may not operate at optimal thermodynamic conditions. Long established design criteria which result partly from semi-empirical studies are not transferable to the novel technology, particularly concerning fluid-structural interaction mechanisms. The interdependency between fluid and structure requires the application of integrated design procedures which need to be validated through fundamental understanding of physical aeroelastic and aeroacoustic coupling phenomena.

The current design process for turbojet engines employs advanced computational methods and delivers systems with high maximum efficiency at design condition. However, the understanding of phenomena at off-design conditions is still poor and their prediction is extremely inaccurate.

Off-design operation is a prevalent factor during short- and medium distance flights and inherent to stationary gas-turbines used to cover peak-loads in the electricity grid. Past research has revealed a strong interdependency of aerodynamics, mechanics and acoustics in this operating range. This interdependency affects the performance, limits the operating range and is not robustly predictable. Although models considering each of the sub-disciplines individually have been successfully validated and applied, current approaches fail to predict periodic and transient phenomena in the highly coupled system. Multi-physical (aero-mechanical-acoustic) interaction is relevant in several components of energy-converters but extremely important in the case of the fan and compressor because it has a large influence on the overall efficiency, operability and noise generation of an engine. A non-justified separation and investigation of individual effects on reduced models can produce misleading results due to nonlinear physical interactions, particularly if they involve vastly different spatial and temporal scales. To overcome this problem, it is necessary to develop integrated design and analysis systems. Where physically justified, such a holistic system can be divided into sub-models with appropriate interfaces.

The underlying physical phenomena are extremely difficult to capture in numerical simulations, and particularly the non-linear influence of large amplitude blade vibrations needs to be quantified and understood. If the instability scenario becomes detectable through holistic modelling methods, it will enable three main optimization approaches:

1. Sophisticated blade designs – making them robust to unsteady phenomena
2. Countermeasures against resonant phenomena - changing steady flow conditions to desensitize the system to disturbances

3. Mistuning the system to suppress resonance (aerodynamic/mechanic/acoustic)

An improvement of stability can directly lead to a higher stage loading and subsequently enhanced operability. As a result, the overall pressure-ratio of the compressor or fan can be increased in a wider operating range, enabling the desired improvement of thermal engine efficiency. The benefits of understanding instability mechanisms and improved prediction capabilities extend to the whole field of fluid-structural technologies and are expected to enable long term improvements in various turbomachinery applications, such as aviation, space propulsion and wind- and tidal energy.

To improve the fundamental understanding of underlying physical coupling phenomena and enable the advancement of methods to predict the aerodynamic and aeroelastic behaviour of compressors and fans a comprehensive data base of measurements on application-representative state-of-the-art components is required.

The work of the author throughout the past decade was dedicated to the analysis of instability mechanisms in high-speed turbomachinery through development and application of advanced experimental methods and a purposeful synthesis with numerical simulations. As will be laid out, significant advancements in the fundamental understanding could be achieved through synchronous analysis of aerodynamics, structure-dynamics and acoustics. Particularly the identification of convected radial vortices in a high speed compressor and the lock-in of their propagation speed due to structural interaction has lead to a revised interpretation and modeling approaches of coupled and uncoupled pre-stall phenomena. In this manuscript, the different contributions of the author are structured and reviewed in the context of recent and future research actions.

The document is structured as follows:

- A brief review of the instability mechanisms in turbomachinery is given
- The long established interpretation of pre-stall phenomena is laid out and fundamentals are explained to put the author's research into context
- A summary of the post-doctoral contributions of the author is presented. This includes the interpretation of measurements, computational results and the development and application of a semi-analytical model.
- The revised interpretation and classification of instability mechanisms based on the research outcomes is proposed
- Current and future research activities and programs under supervision of the author are presented and put into context of the global research objective

1.1.1 Relevant Instability Mechanisms

The research described in this manuscript focusses on physical effects limiting the operating range of two components, a) fans of high-bypass turbofan-engines and b) highly loaded axial compressors. As will be shown, safety critical phenomena in the two components are comparable, particularly for novel designs. Generally, this includes effects which are synchronous to the rotor frequency and its harmonics, for example rotor-stator interactions and excitations due to system-asymmetry and inlet distortions, as well as non-synchronous effects. As synchronous excitation mechanisms are well understood today (Tyler and Sofrin, 1962), the most challenging aeroelastic phenomena for future turbomachinery applications are of non-synchronous nature. In literature, the following well-documented non-synchronous phenomena have been identified as very critical for the integrity of the system:

Flutter is defined as an instability of the coupled (aero-structure) system and often involves blade-to-blade coupling. It is often described as 'self-excited', because an initial small amplitude blade oscillation in a specific eigenmode exponentially amplifies through a positive feedback loop with the aerodynamic field (negative aerodynamic damping). Linear modeling approaches are capable to predict this instability and to determine critical modes and to develop countermeasures. The disturbance is only dependent on the blade vibration and disappears as soon as the vibration stops. For large vibration amplitudes limit-cycle-oscillation may occur due to aerodynamic or structure dynamic

non-linearity. For turbo-engine fans critical modes are typically dependent on swirling acoustic modes that establish between the inlet and the fan stage (Vahdati and Cumpsty, 2016).

Buffeting describes the interaction between an aerodynamic instability, such as vortex shedding or shock-wave boundary layer interaction, that comprises a characteristic frequency and blade vibration in a specific eigenmode (Horcas et al., 2020). Typically, no circumferential blade-to-blade coupling is necessary but often planar acoustic duct modes establish and synchronize the phase of the aerodynamic instabilities.

Rotating Stall is a well known and purely aerodynamic phenomenon occurring due to overloading of a blade row and subsequent flow separation leading to the establishment of circumferentially propagating stall-cells. It typically excites structural eigenmodes due to unsteady loading but for small amplitudes the propagation is not coupled with the blade vibration (Zhao et al., 2020).

Prior to the onset of rotating stall, non-synchronous phenomena involving aerodynamic or acoustic fluctuations and structural vibrations have been identified in compressors and fans which cannot be categorised into the three groups above. Partly ambiguous nomenclature and physical interpretations prevail. As will be shown in this document, the contribution of the author has helped to classify the following phenomena:

Non-synchronous forced response: In multistage compressors, non-synchronous coupling mechanisms between a partially trapped acoustic mode, coincident with a structural vibration pattern can lead to significant blade vibration (Fiquet et al., 2021b). This is similar to non-synchronous vibrations forced by rotating stall.

Planar acoustic modes: For different types of machines, acoustic modes establish in the ducts of experimental setups, typically when the compressor or fan is operating at throttled conditions. Precursors of rotating stall in form of planar acoustic modes have been identified to interact with an asymmetric flow pattern in composite material fans, which are different from surge.

Convective Non-Synchronous-Vibration (NSV): Typically occurring close to the stability limit but before the onset of rotating stall, a complex lock-in mechanism between propagating aerodynamic vorticity disturbances and blade vibration is described under the term Non-Synchronous-Vibration. Experiments of the author have shown a correlation between propagating vortical disturbances and the phase of blade vibrations in a torsional eigenmode. Based on these results the coupling mechanisms were explained and a semi-analytical model was developed. The phenomenon needs to be differentiated from flutter as the aerodynamic disturbance appears without blade vibration and has a characteristic convective propagation speed. Even though this phenomenon has been primarily identified in high-speed compressors, experiments on modern low-speed fans have shown a similar behavior. Understanding of coupling mechanisms is vital for the design of future engines. In the following, the relevant physical dependencies and characteristics for this classification are laid out in detail.

1.2 The stability limit

The main phenomena limiting the operating range of compressors and fans can be classified according to the physical contributions into purely *aerodynamic phenomena* and *coupled aeroelastic phenomena*.

Purely aerodynamic phenomena, such as rotating stall have been studied over several decades (Emmons, 1955) and are well understood even though accurate simulations are still challenging. The onset of rotating stall clearly represents the limit of the operating range of a specific stage, leading to a drop of performance and pressure rise. However, multi-stage compressors can be operated for a limited time at conditions with stalled individual stages (typically front stages) as long as vibrations are acceptable and surge can be avoided.

Research from the past decades has shown that in modern turbomachinery designs, precursors of full-scale rotating stall cells can establish and propagate continuously without causing a significant drop of the performance even in single stage compressors or fans. These conditions are of great relevance as the aerodynamic structure typically becomes sensitive to disturbances and feedback mechanisms (structure-dynamic or acoustic), leading to possible resonance that can be safety critical. In this case, the *coupled aeroelastic system becomes unstable* before the aerodynamic stability limit is reached.

Findings from low-speed test facilities are not necessarily transferable as the ratio between aerodynamic forcing potential and structural stiffness is not representative for high speed machines. For this reason, experimental research on high speed machines presents an important contribution to understanding of stability limiting phenomena in state of the art turbomachinery.

In many cases described in literature, the limiting phenomenon depends on the operating speed of the machine. Typically, aerodynamic phenomena limit the operating range at design conditions whereas aeroelastic instabilities occur at part-speed (Vahdati and Cumpsty, 2016). This is schematically shown in Fig. 1.1 but is not to be generalized. The work presented here concerns only the limit of the operating range at highly loaded conditions towards low mass-flow ratio. A comprehensive analysis of the stability at unloaded conditions is given by Rendu et al. (2020).

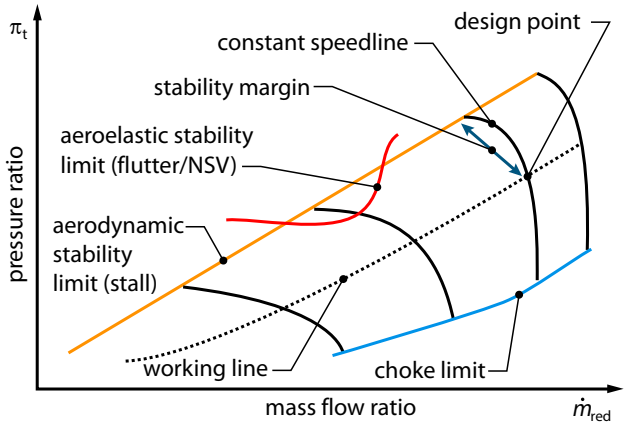

Figure 1.1: Schematic operating range of compressor or fan stage

In turbomachinery fans and compressors, multi-physical phenomena are prominent at loaded conditions in the tip region of the rotor. The fundamental and simplified flow structure is characterized by highly three-dimensional effects: tip leakage vortex, compression shock and boundary layer interactions. The described phenomena, schematically shown in Fig. 1.2a, interact with each other and tend to be very sensitive to disturbances, comprising a wide range of frequencies and wavelengths. They greatly depend on small variations of the local tip clearance and blade geometry resulting from changes in operating conditions. Operating at part speed conditions, additional radial flow migration occurs in the rotor due to the transonic blade design at the tip.

The unstable character of the aerodynamic flow structures can become safety critical if a feedback mechanism as depicted in Fig. 1.2b establishes leading to high amplitude fluctuations. The author's

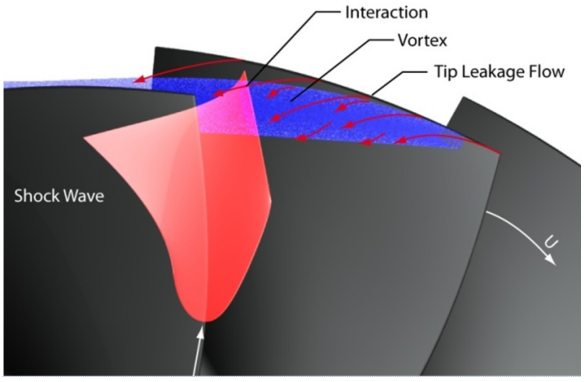

(a) Flow structures at transonic conditions

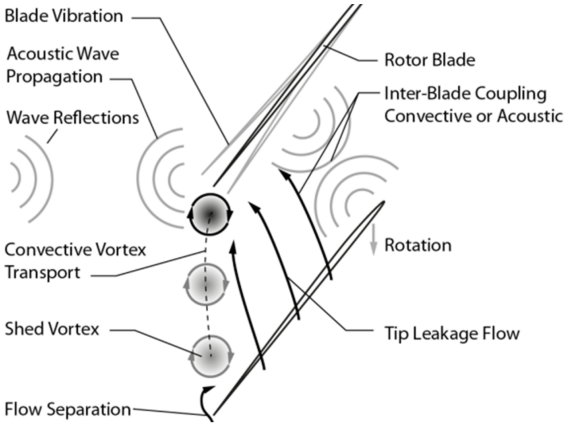

(b) Convective and acoustic coupling mechanisms in a rotor blade row

Figure 1.2: Schematic of flow phenomena in the tip region of transonic compressors

research has helped to clarify the difference between the following types of non-synchronous vibrations:

1. A circumferentially convecting aerodynamic disturbance locks in with a vibration mode or a partially trapped helical acoustic mode. In this process, the disturbance forms a coherent circumferential wave, which is in resonance with the vibration.

2. Aerodynamic flow structures which remain fixed to the rotor blade interact with an external feedback mechanism that may be of acoustic or mechanical nature.

Both mechanisms lead to high-amplitude vibrations in the blades‘ natural frequency that can be devastating within a few seconds but have practically no detectable precursors.

1.2.1 Influence of design trends

For high-speed fans rotating stall, buffeting and flutter are the most common instability mechanisms and well understood today. The establishment of UHBR-configurations with low-speed fans however leads to a substantial change of relevant characteristics.

- Low-speed fans will predominantly operate on the flat part of the compression characteristic, making them more susceptible for stall-driven instability (Lee et al., 2017).

- The flutter frequencies (in the stationary frame) will be lower compared to high-speed designs. As a result, acoustic liners in the intake, which are designed to attenuate higher frequency community noise will not affect the modes relevant for aero-elastic instability.

- The intake length will be shorter for low-speed fans, leading to stronger inflow asymmetry (Benichou et al., 2019) and altered acoustic interaction (Bontemps et al., 2021). This gives rise to stronger broadband excitation and shifted resonance frequencies.

- The relative Mach number and shock strength are lower, the relative tip-clearance and solidity smaller than for conventional direct-drive fans and more sensitive to geometric asymmetry (Rodrigues et al., 2021).

- A strongly nonlinear fluid-structure-interaction at low-frequencies has been observed for fans with low solidity related to the pressure untwist of the blades. At transonic conditions, slight deviations of the local stagger angle at the blade tip can cause a fundamentally different shock structure between adjacent blades that affects the stability of distinct rotor sections (Lu et al., 2019b). This circumstance affects the applicability of promising methods like intentional blade mistuning (Stapelfeldt and Brandstetter, 2021) to suppress the development of circumferentially propagating modes.

In high-speed compressors, the same sensitivity towards Non-Synchronous-Vibrations is observed, but resulting from a different cause: To reduce weight, individual stage loading has been significantly increased over the past decades. To achieve this, the optimization of the aerodynamic design of the compressor blades has led to prominent forward sweep at the blade tip, resulting in structural eigenmodes with significant torsional component and displacement of the leading edge. As will be shown later, this is the dominant factor driving the sensitivity towards NSV. Furthermore, front stages of multi-stage compressors are typically manufactured as blisks, providing negligible structural damping and making them susceptible for aeroelastic interaction.

Chapter 2

Fundamentals on non-synchronous aerodynamic and acoustic disturbances

The work of the author was dedicated to the detection and classification of aerodynamic and acoustic disturbances which may be in resonance with structural vibrations limiting the operating range. In order to classify observed effects into comprehensive categories, the author differentiates between convective disturbances, rotating stall and acoustic modes. Convective disturbances comprise all phenomena traveling with the flow. Rotating stall and acoustic modes instead propagate relative to the mean flow.

In order to put the work into context, fundamentals on the established interpretation on rotating stall, its precursors and trapped acoustic modes in turbomachines are given in the following sections.

2.1 Notation

The interpretation of unsteady phenomena in turbomachinery relies heavily on the analysis of so called spinning modes; defining the temporal and spatial variation of flow variables. In experiments, most commonly the pressure is analysed and the following will briefly review the fundamentals to define the notation used throughout this manuscript.

The unsteady pressure field, or the unsteady aerodynamic disturbance, at a given axial and radial location can be described as a superposition of different aerodynamic modes. Each mode has a circumferential wave number N_a and angular frequency ω_a^S in the stationary frame of reference. Throughout the manuscript Ω is used for angular velocities, ω for frequencies measured at a specific location, superscripts S and R indicate the stationary or relative frame of reference, subscripts a aerodynamic or acoustic, v vibrational disturbances, subscript r indicates the rotor speed ($\Omega_r^S = \Omega_r$). The pressure variation $\tilde{p}$ in a given mode in the stationary frame of reference is hence written as:

$$p(\theta, t) = \hat{p} e^{i(N_a \theta - \omega_a^S t)} \tag{2.1}$$

Its phase velocity or propagation speed is given by:

$$\Omega_a^S = \frac{\omega_a^S}{N_a} \tag{2.2}$$

When viewed in the rotor frame of reference, the wave number is unaltered but the propagation velocity is shifted:

$$\Omega_a^R = \Omega_a^S - \Omega_r = \frac{\omega_a^S}{N_a} - \Omega_r \tag{2.3}$$

It follows that the angular frequency in the rotor and stationary frame are related by:

$$\omega_a^S = \omega_a^R + N_a \Omega_r \tag{2.4}$$

The same relations hold for vibrational disturbances. A useful distinction between purely aerodynamic and purely vibrational signatures arises from the fact that for vibrational disturbances, the frequency in the rotating frame of reference ω_v^R is physically fixed and the phase velocity is a consequence of this and the nodal diameter (circumferential mode) N_v. As a result, frequencies created by vibration in the same blade mode but different nodal diameters are always spaced integer rotor speeds apart when viewed in the stationary frame of reference:

$$\omega_{v,1}^S = \omega_v^R + N_{v,1} \Omega_r \tag{2.5}$$

$$\omega_{v,2}^S = \omega_v^R + N_{v,2} \Omega_r \tag{2.6}$$

The ratio between the frequency of any phenomenon ω and the shaft speed Ω_r is often denoted as Engine Order (EO) and takes integer values for synchronous phenomena, typical for rotor-stator interactions.

Aerodynamic disturbances, on the other hand, tend to have a physically defined propagation speed but often comprise multiple circumferential modes. The frequencies are a consequence of the propagation speed and the circumferential mode, and they are separated by integer multiples of the propagation speed of the disturbance:

$$\omega_{a,1}^S = \Omega_a^S N_{a,1} = (\Omega_a^R - \Omega_r) N_{a,1} \tag{2.7}$$

$$\omega_{a,2}^S = \Omega_a^S N_{a,2} = (\Omega_a^R - \Omega_r) N_{a,2} \tag{2.8}$$

2.2 Precursors of Rotating Stall

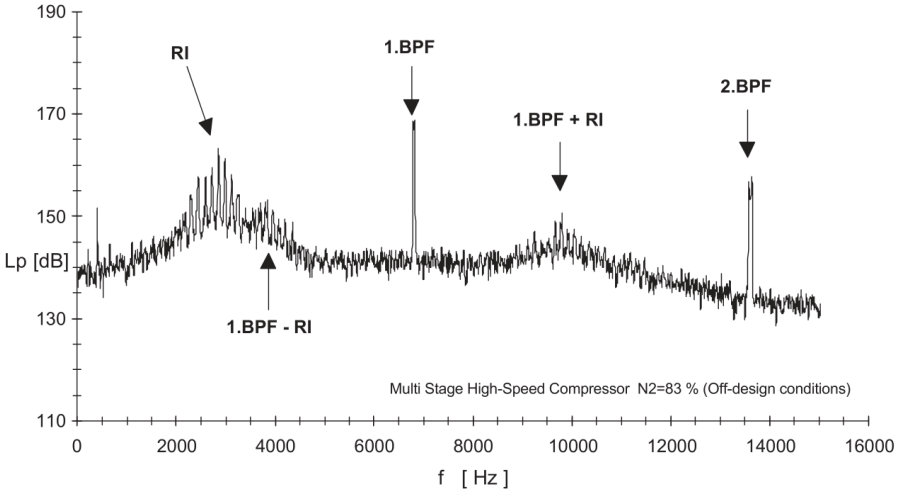

Figure 2.1: Wall pressure spectrum with stall precursor signature (RI) from Baumgartner et al. (1995)

The onset of rotating stall in turbomachinery compressors and fans has been extensively studied and has various forms of precursors. In literature, the topic has received considerable attention. Stall precursors have been identified and classified as modal or spike disturbances according to their characteristic length scale (Camp and Day, 1998). In the former case, disturbances of small amplitude continuously evolve into modal oscillations with a length scale of the compressor circumference. In the latter case, a disturbance with a length scale of only a few rotor blade pitches appears as a transient phenomenon, called spike. This spike travels around the circumference in the direction opposing rotation and develops rapidly into a rotating stall cell. For tip critical compressors showing this spike-type stall inception, much research has been undertaken over the last few decades with the aim to characterize the aerodynamic structure of the disturbance. Inoue et al. (2000), Yamada et al. (2013) and Pullan et al. (2015) describe the aerodynamic disturbance as a small vortex with radial rotation axis (radial vortex—RV), which is shed from the blade leading edge (LE) and travels toward the subsequent blade. This process is often associated with tip leakage flow. According to Yamada et al. (2013), tip leakage fluid "wraps" around a separating vortex and is later spilled around the subsequent blade. This spill forward of tip leakage flow around the blade's leading edge (and trailing edge) has been identified by Vo et al. (2008) as a criterion for spike-type stall inception. When tip leakage fluid accumulates, it blocks the passage. The blockage region becomes especially large when the tip leakage vortex breaks down (Schlechtriem and Loetzerich (1997); Furukawa et al. (1999)), leading to inhomogeneous and unsteady blade loading. This blockage also affects the path along which a radial vortex separating from the leading edge is convected toward the adjacent blade. However, the presence of tip leakage flow is not necessary for the occurrence of radial vortices, as Pullan et al. (2015) showed with studies of a shrouded compressor.

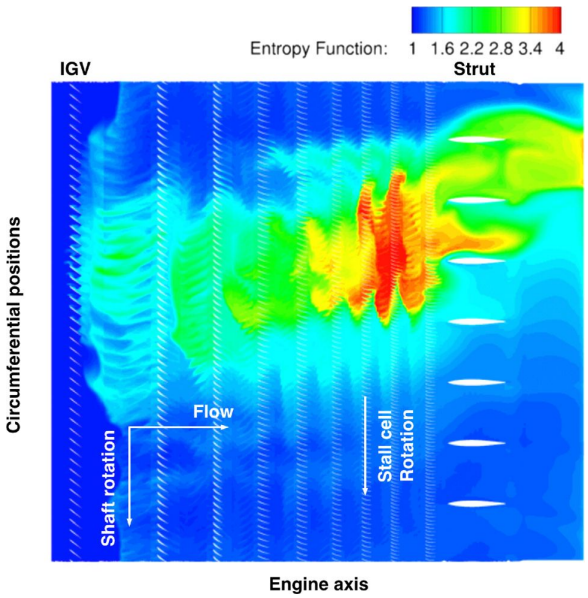

(a) Instantaneous entropy contour on the casing surfacetour

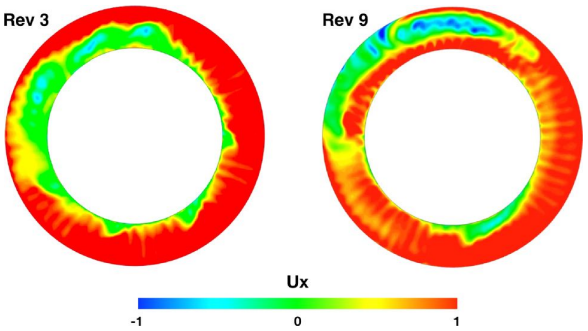

(b) Transient solution at Stator exit, axial velocity con-

Figure 2.2: Numerical simulation of single cell rotating stall in a multi stage compressor, from Zhao et al. (2018)

A special case of stall precursor are small scale aerodynamic disturbances which continuously rotate around the circumference at a fraction of the rotor speed and cause significant pressure fluctuations near the leading edge of the rotor. These disturbances have been identified in several types of compressors and fans and, as will be shown, share a resemblance with the so called spikes but do not necessarily develop into a full stall cell or lead to a drop of performance. When measured in the stationary frame of reference, these phenomena manifest themselves as a range of frequency peaks in the pressure spectrum. The peaks are located at a fraction of the blade passing frequency and often referred to as a "broadband hump". A typical spectrum, showing this type of disturbance has been published by Baumgartner et al. (1995) and is shown in Fig. 2.1. In this and other publications from the era, the term "Rotating Instabilities" has been established. The spectrum shows not only a broadband disturbance (hump) around 30% of the blade passing frequency (BPF) but also individual peaks with a narrow spacing. In addition, this signature is modulated with the blade passing frequency and its harmonics, showing left and right-handed sidebands. This type of disturbance will later be discussed in detail.

2.3 Rotating Stall

Rotating stall is the name given to the phenomenon where one or several zones of reduced flow, also termed stall cells, propagate relative to the blade row. The mechanism by which they propagate has been described by Emmons (1955). It is triggered by boundary layer separation on an individual blade. The stalled blade does not produce sufficient pressure rise to maintain the flow around it, such that the passage becomes blocked by a region of reduced flow. This blockage diverts the upstream flow, leading to an increase in incidence on the trailing blade and a decrease in incidence on the leading blade. The stall therefore propagates in the blade row, moving from the pressure side to the suction side. A stall cell can span multiple passages and extend axially across multiple blade rows as depicted in Fig. 2.2.

When the N_a cells propagate around the circumference, the blades experience periodic aerodynamic forces as the low and high velocity zones pass the blades. The magnitude can be comparable to that of steady-state flow (Graham and Guentert, 1965), and can therefore excite significant blade vibration if the frequency in the rotating frame, $\omega_v^R = N_a \Omega_a^R$, is in resonance with one ore more blade vibration frequencies. Vibration typically occurs in one of the first few eigenmodes, and is usually associated

with a relatively large number of stall cells, because only multiple cells generate sufficiently high excitation frequencies.

Since the vibration occurs near the stall boundary, it is difficult to differentiate it from stall flutter without extensive instrumentation. However, it is a fundamentally different phenomenon. Carter and Kilpatrick (1957) write: "Only in as much as the blading itself is responsible for the exciting forces can the vibration be classed as self-induced. Otherwise the vibration is a forced oscillation". There are a few important measurement indications which can be used to differentiate between flutter and rotating stall excitation:

- Pressure spectra show multiple bands separated by non-integer engine orders, each associated with a circumferential wave number
- The vibration amplitude can be reduced by shifting the blade's natural frequency to be off-resonant with the stall cell
- The resonance condition will vary with inlet temperature because stall frequency is proportional to the mechanical speed of the engine whereas the operating condition at which rotating stall occurs varies with equivalent, or aerodynamic, speed.

In literature, rotating stall has been classified as *progressive* or *abrupt* according to the performance characteristic of the compressor, *stable* or *unstable* according to the temporal periodicity, and *partial span* or *total span* according to its radial extent (Graham and Guentert, 1965). An interesting point with view to vibration in modern compressors, is the distinction between *stable* and *unstable* stall made in early papers. As the name suggests, the former is characterised by time-varying peak amplitudes whereas the latter is steady. Armstrong and Stevenson (1960) report a number of observations for unstable stall:

- The amplitude reduces with increasing stiffness (change in material)
- The amplitude reduces with increasing altitude
- More positive IGV settings (reduced rotor incidence) shift the stall to a lower speed
- With more positive IGV settings, a bigger range in the number of stall cells is possible at a given speed

These observations are in concurrence with what is nowadays commonly referred to as *non-synchronous vibration* and what the author and his coauthors believe to be caused by a convective resonance condition (Stapelfeldt and Brandstetter, 2020). For this type of vibration an initially random aerodynamic disturbance locks-in with blade vibration patterns. In particular, the findings relating to IGV settings agree with measurements made in a transonic research compressor (Franke and Juengst, 2020). This highlights the importance of multi-physical and synchronised instrumentation concepts as developed and applied in the author's research. It is possible that the phenomena described in the following always occurred but only advanced instrumentation has been able to fully explain and characterise them.

To classify Rotating Stall the following conditions are relevant:

1. Flow separation on blade suction side and/or casing boundary layer (2D reversed flow / 3D convergence of streaklines)
2. Periodic unloading / loading of individual blades
3. Propagation of stall cells around circumference approximately 50% rotor speed ($0 < \Omega_a^S < \Omega_r^S$)
4. Propagation speed widely unaffected by external disturbances - free propagation
5. Single stage compressors often show single cell stall ($N_a = 1$), multi-cell is common in multi-stage compressors

6. RS typically initiated by precursor (spike), developing from part-span stall to full span, Multi-cell RS develops towards fewer cells

7. Pressure spectra show consequent peaks at $\omega_n^S = nN_a\Omega_a^S$, peak spacing proportional to propagation speed Ω_a^S, harmonic index n, number of stall cells N_a

In summary, there are several clear indications to characterize rotating stall and the way it leads to non-synchronous forcing on the blades is clearly defined. Aerodynamic stabilization of a given machine, for example through casing treatments or specific geometries with forward swept tips can delay the onset of stall (Passrucker et al., 2003; Brandstetter et al., 2016a). This does not at all apply to the occurrence of different aero-mechanically coupled phenomena involving acoustic or convective interactions, discussed in the following.

2.4 Planar acoustic modes

The most intuitive form of non-synchronous acoustic modes is the planar form, that can be described using one-dimensional theory. Particularly in experimental setups with long tubing systems at the inlet or the outlet, standing acoustic waves establish. Wavelength and frequency of resonant modes can be roughly assessed with the length of the tubing. Even though these are very basic relations from linear acoustic theory, a short summary is given: Open termination (for example a bellmouth with comparably small radius or an abrupt ending of a nozzle or a tube) enforces a pressure node, closed termination (actually closed or very narrow section in a throttle) a pressure peak. Hence the resonant wavelength for the n-th harmonic in a duct with length L_{eq} (equivalent length with end correction), can be deduced for similar terminations (open or closed on both sides) as $\lambda_n = 2L_{eq}/n$, its frequency as $f_n = a/\lambda = na/(2L_{eq})$ with a being the speed of sound.

For a case with open termination on one side and closed on the other (for example throttle to outlet), impair multiples of a quarter wavelength can establish: $\lambda_n = 4L/(2n-1)$ and $f_n = (2n-1)a/(4L)$. Section changes of the flow channel, for example due to a Venturi-nozzle also reflect acoustic waves, with a reflection coefficient proportional to the section change (Miles, 1944). The same problem applies to numerical simulations, where inlet and outlet boundaries impose a specific acoustic termination if non-reflective conditions are inefficient (Grondin, 2019).

If large volumes are present in the setup, their characteristic Helmholtz-frequency can be estimated via $f_H = \frac{a}{2\pi}\sqrt{\frac{A}{V_0 L_{eq}}}$, with opening area A, Volume V_0 and equivalent neck-length L_{eq}. These characteristic frequencies are typically present in experimental setups and strongly differ from real engines. Frequencies are typically low (10-100Hz) compared to characteristic frequencies occurring in turbomachinery (blade-passing, blade-vibration, etc. $>$ 100Hz) but excessive amplitudes and modulations of the flow field are possible if the compressor or fan is working close to stability limit, particularly at an operating point with a positive slope of the static pressure characteristic (Moore and Greitzer (1986), etc.). Synchronous excitation of planar modes can be avoided through deliberate choice of a blade count, avoiding integer multiples between different rows, which is industry standard today.

Non-synchronous modes are still subject of research. In several applications, non-synchronous planar modes can be safety critical for a machine if they serve as a feedback mechanism that synchronizes vortex shedding or unstable shock-boundary-layer interactions (di Mare et al., 2009), discussed under the term buffeting. Coincidence with structural eigenmodes can then obviously cause resonance. A specific interaction of a non-synchronous planar duct mode with the operation of a low-speed fan has been reported by Brandstetter et al. (2019c) for a novel test facility with long exit tubing, including a venturi-nozzle, shown in Fig. 2.3. It has been shown, that a strong modulation of the inlet pressure (Fig. 2.3 b) and the asymmetry of the flow field in the rotor occurred at near-stall conditions. This will be discussed in detail in section 5.1.3.

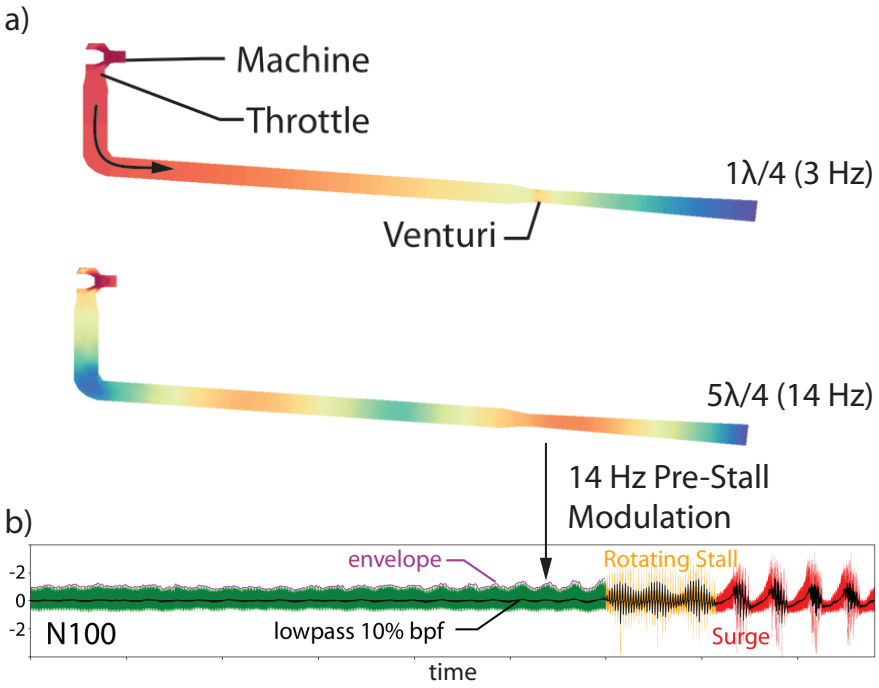

Figure 2.3: planar modes in exit-duct, a) acoustic pressure in exit duct, b) wall pressure signal during stall inception

Presence of planar modes can be easily identified and characterized using circumferentially distributed wall pressure sensors:

1. Like structural eigenmodes, the frequency of planar duct or cavity modes only slightly changes with the operating condition (frequency proportional to speed of sound), making them appear as almost horizontal lines in a Campbell diagram during rotation speed variation
2. As the waves are plane, circumferentially distributed sensors will show an inter-phase angle of 0°
3. Independence from the actual turbomachine can be verified by deriving impulse-response spectra Brandstetter et al. (2019c)

2.5 Spinning acoustic modes

While broadband acoustic disturbances are a general problem for noise emissions, tonal acoustic modes in turbomachinery can be extremely dangerous under certain conditions. Synchronous tonal noise resulting from interactions of rotors and stators are extensively discussed in literature and well understood (Tyler and Sofrin, 1962). For the interaction-phenomena in the focus of this work, non-synchronous, circumferentially spinning acoustic modes are of relevance (Parker and Stoneman, 1989).

As acoustic duct modes are a recurring issue in the result-section of this manuscript, a brief description of the relevant conditions and characteristics is given in the following. A more detailed analysis can be found in literature ((Cumpsty and Whitehead, 1971; Camp, 1999; Cooper and Peake, 2000; Hellmich and Seume, 2008)).

In a narrow duct with rigid walls, acoustic modes can be considered as two-dimensional pressure fluctuations with x being the axial and θ the circumferential coordinate. The solution of the homogeneous wave equation for one mode can be expressed in the form:

$$p(x,\theta,t) = \hat{p}e^{-i\omega_a t + N_a\theta}e^{-iCx} \tag{2.9}$$

If coefficient C is complex, the wave propagates axially in the duct without attenuation, a real value of C leads to an evanescent wave. Eigenvalue analysis shows, that a critical value for C exists as a function of the duct geometry, the mean flow conditions, the frequency ω and the circumferential wave number N_a.

Strictly speaking, eigenvalue analysis is always necessary to determine cut-on conditions, but a coarse approximation can be made for low axial Mach-Numbers as follows. A spinning acoustic wave of zeroth mode order (Bessel functions as discussed by Tyler and Sofrin (1962)) is propagative (cut-on) with constant amplitude, if the phase velocity of the wave relative to the flow exceeds the local speed of sound. The corresponding cut-on frequency rises linearly with the circumferential wave number N_a. Inside a compressor rotor, the tangential velocity v_θ of the flow increases ($v_{\theta 2} > v_{\theta 1}$) as well as the local speed of sound a, hence the necessary phase velocity of a co-rotating mode needs to increase in order to propagate downstream.

The tangential flow velocity v_θ changes the phase velocity c_a^S necessary for propagation in the stationary frame of reference as depicted in Fig. 2.4. Assuming a narrow duct with average radius R the phase velocity for a specific mode with the frequency ω_a^S in the stationary frame of reference is given with its circumferential wave Number N_a as:

$$c_a^S = \frac{\omega_a^S R}{N_a} \tag{2.10}$$

For co-rotating modes ($N_a > 0$, forward traveling waves: FTW) and low axial Mach number the cut-on condition is met, if the circumferential phase velocity exceeds the sum of the local speed of sound a and the tangential flow velocity v_θ:

$$c_{cut-on,FTW} > a + |v_\theta| \tag{2.11}$$

In contrast, for backward traveling waves (BTW) the phase velocity is lower according to:

$$c_{cut-on,BTW} > a - |v_\theta| \tag{2.12}$$

A given co-rotating acoustic mode with a specific frequency ω_a^S and circumferential wave number N_a can hence be cut-off downstream of the rotor and only be propagating upstream if the phase velocity $c_2^S < a_2 + |v_{\theta 2}|$ as depicted in Fig. 2.4 as AR-Range FTW. Inversly, specific counter-rotating modes can be cut-on only in the downstream direction.

Here, the range for modes to appear in the AR-Range BTW is slightly narrower than for Co-Rotating modes since the increase of the speed of sound counteracts the increase of tangential velocity. All observations of acoustic resonance for swirling modes described in literature known to the author fit in the respective range, that is at the limit of being cut-off in one axial direction.

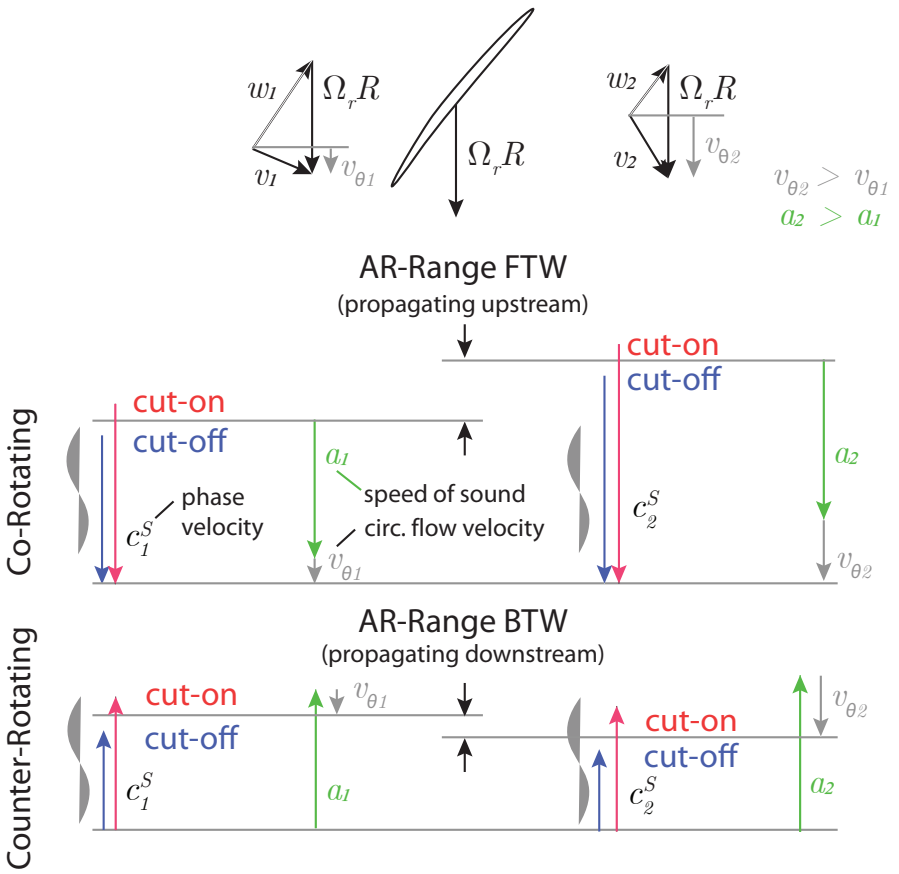

Figure 2.4: Propagation Conditions for Acoustic Resonance at low axial Mach-Numbers

Again, this consideration is only valid for very low axial Mach-Number, but very helpful for a first assessment if a specific phenomenon could be attributed to a spinning acoustic mode and supports the interpretation of results. A comparison for a specific case from Fiquet et al. (2021b) is shown in Fig. 2.5, illustrating the range of acoustic resonance for co- and counter rotating modes for a case with axial inflow $v_{\theta 1} = 0$. It can be seen that with rising axial Mach-Number, the cut-off frequency decreases slightly, illustrating the error range of the consideration lined out above.

The highest amplitude of the acoustic modes is observed near the stage in which the mode propagation condition changes from cut-on to cut-off, indicating that the energy source for the mode is located in the respective stage. The source can be related to periodic vortex shedding from the rotor (or stator) blades (Cumpsty and Whitehead, 1971), or a fluctuation of zones with separated boundary layers Fiquet et al. (2021a), which is phase locking to the acoustic mode. In the rotating frame of reference the frequency of a specific mode is given as:

$$\omega_a^R = \omega_a^S - N_a \Omega_r \tag{2.13}$$

The local aerodynamic effect in the blade row that is necessary as energy source for the acoustic mode must fit this frequency. Hence, the range for possible waveforms occurring during acoustic resonance can be narrowed down based on the described conditions as follows. Assuming classical vortex shedding the frequency $\omega_{a,St}^R$ can be estimated based on flow velocity and blade geometry (Strouhal-frequency). The expected circumferential wave number N_a can be derived as

$$N_a = \frac{\omega_{a,St}^R}{c_{cut-on}/R - \Omega_r} \tag{2.14}$$

with the limits for c_{cut-on} given by equations 2.11 and 2.12 for co-and counter swirling modes respectively.

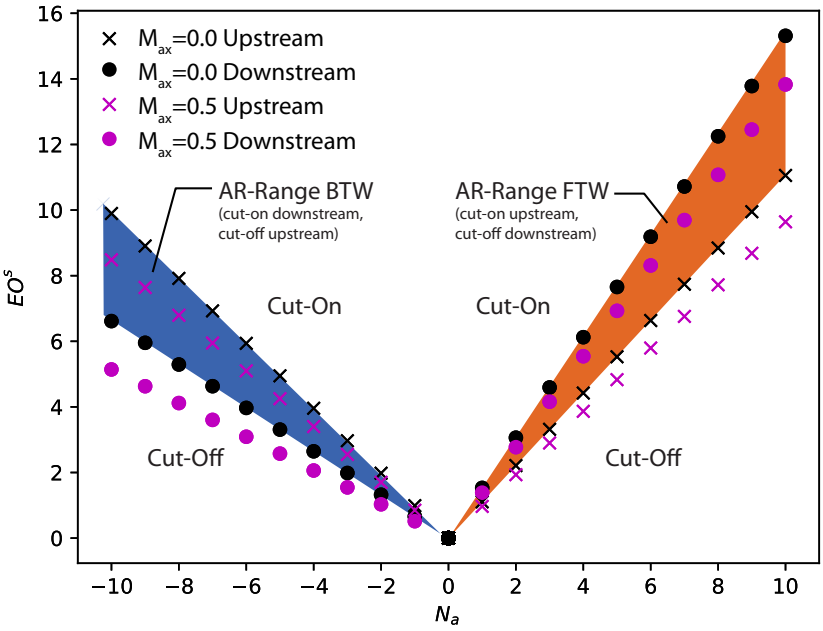

Figure 2.5: Exemplary Range for Acoustic Resonance, Dependency on rotation direction for $v_{\theta 1} = 0, v_{\theta 2} = 170ms^{-1}, T1 = 340K, T2 = 380K$ Black Symbols for $M_{ax} = 0$, magenta for $M_{ax} = 0.5$

This equation is also valid for cases which do not rely on classical vortex shedding like fluctuating flow stall patterns, oscillations of the tip-leakage flow (Mailach et al., 2001; Brandstetter et al., 2019b) or shock-boundary-layer interactions, (di Mare et al., 2009).

In many experimental observations of acoustic resonance a strong modulation (scattering) of the fundamental acoustic mode with the blade passing frequency (and its m harmonics) is present (Hellmich and Seume, 2008). This manifests as sidebands in the frequency spectrum of the acoustic pressure. Furthermore, n harmonics of the fundamental mode are typically present (Brandstetter et al., 2019b). With the frequency of the fundamental mode in the stationary reference frame ω_a^S and the Blade number N_b the frequency spectrum shows modulation peaks as:

$$\omega_{a,mod}^S = n \cdot N_b \Omega_r \pm m \cdot \omega_a^S \tag{2.15}$$

Experimental observations show that the dominant acoustic mode can be a harmonic (or subharmonic) to the local aerodynamic or structure dynamic effect which is in resonance. Summarizing the characteristics of acoustic resonance, the following points can be deduced:

- Acoustic resonance is typically excited by an unstable aerodynamic feature in a rotor or stator that is receptive to an external feedback mechanism
- An established acoustic mode can trigger phase-locking of periodic vortex shedding and fix circumferential wave numbers
- Acoustic resonance does not require a convective transport mechanism (radial vortices, etc.) to establish
- The flow conditions in the machine, particularly the change of tangential velocity in a rotor leads to a separation of modes, which are propagative (cut-on) only in one axial direction
- The range of propagation speeds for resonant acoustic modes is limited and characteristic for a specific operating point, fixing the possible wave numbers for given frequencies
- Co-rotating modes are propagative upstream, counter-rotating modes downstream of a rotor (due to rising swirl)

- Dominant acoustic modes are typically observed with strong harmonics and modulations with the blade passing frequency which can themselves lead to the excitation of structural modes
- Modes with low circumferential wave number are less prone to diffraction and reflection in the blade rows
- The peak spacing in a pressure spectrum is not representative of the propagation speed, as different modes propagate with different circumferential phase velocities. Circumferentially distributed sensors are necessary to detect wave number and phase velocity

2.6 Convected vorticity disturbances / "Rotating Instabilities"

As already indicated, a specific form of stall precursor identified as vorticity disturbances is discussed under the term rotating instability. It concerns the most controversially disputed non-synchronous phenomenon occurring at highly loaded operating conditions in compressors and is closely linked to the formerly described rotating stall.

It originated around 1995 and was particularly established by the studies of Baumgartner et al. (1995); Kameier and Neise (1997); Maerz et al. (2002) and later readdressed by Mailach et al. (2001). Until today the term is commonly used in different studies and specifically associated to characteristic measurement signatures:

a) a broadband "hump" in the frequency spectrum of a pressure sensor at a fraction of the blade passing frequency, often appearing with individual frequency peaks within the hump

b) a linear phase evolution in a cross-spectrum of circumferentially distributed sensors.

Several attempts have been made to assign a physical phenomenon to the signature but are still under discussion (Cumpsty, 2001).

Baumgartner et al. (1995) interpreted the disturbance as a "flow instability in the tip region", associated to a vortex shedding mechanism that "can be interpreted as a rotating source to generate pressure waves [...], moving relative to the blade at a fraction of the rotor speed [...], similar to rotating stall". However, a difference to rotating stall was emphasized, noting that stall does not excite pressure fluctuations in its own frame of reference. Furthermore a link to the influence of enlarged tip clearance, boundary layer separation and blade vibrations was drawn. The image of a "rotating loudspeaker that is moving relative to the rotor blade" was established and later experimentally confirmed by the study of Kameier and Neise (1997), who reproduced RI spectra using exactly this source.

While several further studies on the physical origin of the disturbance have been presented, the interpretation of Mailach et al. (2001) needs to be mentioned, assigning eventual peaks in the broadband hump to consecutive and superimposed modes associated to fluctuations of the tip leakage vortex and all propagating with a fraction of the rotor speed.

Published discussions on these studies aim to point out that the phenomenon might just be a specific form of a part-span rotating stall cell, similar to the phenomena described by Inoue et al. (2000) illustrated in Fig. 2.6.

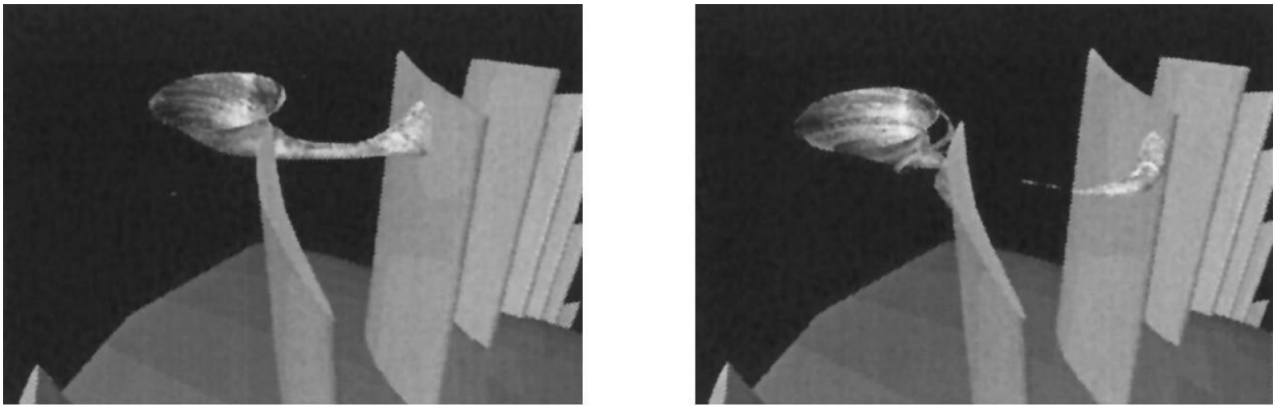

Figure 2.6: Illustrations for the flow mechanism of short-length-scale stall cell, from Inoue et al. (2000)

In contrast, experimental studies on high-speed machines have shown, that the frequency signature, or more specific individual peaks within the "broadband hump" can be associated to Non-Synchronous-Vibrations.

Following the literature discussed above, the one feature differentiating the interpretation of a "rotating instability" from other near-stall unsteady phenomena is the presence of a frequency in the frame of the rotating disturbance. This idea of a 'source frequency in the source's frame of reference' was first established by Kameier and Neise (1997) has since been employed for a range of RI studies.

As will be discussed in the results section, Brandstetter et al. (2020) have demonstrated that the phenomenon can be clearly explained without the necessity of a source frequency but rather a circumferential convection of vortical disturbances which can be randomly distributed around the circumference. The main signature differentiating these from swirling acoustic modes, is that the circumferential convection speed is independent from the pattern of the disturbance. This characteristic of convected disturbances will be recurring throughout the results section. In contrast to so-called spikes, the convected vorticity disturbances do not evolve rapidly into rotating stall-cells. Measurements have shown that the aerodynamic structure is comparable, yet, the blade to blade convection occurs within the blade-passage whereas spikes can travel upstream of the leading edge, (Young et al., 2012), as depicted in Fig. 2.6 and Fig. 2.7.

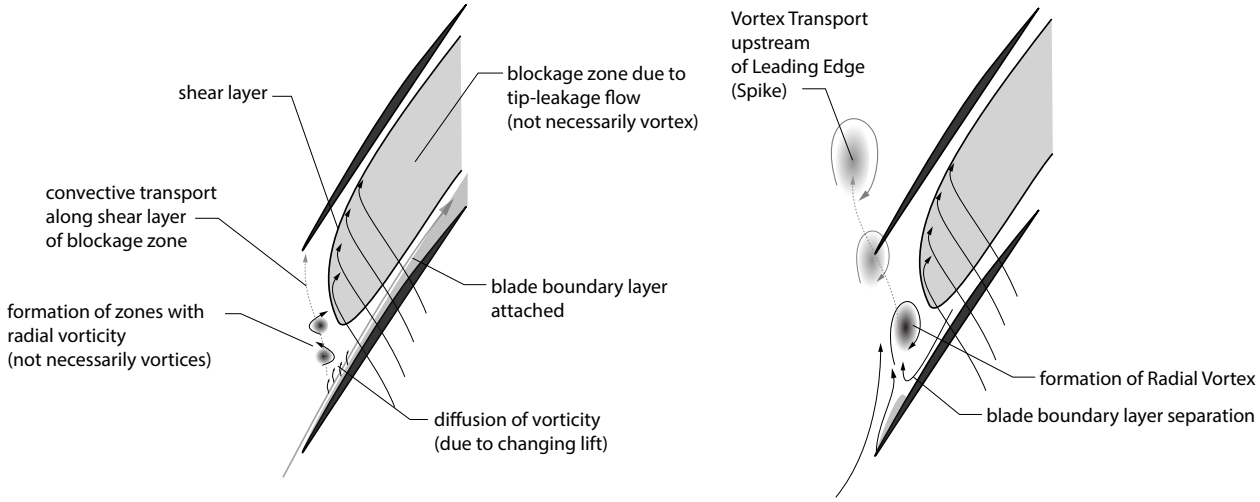

Figure 2.7: Comparison between convected vorticity disturbances occurring during NSV or "Rotating Instability" and a spike type stall precursors

Chapter 3

Contributions from Post-doctoral research

The published post-doctoral work of the author and PhD students under his supervision can be structured into three branches:

a) Convected Aerodynamic Disturbances: From experiments on an HPC stage at Technische Universität Darmstadt (Fig. 3.1a) a specific phenomenon of convected disturbances was characterized and a relation (lock-in) to blade vibrations was proven. The findings could be confirmed on a low-speed fan at Ecole-Centrale de Lyon (Fig. 3.1b). Based on these results a model was developed that allows the prediction of the lock-in phenomenon. Later, this model was linearized and used for stability analysis and the assessment of aerodynamic and structural mistuning.

b) Acoustic Resonance: On the test facility at ECL the establishment of planar acoustic duct modes was discovered and related to a resonating rotor-fixed asymmetry. This stands in contrast to swirling acoustic modes, which have been observed in two different multi-stage setups. For one multistage compressor, the phenomenon could be reproduced and explained.

c) Open-Test-Case Low Speed Fan: A fan stage from composite materials was developed at ECL and introduced in 2021 for numerical and experimental investigation (Fig. 3.1b). The studies concerning this development are closely related to the research on convective disturbances in lock-in with structural vibrations and acoustic resonance.

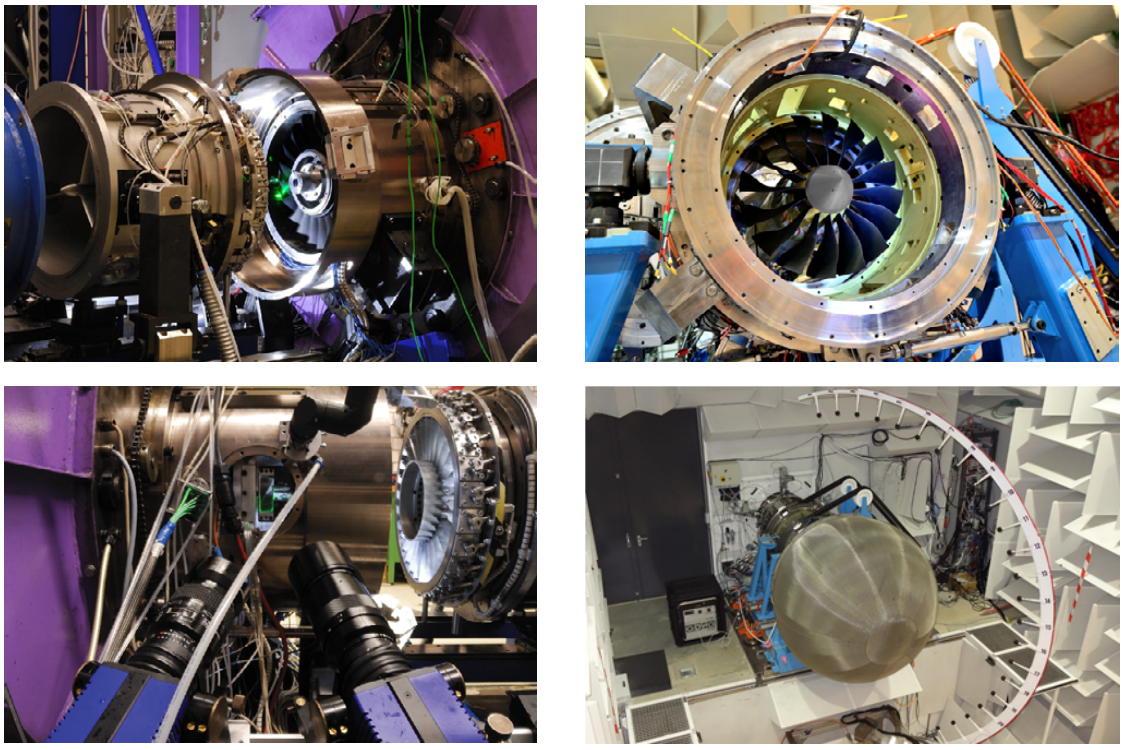

a) High-Pressure-Compressor
TU-Darmstadt
(2007-2017)

b) UHBR Fan
Ecole Centrale de Lyon
(2017-present)

Figure 3.1: Main test facilities

A structured visualization of the concerned publications is presented in Fig. 3.2, indicating experimental studies, numerical simulations and reduced order modeling. Following this thematic structure, the results are summarized in the following chapters.

The publications comprise a selection of peer-reviewed works in Journal of Turbomachinery (JT), Journal of Sound and Vibration (JSV), Journal of the Global Power and Propulsion Society (GP), ASME Turbo Expo (TE) and the European Turbomachinery Conference (ETC), with the author of the manuscript either as first or corresponding author to publications by the PhD students Anne-Lise Fiquet, Martin Rodrigues or Valdo Pages.

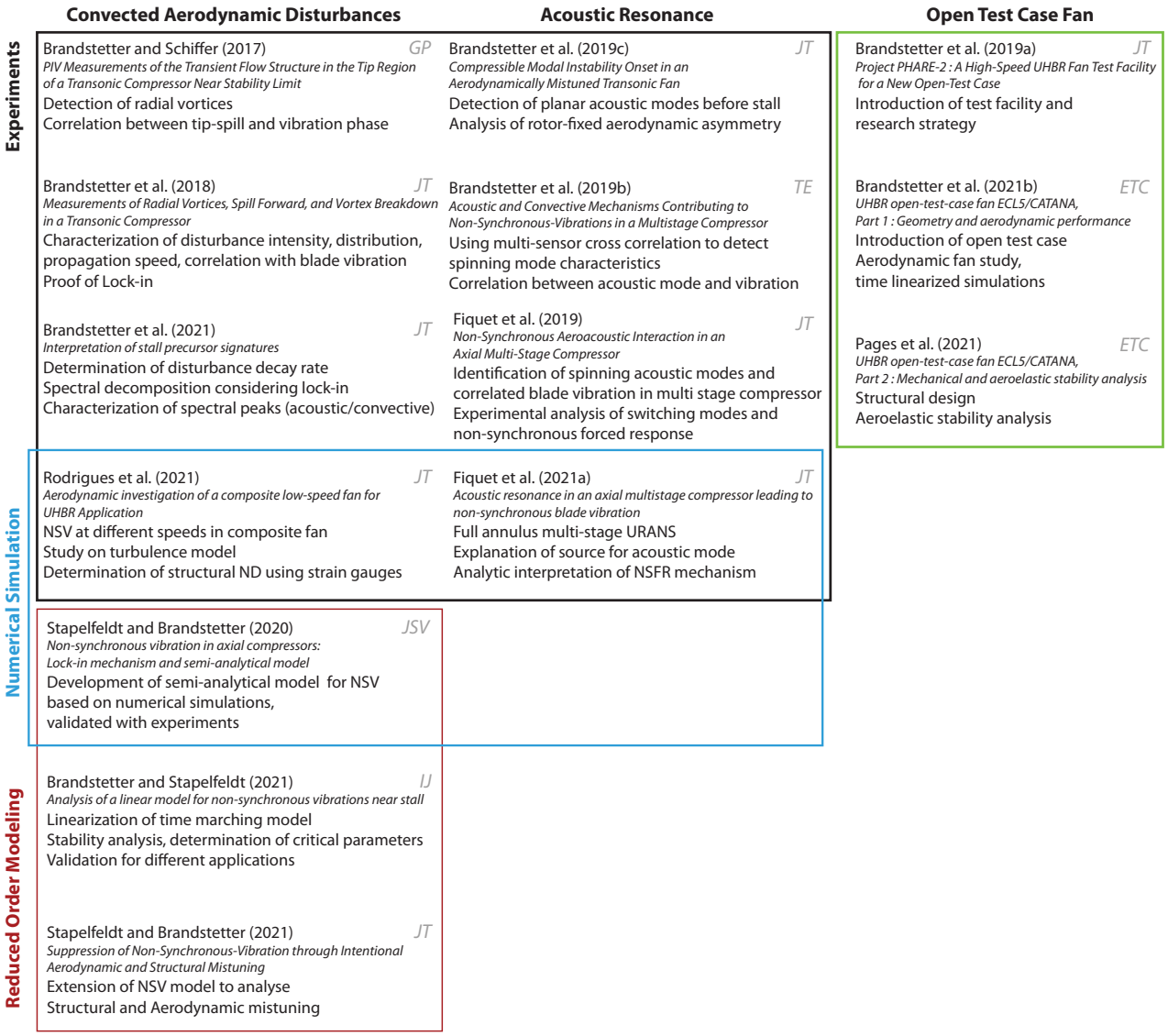

Figure 3.2: Structure of selected post-doctoral publications

Chapter 4

Vibrations driven by convected aerodynamic disturbances

4.1 High-speed compressor: Unsteady aerodynamics in tip region

At Technische Universität Darmstadt an experimental one-and-a-half stage high speed compressor was established in 2008 and investigated with a focus on aerodynamic performance and aeroelastic instabilities. The machine, designed by Rolls-Royce-Germany is representative of a front stage of a modern high-pressure transonic compressor of an aircraft engine and provided the basis for the authors thesis and post-doctoral research. A description of the setup is given in (Biela et al., 2011). The rotor is fabricated as an integral bladed disk (blisk) from titanium with very low structural damping. The experimental characteristic is presented in Fig. 4.1

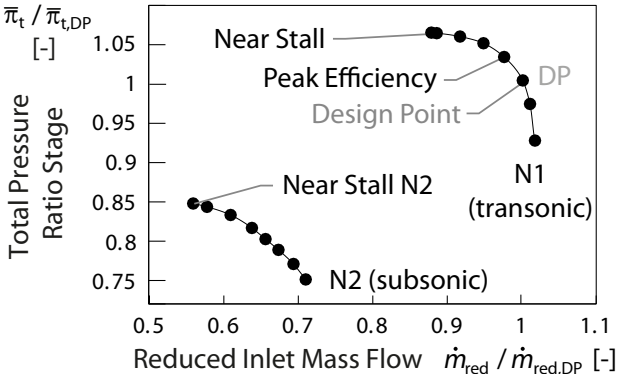

Figure 4.1: Total pressure characteristic of transonic compressor, from (Brandstetter et al., 2018)

The author developed a laser-optical setup to measure the flow field in the tip region that allowed to determine the evolution of the tip-leakage flow and the associated blockage in the tip region (Brandstetter et al., 2011). This work involved design of customized laser-optical components and evaluation methods as commercial systems were not capable to provide the required resolution. A stereoscopic Particle-Image Velocimetry setup was employed as depicted in Fig. 4.2. A laser-lightsheet was generated at 92% of the channel height to illuminate the main flow which was enriched with petroleum-fume

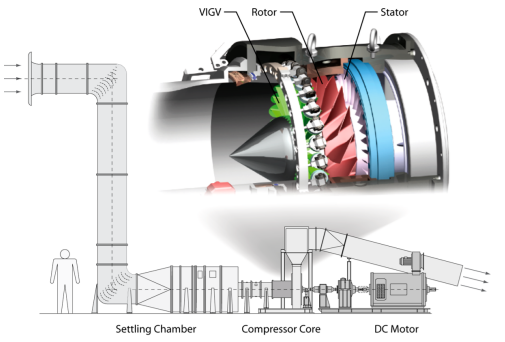

(a) Transonic compressor test facility at Technische Universität Darmstadt

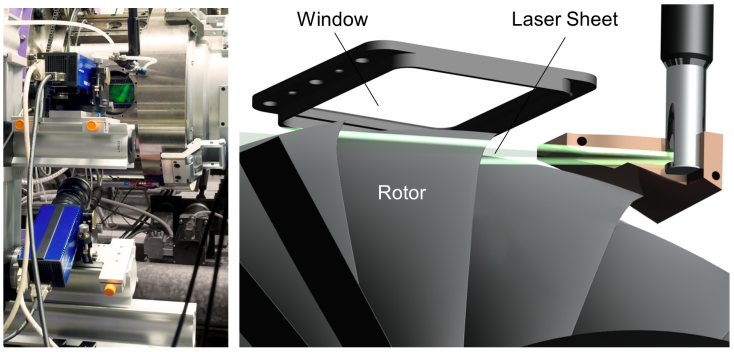

(b) Stereoscopic PIV setup

Figure 4.2: High-Speed compressor setup with Particle-Image-Velocimetry system, from (Brandstetter et al., 2011)

seeding. CCD cameras record double-images with a specific time delay, given by the laser double pulse. Displacement of the particles recorded on both exposures of the double-images is calculated using a cross-correlation algorithm to measure the local velocity of the flow. The combination of two cameras, observing the lightsheet from different angles allows the reconstruction of all three velocity components in the light sheet plane. The average of a phase locked series of vector fields describes the mean flow structure while individual snapshots of the flow field allow the assessment of transient flow structures.

Fig. 4.3 shows ensemble averaged results for the relative Mach-number while throttling the machine from choke condition (left) towards the stability limit (right) from Brandstetter et al. (2011). It can be seen how a blockage zone - characterized by low relative velocities - developing due to the tip leakage flow in the middle of the blade passage, increases in size and encompasses the whole passage at near-stall condition. This blockage zone is of great importance, as disturbances developing in the leading edge plane cannot propagate downstream through the passage.

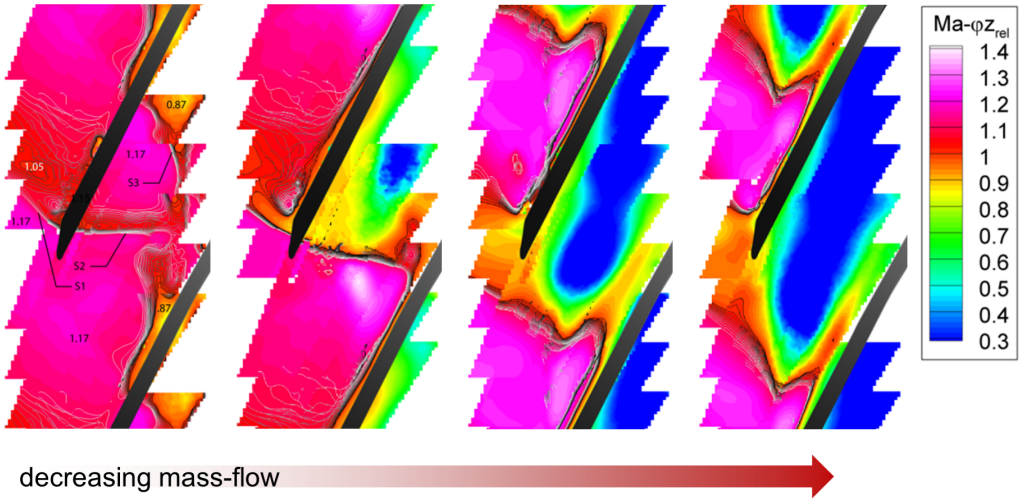

Figure 4.3: Evolution of Blockage zone at 92% channel height with throttling from near-choke to near-stall, second to left represents Peak Efficiency in Fig. 4.1

It was found that due to this spillage of fluid around the leading edge, small vortices with radial rotation axis evolve and propagate upstream of the blockage zone created by tip-leakage flow from blade to blade. In Fig. 4.4 a raw image of these measurements is shown, together with the derived velocity vectors indicating the shape of the radial vortex. These phenomena have been heavily discussed in literature but were never observed before in a high-speed machine. A detailed description of the findings is presented in (Brandstetter et al., 2018) and (Brandstetter and Schiffer, 2017).

4.2 High-speed compressor: Lock-in with vibration mode

4.2.1 Experimental results

At the same time as the radial vortices, high amplitude vibrations were detected in this machine which could not be explained as stall induced vibrations or flutter. The conventional post-processing methods were extended to enable the simultaneous characterization of flow-field disturbances and blade vibrations. This included the synchronization of strain-gauge and tip-timing measurements to resolve blade-individual vibrations, unsteady wall-pressure measurements above the rotor and unsteady PIV-measurements. Furthermore, a correlation between the vibration phase and amplitude of a torsional blade oscillation and the flow field around the leading edge could be determined. These results have been presented by Brandstetter and Schiffer (2017).

In Figure 4.5 (a), the position of the measured disturbances between the leading edges is shown for the PIV and the wall-pressure measurement, showing a clear correspondence. During a transient measurement, starting at a stable near-stall condition approaching the stability limit, the number of disturbances increased as depicted in the upper graph of Fig. 4.5b. At the same time, the spatial

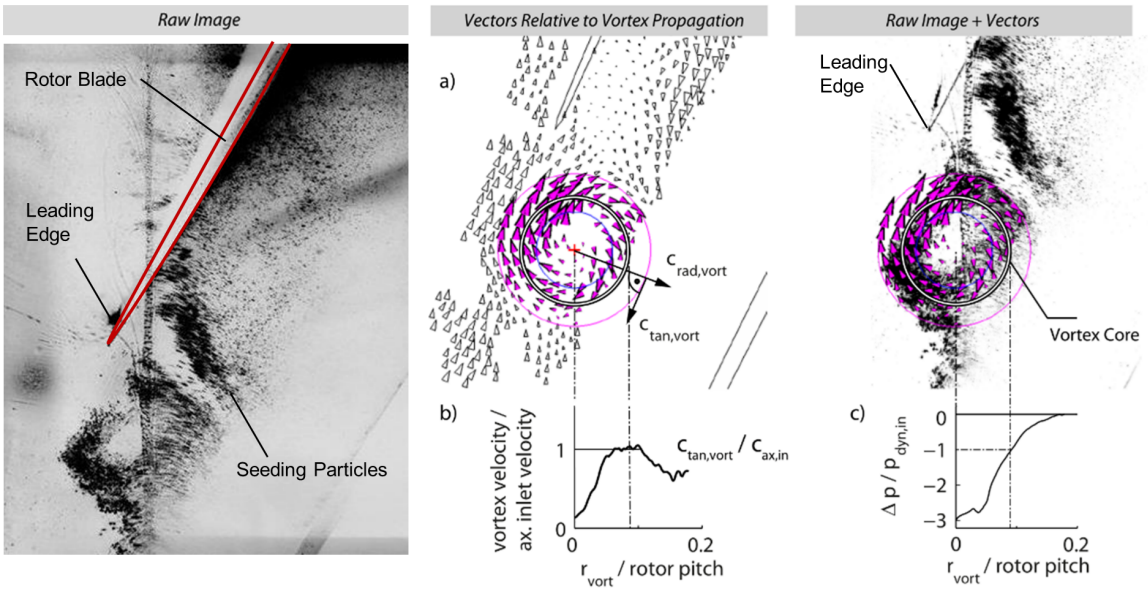

Figure 4.4: Evolution of Blockage zone at 92% channel height with throttling, ensemble averaged results, (Brandstetter et al., 2018)

distribution changes from erratic or random occurrence to a clearly structured, phase locked pattern that corresponds to the development of a singular circumferential wave number. As presented in the top graph of Fig. 4.6a, the rotor blade vibration amplitude rises during this throttling manoeuvre, and this coincides in time with the rise in count of aerodynamic disturbances and switch to a single wave number seen in Fig. 4.5.

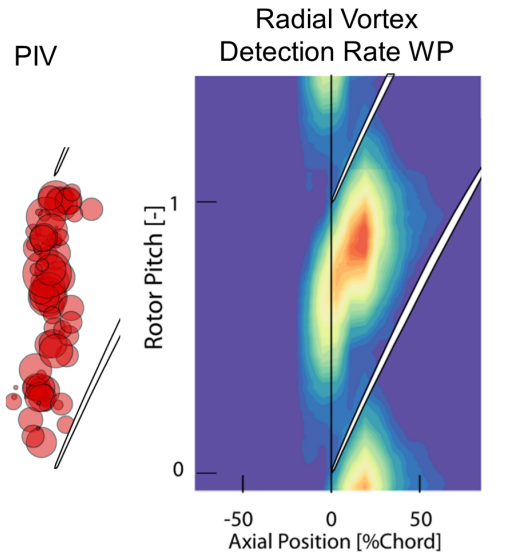

(a) Radial vortex detections in PIV and wall-pressure measurements

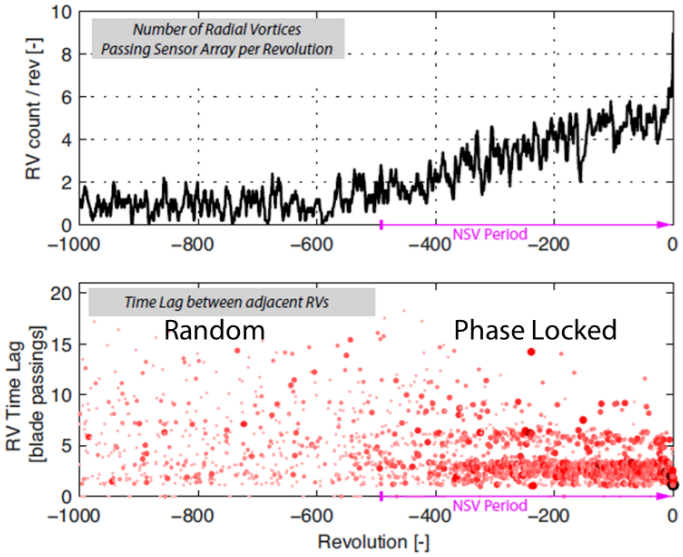

(b) Count of radial vortices per revolution and spatial distribution

Figure 4.5: Measurements of radial vortices, Images from (Brandstetter et al., 2018)

Through a method of cross-correlating multiple pairs of unsteady wall pressure sensors distributed around the circumference (see also section 5.2), the propagation speed of the disturbances was calculated. This is shown in the bottom graph of Fig. 4.6a. It is seen that the aerodynamic disturbances propagate at a constant speed around the circumference before the onset of vibrations, but occur less intense and erratically. Through slow throttling of the machine, intensity of the disturbances increased while blade vibration amplitude started to rise. Eventually, the rotor developed a vibration

pattern with a fixed phase angle between adjacent blades. A regular spatial distribution of aerodynamic disturbances developed together with a slight shift in propagation speed as seen in Fig. 4.6 a) . For the presented case, the aerodynamic disturbances travel backwards in the rotor frame of reference with about half the tip-speed while the corresponding blade vibration pattern is traveling in opposite direction due to aliasing with the number of rotor blades, illustrated in 4.6 b) (Aerodynamic Wave Number N_a =13, Structural Nodal Diameter N_v =8, aliasing at N_b =21 Blades).

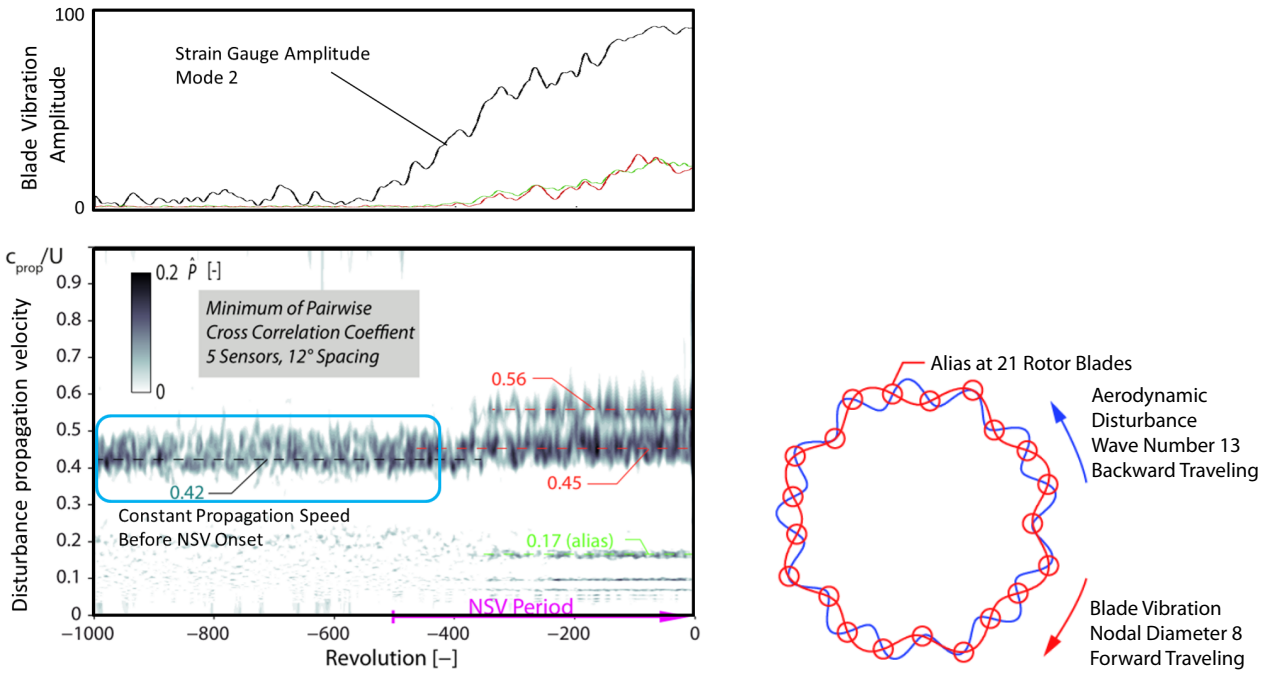

(a) Rotor blade vibration amplitude and propagation speed of aerodynamic disturbances during transient throttling

(b) Coherent interaction between aerodynamic disturbance and blade vibration after lock-in

Figure 4.6: Lock-in of aerodynamic disturbances and blade vibration during NSV (Brandstetter et al., 2018)

4.2.2 Computational results

To further investigate the lock-in phenomenon, unsteady numerical simulations have been carried out. Details are provided by Stapelfeldt and Brandstetter (2020). The objectives of the simulations were to quantitatively and qualitatively determine the relationship between the convected disturbance detected in the measurements and blade vibrations, and to determine its sensitivity with respect to operating point, vibration amplitude and relative phase between vibration and disturbance.

Rather than modelling the full 1.5 stage domain, a reduced model was built to facilitate a parametric study. The computational domain, shown in Fig. 4.7, comprises five rotor blade passages.

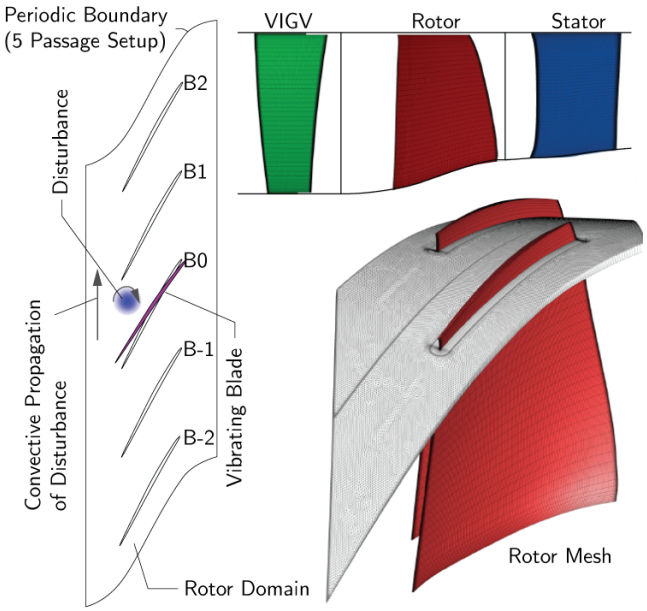

Figure 4.7: Computational domain for steady and unsteady simulations and detail of rotor mesh, (Stapelfeldt and Brandstetter, 2020)

Two operating conditions have been studied, first OP1, denoted in Fig. 4.8 a) representing a point where the compressor could be operated safely in the experiment without significant vibrations and OP2 as a condition where NSV was observed. Fig. 4.8b presents the relative Mach number close to the casing for these two operating conditions, showing an extensive blockage zone developing in the blade passage. Comparison with the PIV measurements at an operating point between OP1 and OP2 shows a remarkable agreement with the average flow conditions in the simulations, indicating that the blockage situation due to tip leakage flow is well represented numerically.

Starting from steady RANS solutions, harmonic oscillation of one blade in the first torsional mode was prescribed in the simulation. In the time marching solution, vortical aerodynamic disturbances evolved at the leading edge of the oscillating blade as shown in Fig. 4.9 for the experimental measurement plane at 92% span. During the shown oscillation cycle, the disturbance travels in circumferential direction towards the trailing blade.

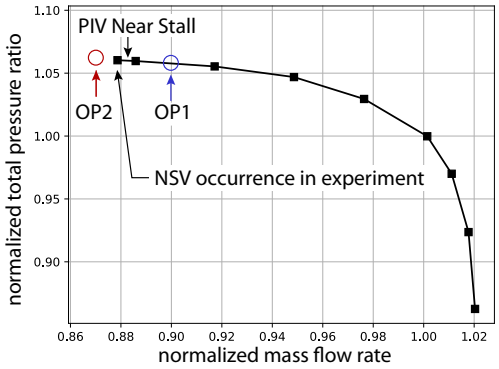

(a) Measured and calculated compressor characteristics, values normalized with aerodynamic design point

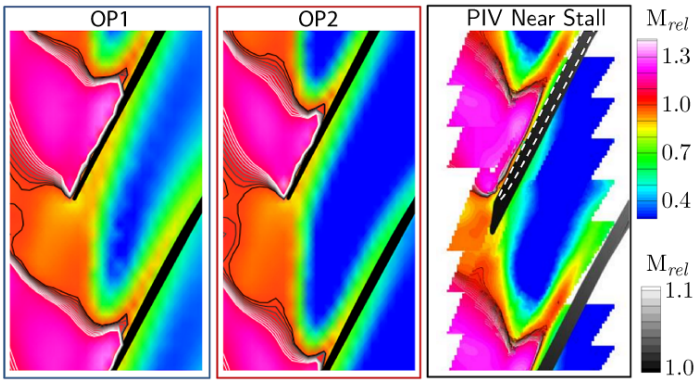

(b) Comparison of relative Mach number at OP1 and OP2 at 92% Span (pseudo-colours for whole Mach-Number range, grey isocontours in low supersonic range indicating shock structure)

Figure 4.8: Validation of numerical simulations with experimental data (Stapelfeldt and Brandstetter, 2020)

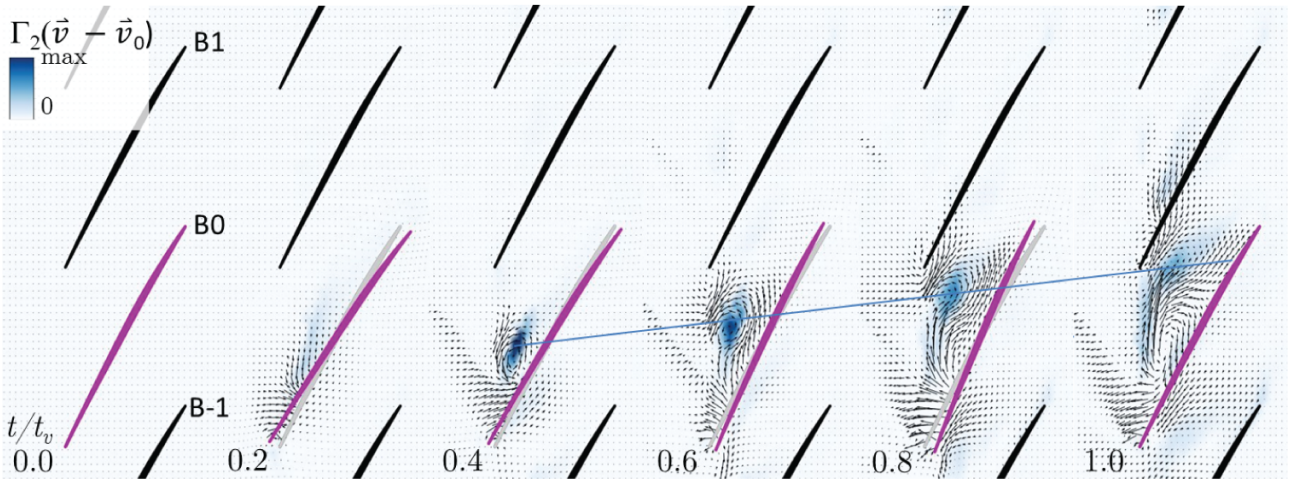

Figure 4.9: Development of propagating disturbance during one blade oscillation cycle; unsteady velocity vectors and contour map of vortex criterion Γ_2 after al. Graftieaux et al. (2001), image from (Stapelfeldt and Brandstetter, 2020)

In order to understand coupling with the structure, the influence of the disturbance on the blade forcing was determined. The vortical disturbance was quantified by measuring circulation in a mid-passage control volume on the 2D measurement plane. Figure 4.10a shows the temporal evolution of the convected circulation in the blade passage for all blades. It can be seen how the disturbance, emitted from Blade 0 takes a time of approximately 10 blade passages (t_{bp}) to pass the domain and arrive again at Blade 0. For OP1, the disturbance has decayed to a negligible level, at OP2 the amplitude remains significant and accumulates with newly emitted circulation. For both cases it was found that the modal forcing on the blade was time and amplitude coherent to the convected circulation in the middle of the passages as illustrated in Fig. 4.10b for OP2.

The influence of the operating point was further quantified by measuring the amplitude of the circulation in the different blade passages. Fig. 4.11 shows a rapid decay of the disturbance as it travels around the circumference at OP1 whereas at the higher throttled condition OP2, the disturbance amplitude approaches a constant level. In both cases, the propagation speed was identical. The low decay rate of the disturbance at OP2 leads to an accumulation in the leading edge plane, which is discussed in detail in (Stapelfeldt and Brandstetter, 2020). Most importantly, the evolution of the decay rate with throttling of the machine corresponds to the experimental observations discussed above.

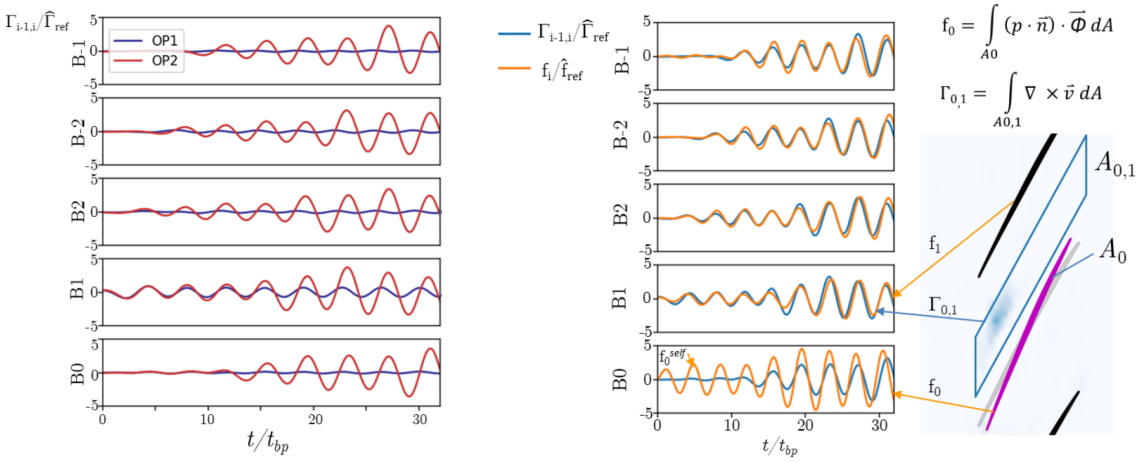

(a) Convected circulation, Comparison OP1 and OP2

(b) Correlation between convected free circulation and modal forcing at OP2

Figure 4.10: Temporal evolution of convected disturbance and modal forcing for all blades in the domain, Blade 0 vibrating with an amplitude of 1°

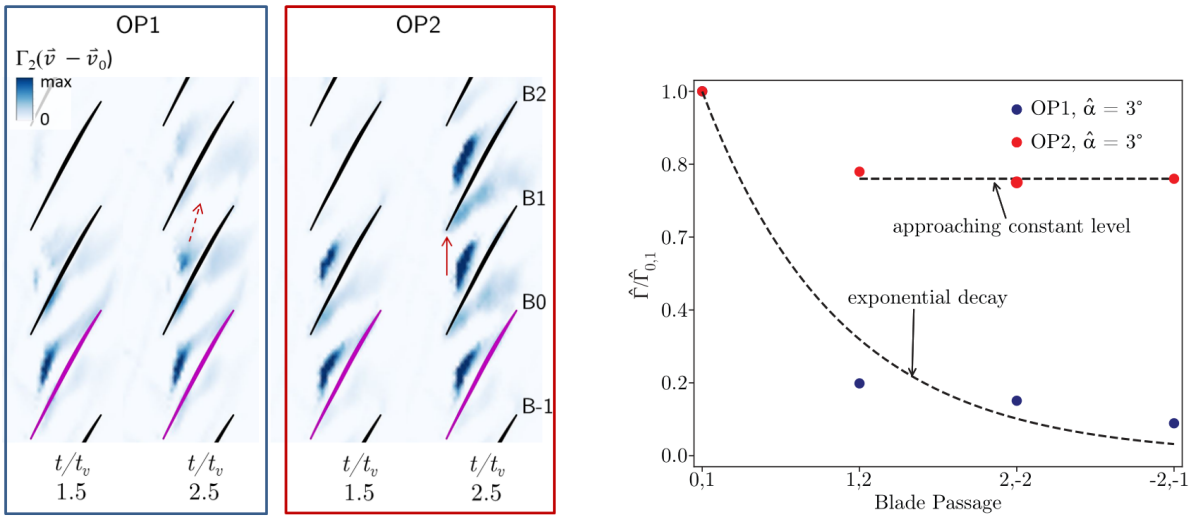

(a) Convective propagation of disturbance, comparison OP1 and OP2, vibrating blade B0, (Stapelfeldt and Brandstetter, 2020)

(b) Passage-to-passage variation in disturbance amplitude, Comparison OP1 and OP2 for modal deflection amplitude $\alpha = 3°$ at blade tip)

Figure 4.11: Disturbance propagation in numerical simulations (Stapelfeldt and Brandstetter, 2020)

4.2.3 Low speed composite fan: Lock-in phenomenon

A comparable phenomenon was recently observed at a fan test facility at Ecole Centrale de Lyon for a fundamentally different setup of a low-speed composite-material fan that is representative of a modern Ultra High Bypass Ratio engine. The test facility ECL-B3 presented in Fig. 4.12 is a completely new test platform that has been realized in cooperation between École Centrale de Lyon and Safran Aircraft Engines as part of the ANR – EQUIPEX program. The facility has been commissioned in 2017 and successfully used for the investigation of a state-of-the-art fan stage (Safran Marlysa Montage 0+) derived from the CFM International LEAP engine. The results presented in the following have been obtained from a technology demonstrator for a modern UHBR fan that was investigated within the European funded project FP7 ENOVAL (GA: 604999).

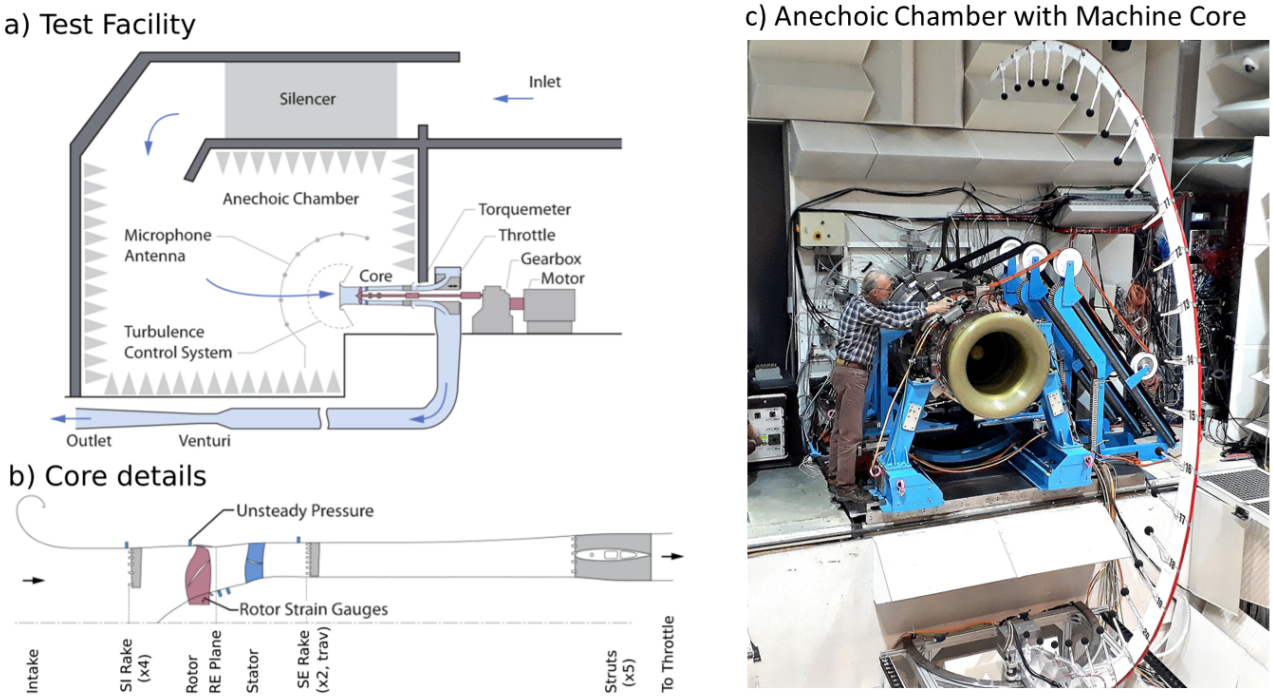

Figure 4.12: ECL-B3 test facility for UHBR Composite Fans

The rotor is driven by an electric motor at a rotation speed of approximately 16000 rpm. The machine is operated in an open cycle. Through a set of silencers, air is sucked in from the roof and led to the anechoic chamber containing the actual machine. In order to measure the mass flow, a Venturi-nozzle is installed after a 25m long circular tube section which is relevant for the results presented in section 5.1. The inner core design is depicted in Fig. 4.12 b). To reduce complexity, the setup does not separate bypass and core flow. Instead, the original stator has been modified to provide representative conditions at the rotor exit with just a single flow channel. The whole flow-section between fan-stage and throttle is equipped with acoustic liners and specifically designed to reduce interactions with facility components. Hence the test case provides optimal conditions for the rotor to develop disturbances without being affected by upstream installations.

Using unsteady wall pressure instrumentation combined with rotor strain gauges during transient throttling manoeuvres, non-synchronous vibrations have been observed with the same characteristics as for the HPC compressor described before. Between the rotor leading edges, flow disturbances propagate around the circumference and interact with the rotor blades (Rodrigues et al., 2021). In Fig. 4.13 the fluctuation of the pressure field above the rotor blades is presented for different operating conditions denoted in the attached characteristic. At highly throttled condition OP6 the pressure fluctuations between the leading edges achieve a high level of 10% of the mean value, which is comparable to the HPC results from Brandstetter et al. (2018). At the same time, significant blade vibration amplitudes were measured, particularly in the 3rd blade eigenmode. It was found that for several

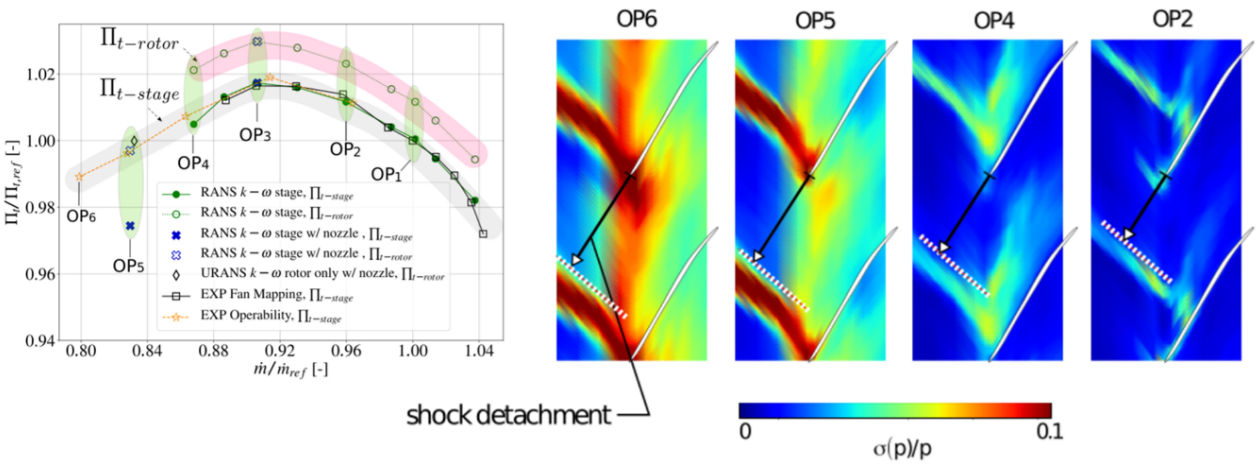

Figure 4.13: Pressure rise characteristic and unsteadyness (relative standard deviation) of wall pressure field at design speed for low-speed fan, (Rodrigues et al., 2021)

speedlines between 60% and 100% a consistent phenomenon of a backward traveling aerodynamic disturbance in resonance with a structural vibration mode is present. The maximum amplitude of the vibration was measured at 80% speed, shown in Fig. 4.14a which reached safety critical limits. Analysis of the dominant wave numbers, presented in Fig. 4.14b shows a continuous evolution with the rotor speed. It was found, that the relative propagation speed of the aerodynamic disturbance is mostly independent of the speedline for all experiments (54% - 60 % of the rotor speed, $\Omega_a^S/\Omega_r = 0.54..0.6$). As the eigenfrequency of the relevant blade mode ω_v^R can also be considered constant, the wave number N_a decays with the rotor speed Ω_r according to $N_a = \omega_v^R/\Omega_a^R = \omega_v^R/(\Omega_r - \Omega_a^S)$ in Fig. 4.14b. In all cases, the backward traveling aerodynamic disturbance aliases with the 16 rotor blades to the Nodal Diameter of the structural vibration ($N_{v,Mode3} + N_a = 16$), corresponding to rising evolution with the rotor speed in Fig. 4.14b. As the propagation speed of the aerodynamic disturbances is independent of the operating condition, these results, obtained within the PhD thesis of Martin Rodrigues, indicate the same convective lock-in phenomenon described above for the HPC compressor.

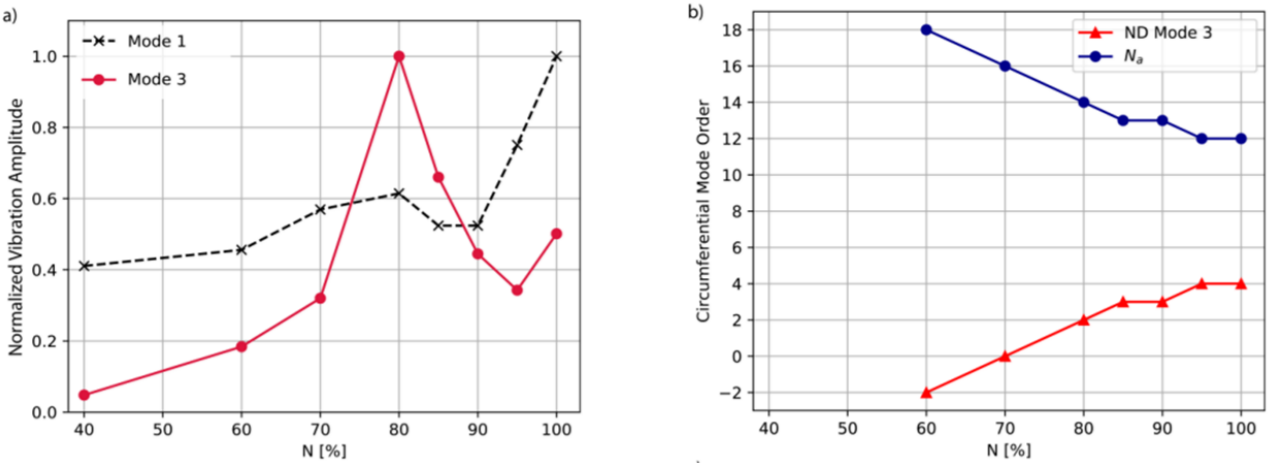

Figure 4.14: a) Amplitude of Non-Synchronous-Blade Vibration at highly throttled conditions for different rotor speeds, b) Circumferential mode order of dominant aerodynamic disturbance (N_a) and corresponding nodal diameter of blade Mode 3, from Martin Rodrigues et al. (2021)

A deeper analysis of the characteristics of the observed disturbances is presented in (Brandstetter et al., 2020). Here, the decay rate of the convective disturbances was analyzed, depending on wave number and interaction with rotor blades. It was found that disturbances which are not locked in with

structural vibrations decay with a half-life of approximately 0.5 revolutions, meaning that a significant amount of more than 20% of initial disturbance travels around the circumference multiple times. After lock-in, the decay rate reduces even further. As will be discussed in section 4.5.1 this low decay rate is the dominant factor that determines the sensitivity of the system to develop critical non-synchronous vibrations.

These results are of high relevance, as typically the operating range of fans is limited either by rotating stall or flutter. The fan investigated here represents a novel type of low-speed transonic fans which are scarcely described in literature. The occurrence of NSV was not anticipated and the typical countermeasures against flutter which have been considered in the design of this machine are obviously not effective to suppress this type of aeroelastic instability. The fact that the phenomenon occurs at multiple speeds and is most severe at 80% is not understood yet and subject of our current investigations.

4.2.4 Summary: Physical mechanisms driving convective NSV

The above investigations have discovered that NSV is a phase-lock between structural vibrations and aerodynamic disturbances. It is fundamentally different to self-excited flutter, as the disturbances exist without vibration. These findings received noticeable attention from the community as the problem has been observed in numerous studies but could not be explained comprehensively before. As will be described in the following sections, the characteristics of the phenomenon require specific considerations to develop countermeasures, but the fact that the propagation speed is independent of the spatial distribution and lock-in with a structural vibration mode occurs provides the possibility to predict the coupled system behavior in a reduced order model. However, accurate numerical simulation of the phenomenon, to calibrate the model remaines challenging, as discussed by Stapelfeldt and Brandstetter (2020) and in the following.

4.3 Development of semi-analytical model

The presented experimental and computational results on NSV indicate that the vibration is caused by aerodynamic disturbances which develop near the leading edge close to the casing. The vortical disturbance convects from blade to blade in the circumferential direction. This generates aerodynamic forcing on the blades which is proportional to the change in circulation due to convected vorticity. Without blade vibration the vortical structures are randomly distributed in time and space but travel at a constant circumferential velocity set by the flow field. Through interaction with oscillating blades an organized pattern develops such that the phase velocity of the vibration mode matches that of the aerodynamic disturbance. This is achieved through adjustment of the circumferential wave number and a slight shift of propagation speed. The process is a lock-in of fluid and structure, and was dominantly observed for torsional blade vibration modes.

4.3.1 Model formulation in time-domain

Based on these physical mechanisms, a semi-analytical model to predict the phenomenon was developed in cooperation with Sina Stapelfeldt from Imperial College London. The experiments on the HPC compressor described in (Brandstetter et al., 2018) were taken as a reference case. Schematically the model is shown in Fig. 4.15.

The model uses single-degree of freedom mass oscillators to represent blades on a rigid disk. In its simplest form, the individual blades are tuned and structurally uncoupled but aerodynamically coupled by a forcing term. The equation of motion for this system is given by:

$$\ddot{\boldsymbol{q}}(t) + D\dot{\boldsymbol{q}}(t) + K\boldsymbol{q}(t) = \boldsymbol{F(t)} \tag{4.1}$$

where q is the modal displacement, D and K are the diagonal damping and stiffness matrices and F is the mass-normalized modal force. The following will derive an expression for the forcing term based on the conclusions from the experimental and numerical studies described above.

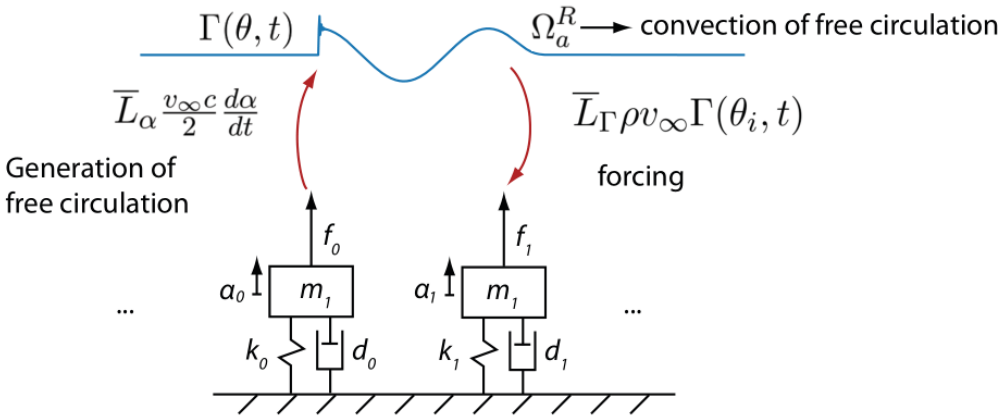

Figure 4.15: Schematic of Semi-analytic model, (Stapelfeldt and Brandstetter, 2020)

It was demonstrated, that the behaviour of the 3D rotor blades undergoing torsional motion could be adequately modelled in a quasi 2D analysis, considering the twist of a spanwise section. In this case, the modal force can be approximated by the moment induced by the unsteady lift and the modal displacement q can be replaced with twist of the blade $\alpha \propto q$. If the changes in the location of the centre of pressure are negligible, the simplified equation of motion for the system becomes:

$$\ddot{\boldsymbol{\alpha}}(t) + D\dot{\boldsymbol{\alpha}}(t) + K\boldsymbol{\alpha}(t) = c_1 \boldsymbol{L'(t)} \tag{4.2}$$

where c_1 is a constant of proportionality between the 2D unsteady lift, L', and 3D mass-normalised modal force.

Since the aerodynamic disturbance can be quantified in terms of convected vorticity, the modal force term on the right hand side can be further specified. It was shown that it can be considered as a superposition of the force induced directly by the blade oscillation and that caused by the circumferentially propagating vorticity disturbance. A few simplifying assumptions using the model of Theodorsen (1949) to approximate the unsteady lift due to blade twist, and the Kutta-Joukowski theorem to approximate the force induced by a travelling disturbance result in the following equation of motion:

$$\ddot{\boldsymbol{\alpha}}(t) + D\dot{\boldsymbol{\alpha}}(t) + K\boldsymbol{\alpha}(t) = \underbrace{\frac{1}{2} c_1 \rho v_\infty^2 c \tilde{L}_\alpha \boldsymbol{\alpha}(t)}_{\text{force due to vibration}} + \underbrace{c_1 \rho v_\infty \tilde{L}_\Gamma \boldsymbol{\Gamma}(t)}_{\text{force due to convected disturbance}} \tag{4.3}$$

where ρ is the density, v_∞ is the relative inlet velocity, c is the blade chord. The coefficient $\tilde{L}_\alpha$ models the unsteady aerodynamic response of the blade. Like Theodorsen's function, it is a function of the reduced frequency k and operating point but for simplicity, we assume a constant operating point and tuned system to drop these dependencies. In the second term on the right hand side, $\tilde{L}_\Gamma$ is a complex constant modelling the change in amplitude and phase relative to the quasi-steady force induced by the convected vorticity disturbance. This is a function of reduced frequency and blade deflection amplitude but is assumed to be constant here, since the reduced frequency is kept constant and the blade deflections are assumed to be small.

By assuming a constant angular velocity of the disturbance, Ω_a^R, the following one-dimensional equation can be derived, describing the rate of change of circulation in fixed control volumes placed around the circumference:

$$\frac{d\Gamma}{dt} = -\Omega_a^R \frac{\partial \Gamma}{\partial \theta} + \frac{\nu}{R} \frac{\partial^2 \Gamma}{\partial \theta^2} + \dot{\Gamma}_S(\theta, \alpha(t)) + \dot{\Gamma}_{sink} \tag{4.4}$$

where $\dot{\Gamma}_{sink}$ is a sink term, describing the loss of vorticity axial out of the domain and $\dot{\Gamma}_S$ is the source term modelling the generation of vorticity on the oscillating blades. The first two terms on the right hand side represent convection and diffusion of the disturbance.

Ω_a^R	propagation speed of disturbance
$\overline{L}_\alpha$	Transfer from modal oscillation to lift on oscillating blade
$\overline{L}_\Gamma$	Transfer from convected circulation to lift
$\dot{\Gamma}_{sink}$	Loss of circulation due to axial convection and diffusion, generally a non-linear function, linear approximation valid for vibration amplitudes $\hat{\alpha} < 1°$

Table 4.1: Parameters and their purpose in the semi-analytical model

Together with Eq. 4.3 this forms a coupled system. The bi-directional interaction between the disturbance and an oscillating rotor blade arises from the source-term $\dot{\Gamma}_S$ in Eq. (4.4) and the second forcing term in Eq. (4.3). The convection of the circulation couples the different rotor blades aerodynamically.

In the computational model used to study NSV, the vorticity disturbance was generated by the oscillating blades ($\Gamma \propto \dot{\alpha}$), such that both terms on the right hand side depend on the blade vibration. In Fig. 4.10b this dependency is clearly visible through comparison of the modal force on the vibrating blade B0 and the remote blades. Before the disturbance has traveled through the domain ($t < 10t_{bp}$) Blade 0 already experiences harmonic modal forcing due to its own oscillation (self-forcing). The remote blades are only forced as soon as the disturbance arrived. For $t > 15t_{bp}$ the forcing on Blade 0 has reached a novel constant amplitude resulting from the superposition of self forcing and the convected disturbance it emitted more than one domain traversal earlier. Hence, the semi-analytic model comprises a conservation term for the aerodynamic disturbance which is continuous around the circumference that allows the disturbance to traverse the domain multiple times before decaying.

The model itself only contains 4 remaining parameters which are calibrated with the unsteady numerical simulations as denoted in Tab. 4.1. Ω_a^R and $\dot{\Gamma}_{sink}$ depend on the operating condition (time average flow field), $\overline{L}_\alpha$ and $\overline{L}_\Gamma$ are characteristics of the blade profile.

4.3.2 Validation and interpretation

In (Stapelfeldt and Brandstetter, 2020) we show how the calibrated model accurately reproduces the temporal evolution of modal forcing for the 5 Passage setup with only one oscillating blade. After validation against the CFD results, the model was applied to the same test case but the blade movement is not prescribed and all 21 blades are included.

The unsteadiness is triggered with an initial disturbance at Blade 16 and the resulting blade displacements and disturbance locations are tracked. Figure 4.16 presents the time history of the solution, with the blade oscillations shown as red lines and the track of the propagating disturbances in grey. It can be seen that the disturbance from Blade 16 propagates in circumferential direction and excites the trailing blades. After approximately two revolutions the initial disturbance has travelled around the circumference.

Every time the disturbance interacts with an oscillating blade, its path is slightly shifted. A zoomed view of this interaction is shown in Fig. 4.17a. Here the shift of the disturbance at each interaction is clearly visible. This leads to a change of the global propagation speed, which is recorded in Fig. 4.17b. It clearly shows the acceleration after the first domain traversal. After approximately 6 revolutions, the propagation speed stabilizes to a value approximately 2.5% higher than the free propagation speed. At this point the system is considered locked in.

The frequency and inter-blade phase angle ($\sigma_a = 2\pi N_a/N_B$) of the aerodynamic disturbance match those of the structural vibration:

$$\omega_{v,lock} = \omega_{a,lock} = N_a \Omega_{a,lock}^R \tag{4.5}$$

$$\sigma_v = \sigma_a \rightarrow N_v \equiv N_a \pmod{N_B} \tag{4.6}$$

In other words, a coherent aerodynamic disturbance and structural nodal diameter pattern are established. The model has shown that this lock-in is achieved by adjustment of the global propagation speed, Ω_a^R, and selection of a matching nodal diameter pattern and aerodynamic wave number. The

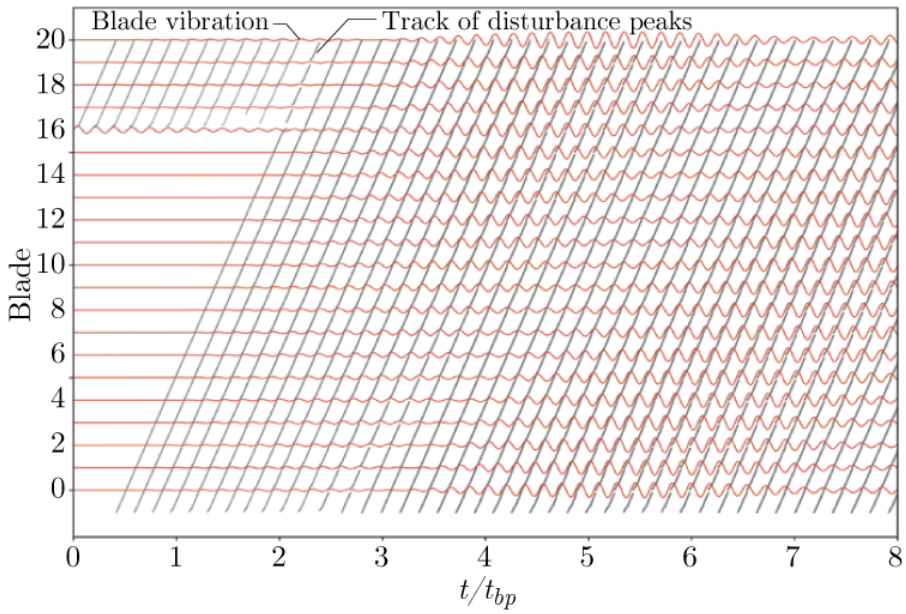

Figure 4.16: Disturbance evolution over 8 revolutions as predicted by semi-analytical model for 21-bladed rotor. Initial disturbance at Blade 16: 1°, $\Omega_a^S = 0.5\Omega_r^S$.

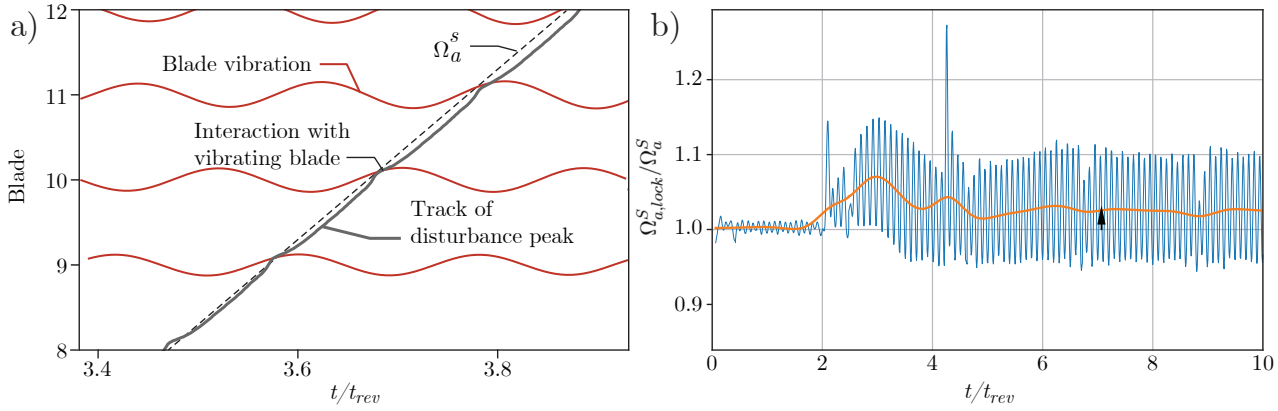

Figure 4.17: Solution of semi-analytic model

vibration mode and shift in propagation speed match those of the experiment, $N_a = 13, N_v = 8, N_B = 21$.

4.3.3 Applicability to other compressors and fans

Although the model coefficients have been tuned for the high-pressure compressor investigated in Darmstadt, the author found that it was useful for analysing the stability of different machines. This is for two reasons; Firstly, the model illustrates general trends observed during sweeps of the non-dimensional parameters known to be most influential to NSV, and the qualitative results are considered general. Secondly, the coefficients and parameters do not appear to vary significantly from machine to machine. The force coefficients have a minor effect on stability as shown in (Brandstetter and Stapelfeldt, 2021), and were found to be similar for HPC compressors (Stapelfeldt and Brandstetter, 2020) and low-speed fans (Rodrigues et al., 2021). Propagation speeds are around 50% rotor speed for a number of different machines (Baumgartner et al., 1995; Kielb et al., 2003; Thomassin et al., 2011; Dodds and Vahdati, 2015). The model with the coefficients shown here, was able to able correctly predict the unstable nodal diameter for a number of cases from literature, listed in Table 4.2.

	N_B	Ω_a^R/Ω_r	ω_v^R/Ω_r	$\sigma_{v,exp}$	$N_{v,exp}$
Baumgartner et al. (1995) **trans. multist. HPC**	27	−0.36	7.56	80°	6
Kameier and Neise (1997) **low speed axial fan**	24	−0.6	22.2	165°	11
Brandstetter et al. (2018) **trans. sing. stg. HPC**	21	−0.44	5.8	137°	8
Rodrigues et al. (2021) **transonic fan**	16	−0.42	5.46	67.5°	3

Table 4.2: NSV cases from literature successfully captured by the model

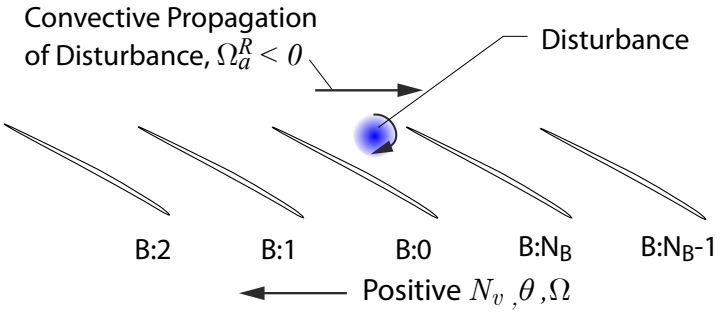

Figure 4.18: Sketch of rotor indicating blade numbering and sign convention

4.4 Linearisation of the semi-analytical model for stability analysis in the frequency domain

4.4.1 Formulation in the frequency domain

In the model presented above, the aerodynamic forcing results only from the blade vibration and is linearly dependent on the blade vibration amplitude. Under some assumptions, it is possible to recast the model into the frequency domain and predict stability using eigenvalue analysis. To do this, we derived an expression for the forcing term based on the assumptions of harmonically oscillating blades and a harmonic aerodynamic disturbances.

To simplify the derivation, the original model:

$$\ddot{\boldsymbol{\alpha}}(t) + D\dot{\boldsymbol{\alpha}}(t) + K\boldsymbol{\alpha}(t) = \frac{1}{2}c_1\rho v_\infty^2 c\overline{L}_\alpha \left[\boldsymbol{\alpha}(t) + \overline{L}_\Gamma \boldsymbol{\Gamma'}(t)\right] \tag{4.7}$$

is written as:

$$\ddot{\boldsymbol{\alpha}}(t) + D\dot{\boldsymbol{\alpha}}(t) + K\boldsymbol{\alpha}(t) = \boldsymbol{F_v(t)} + \boldsymbol{F_a(t)} \tag{4.8}$$

where F_v is the force due to the blade vibration and F_a is the force generated by the aerodynamic disturbance. At first sight, this resembles a forced response case. However, above we chose the disturbance to be generated by the blade vibration, such that the distinction between F_v and F_a is not clear. The distinction is discussed in detail in (Brandstetter and Stapelfeldt, 2021), and will be demonstrated in the following, where expressions for F_v and F_a in an assembly of N_B harmonically oscillating blades are derived.

We assume that the rotor blades are vibrating at an angular frequency ω_v^R in the rotor frame of reference, in nodal diameter N_v, such that the structural inter-blade phase-angle is given by $\sigma_v = 2\pi N_v/N_B$. The force due to vibration F_v, can hence be written as:

$$F_v(t) = \tilde{F}_v e^{i\omega_v^R t} \tag{4.9}$$

The aerodynamic disturbance has circumferential propagation speed Ω_a^R in the rotor frame of reference. The sign convention is such that a positive circumferential direction is in the direction of rotation and therefore $\Omega_a^R < 0$ as illustrated in Fig. 4.18. It is being emitted at frequency ω_a in the rotor frame of reference. This could be, for example, vorticity being shed from one blade as a result

of an aerodynamic instability but it could also be due to vibration in an structural eigenfrequency ω_v. Since it is difficult to induce sufficiently small variations to cause local vortex shedding, the CFD simulations used to calibrate the model in (Stapelfeldt and Brandstetter, 2020), relied on vibration as a disturbance trigger, so we will consider the special case where the aerodynamic disturbance is being emitted from a vibrating blade and $\omega_a = \omega_v$.

Assuming unattenuated disturbance propagation, the force due to the aerodynamic disturbance is a superposition of the disturbances originating from N preceding blades. Note that N here is the number of blades that have an influence on Blade 0, which is not necessarily equal to N_B. In (Brandstetter and Stapelfeldt, 2021), it is shown that the force due to the aero-disturbance hence takes the shape:

$$F_a(t) = \sum_{n=0}^{N-1} \tilde{F}_a^* e^{i(\omega_v t - n\sigma_v - n\sigma_a)} \tag{4.10}$$

where $\tilde{F}_a^*$ is the complex constant representing the relationship between the incoming aerodynamic disturbance and the aerodynamic forcing experienced by a blade. The difference in phase between the forcing resulting from the N blades is the sum of the structural and aerodynamic inter-blade phase angle:

$$\sigma_v = \frac{2\pi N_v}{N_B} \tag{4.11}$$

$$\sigma_a = \omega_v T = -\frac{2\pi\omega_v}{N_B \Omega_a^R} \tag{4.12}$$

In reality, the aerodynamic disturbance will attenuate while travelling around the circumference as vorticity is not convected purely circumferentially but also axially out of the domain. Assuming an exponential decay, the amplitude of the disturbance is modelled as $\hat{F}_a(n) = \hat{F}_a^* e^{-nr_a}$, such that the expression for $F_a(t)$ becomes:

$$F_a(t) = \sum_{n=0}^{N-1} \tilde{F}_a^* e^{-nr_a} e^{i(\omega_v t - \sigma_{v,n} - n\sigma_a)} \tag{4.13}$$

$$= \sum_{n=0}^{N-1} \tilde{F}_a^* e^{-nr_a} e^{-i(\sigma_{v,n} + n\sigma_a)} e^{i\omega_v t} \tag{4.14}$$

4.4.2 Comparison to classical flutter

It is now possible to compare this to the classical flutter case, where $F_v(t) = \tilde{F}_v e^{i\omega_v t}$. To do this, we set the number of preceding blades to infinity, consistent with a periodic state. Equation 4.14 then becomes:

$$\begin{aligned} F_a(t) &= \tilde{F}_a^* e^{i\omega_v t} \sum_{n=0}^{\infty} e^{-nr_a} e^{-in(\sigma_v + \sigma_a)} \\ &= \tilde{F}_a^* e^{i\omega_v t} \left[\frac{1 - e^{-r_a} e^{-i(\sigma_v + \sigma_a)}}{1 - 2e^{-r_a}\cos(\sigma_v + \sigma_a) + e^{-2r_a}} \right] \end{aligned} \tag{4.15}$$

where the equality $\sum_{k=0}^{\infty} p^k e^{ikx} = [1 - pe^{ix}]/[1 - 2p\cos x + p^2]$ has been used. The sum of the inter-blade phase angles expressed in terms of nodal diameters and frequencies is:

$$\sigma_v + \sigma_a = 2\pi \left[\frac{N_v + \omega_v/\Omega_a^R}{N_B} \right] \tag{4.16}$$

Two differences between convective NSV and classical flutter become apparent in Equation 4.14 and 4.15. There are two distinct time-scales in the case of NSV: the vibration time scale and the aerodynamic, or convective, time scale, $n\sigma_a = -n\omega_v/(N_B\Omega_a^R)$. If the convective time scale is not

an integer multiple of the vibration period, the phase-lag between the aerodynamic disturbance and vibration modulates the forcing creating a beating signal. The amplitude of this will depend on the decay coefficient r_a. For a given r_a, the amplitude ratio $\hat{F}_a/\hat{F}_a^*$ will reach a maximum if $\omega_v = N_a\Omega_a^R$, as in a forced response function. This is shown in Fig. 4.19 for different decay coefficients, where the amplification for a fixed vibration frequency and range of propagation speeds Ω_a^R has been computed. However, unlike classical forced response, the aerodynamic excitation in this scenario depends on the vibration amplitude.

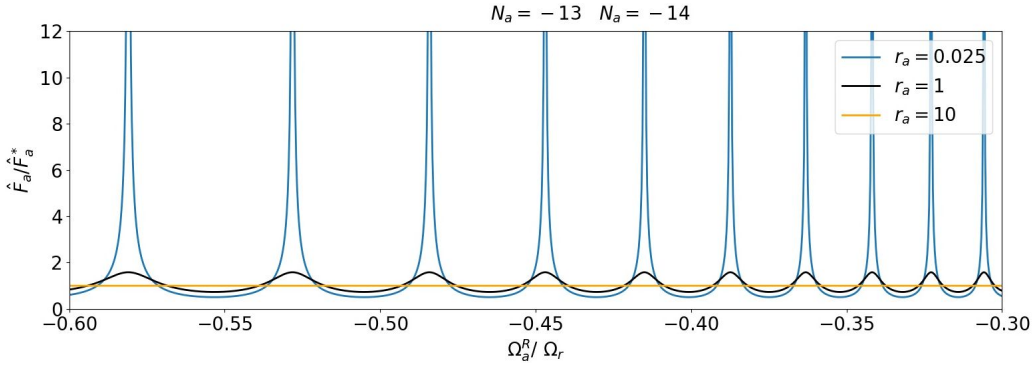

Figure 4.19: Amplification of disturbance for different decay coefficients.

The other difference results from the decay coefficient r_a. The value of r_a determines how many blades exert an influence on Blade 0. For low values of r_a, it is possible that an aerodynamic disturbance emitted from Blade 0 travels around the entire circumference and returns to Blade 0.

4.4.3 Formulation after lock-in

The numerical studies in Stapelfeldt and Brandstetter (2020) showed how lock-in of the disturbance and a vibration pattern is achieved through a phase-modulation of the disturbance when it is interacting with an oscillating blade, and establishment of a nodal diameter pattern such that the phase-speed of the aerodynamic disturbance matches that of the structure. In this case the resonance condition:

$$\omega_v = N_a\Omega_a^R \text{ where } N_a = \{1, 2, ..., n\} \tag{4.17}$$

is fulfilled, i.e. an integer number of aerodynamic wave lengths fits into the circumference. Using Eq. 4.16, we then see that:

$$\sigma_v + \sigma_a = 2\pi\frac{N_v - N_a}{N_B} = 2\pi m \text{ where } m = \{1, 2, ..., n\} \tag{4.18}$$

such that Equation 4.15 simplifies to:

$$F_a(t) = \tilde{F}_a^* e^{i\omega_a^R t}\frac{1}{1 - e^{-r_a}} \tag{4.19}$$

Considering a case where the disturbance rapidly decays over the circumference, i.e. $r_a \to \infty$, recovers the expression for classical flutter:

$$\lim_{r_a\to\infty} F_a(t) = \tilde{F}_a^* e^{i\omega_a t} \tag{4.20}$$

In the case of $r_a \to 0$ the aerodynamic forcing amplitude diverges even in the absence of a coupled fluid-structure instability.

The above analysis has examined the relationship between NSV and classical flutter. Equation 4.19 shows how, even after lock-in, when it is impossible to distinguish unsteadiness resulting from aerodynamics from that of vibration, the physics governing the system are different. In the case of NSV, the attenuation of a circumferentially propagating disturbance is low, while it is high in the case of

flutter. In other words, in the case of NSV a purely aerodynamic instability exists which is absent in the case of classical flutter.

To further illustrate the difference between NSV and flutter, it is useful to compare the above description to an aerodynamic influence coefficient (AIC) formulation which can then be used to analyse the stability of the system.

4.4.4 Analogy with classical AIC approach

When the number of preceding blades considered in the summation is less than the number of blades in the circumference $N \leq N_B - 1$, which is a valid choice for rapid decay of the aerodynamic disturbance, Eq. 4.14 becomes:

$$F_a(t) = \sum_{n=0}^{N-1} \tilde{F}_a^* e^{-nr_a} e^{i[\omega_v t - n(\sigma_v + \sigma_a)]} \tag{4.21}$$

Noting that the amplitude of the force is proportional to the blade modal velocity, because vorticity is being generated by the blade oscillation (Stapelfeldt and Brandstetter, 2020), and including the forces resulting from vibration on the vibrating blade itself, $F_v(t)$, this can be rewritten to resemble a classical aerodynamic influence coefficient formulation. In this case, the equation of motion for a given blade and inter-blade phase angle, σ_v, becomes:

$$\ddot{\alpha} + 2\zeta_v \omega_v \dot{\alpha} + \omega_v^2 \alpha = \tilde{C}_v \alpha + \sum_{n=0}^{N-1} \tilde{C}_{a,n_{\sigma_v}} \dot{\alpha}_n \tag{4.22}$$

where the first term on the right hand side represents the aerodynamic influence of the blade on itself and the sum contains the contribution of all other blades. When the solution for the modal displacement is assumed to be a complex exponential,

$$\alpha = \hat{\alpha} e^{\lambda t} \quad \text{where } \lambda = -\omega_v \zeta \pm i\omega_v \sqrt{\frac{\omega^2}{\omega_v^2} - \zeta^2} \tag{4.23}$$

such that the solution to the eigenvalue problem will give the aeroelastic frequency, ω and aerodynamic damping ζ. The blade influence coefficient relates to the aerodynamic force coefficient F_a^* as follows:

$$\begin{aligned} \tilde{C}_{a,n_{\sigma_v}} &= \frac{\tilde{F}_a^*}{\omega_v \hat{\alpha}} e^{-nr_a} e^{-n(\sigma_v + \sigma_a)} = \tilde{C}_a e^{-nr_a} e^{-n(\sigma_v + \sigma_a)} \\ \tilde{C}_v &= \frac{\tilde{F}_v}{\hat{\alpha}} \end{aligned} \tag{4.24}$$

In other words, the influence coefficient as derived from AIC simulations automatically incorporates the phase-lag and decay. It is normally obtained using CFD simulations without any knowledge of the physical mechanisms causing the aerodynamic coupling between blades.[1]

The comparison to the classical AIC approach clearly shows that in a locked-in state and for a sufficiently high decay of the disturbance around the circumference, the problem is equivalent to classical flutter and can be analysed using aerodynamic influence coefficients. The problem in the case of NSV, is how these influence coefficients are defined. Without sufficient decay, the aerodynamic disturbance will traverse the entire circumference and the coefficients will be time-dependent (on the number of revolutions of the disturbance). In this case, they are impossible to obtain using CFD simulations because the AIC paradigm is that the influence decays to zero with distance from the oscillating blade. Same applies to time-linearized simulations, where the differentiation of $\tilde{C}_v$ and $\tilde{C}_a$ cannot be derived.

[1] Note that, in the typical AIC analysis, the vibration inter-blade phase angle σ_v would not feature in the aerodynamic influence from Blade n to Blade 0 (as only one blade is vibrating). Instead, the complex blade-individual influence coefficient is transferred into the travelling wave space by a Fourier transform.

4.4.5 Validation of frequency model

The frequency domain model was applied to the transonic HPC compressor for the two operating points of interest. The coefficients were previously calibrated using reduced-domain CFD simulations at OP1 and OP2. Due to the low decay rate of the aerodynamic disturbance, a periodic solution does not exist and the force coefficients are time-dependent. The present analysis uses rounded values following calibration during the first few cycles of blade vibration, hence strictly speaking, the following analysis is not valid for OP2. These artificial coefficients help to illustrate the parameters driving NSV but the following is not to be interpreted as a frequency-domain solution of the NSV phenomenon.

Figure 4.20a shows the aerodynamic damping curves at the two operating points. While OP1 is stable, OP2 shows significant negative aerodynamic damping at $N_v 8$. This is associated with a large (3%) shift in frequency of the aeroelastic system relative to the in-vacuo frequency, as shown in Fig. 4.20b. This shift in frequency shows how the fluid-structure coupling modifies the phase-speed of the aerodynamic disturbance. This lock-in effect was also seen in the experiment and numerical simulations Brandstetter et al. (2018); Stapelfeldt and Brandstetter (2020). The results at OP1 (stable) and OP2 (instability at N_v=8) are in agreement with the experimental measurements and validate the frequency domain model. It is important to consider the frequency shift in future works using imposed harmonic blade oscillation in numerical simulations.

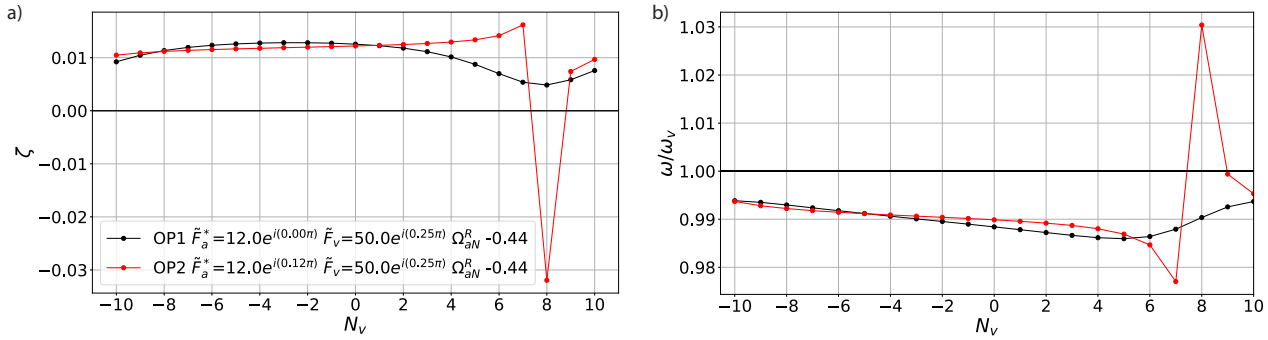

Figure 4.20: Aerodynamic damping versus nodal diameter for the experimentally tested operating points

4.5 Applications of the model

4.5.1 Sensitivity studies

The previous model application provided a prediction of the critical vibration mode for a known propagation speed, Ω_a^R. This can be approximated from steady state computations but it will differ from different rotational speeds and guide vane settings (Franke and Juengst, 2020).

If the propagation speed prediction is unknown or may be varied through VIGV scheduling, the model allows analysis for a range of propagation speeds, covering those measured in experiments and assuming that the tuned parameters (L_θ, L_Γ etc.) remain constant which is of course not strictly true. The graphs presented in Fig. 4.21 summarize the results of this variation in Ω_a^R from the time-domain model. Fig. 4.21a shows how the locked-in aerodynamic wave number varies with propagation speed, while Fig. 4.21b shows the resonant structural nodal diameter, i.e. the aerodynamic wave number aliased on the 21-bladed rotor. The size of the markers indicate the amplitude rise of the dominant vibration pattern. It can be seen how the actual wave number of the vibration jumps through variation of the propagation speed. This is also coherent with experimental observations, which showed alternating patterns for repeated measurements Franke and Juengst (2020).

In Brandstetter and Stapelfeldt (2021) we present a more detailed analysis of the influence of system parameters such as decay rate, propagation speed, amplitude and phase of the aerodynamic coefficients on the system stability using the formulation in the frequency domain. The analysis has shown that the results depend significantly on the disturbance attenuation over the circumference which is determined by the blockage in the tip region and therefore depends on the operating point.

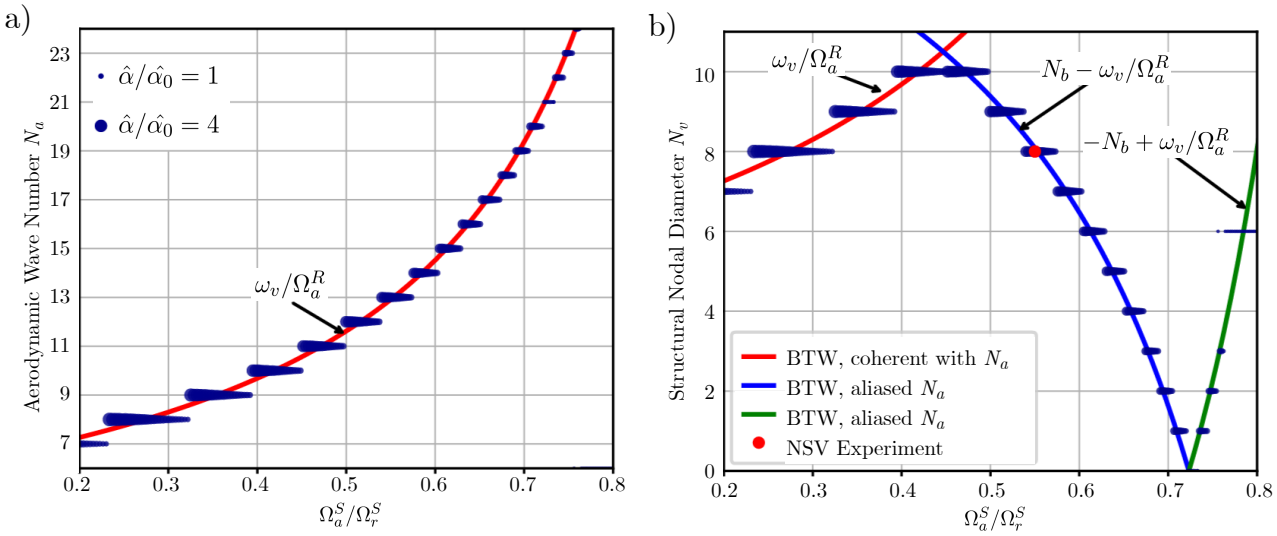

Figure 4.21: Predicted aerodynamic wave number (a) and excited structural nodal diameter pattern (b) for a range of free propagation speeds. Forward travelling (FTW) and backward travelling (BTW) waves as a result of aliasing on 21-bladed rotor. The experimental vibration mode is indicated. Symbol size represents average blade vibration amplitude $\hat{\alpha}$ after 20 revolutions

4.5.2 Use of the NSV-model for interpretation of measurement data

Since the time-marching model simultaneously contains convective and vibration frequencies, it can be used to replicate experimental pressure spectra. It enables the analysis of the temporal evolution of different quantities. This can aid the interpretation of measurement data.

In (Brandstetter et al., 2021a) we showed for the case of the low-speed-fan discussed in Section 4.2.3, that through induction of randomness in the aerodynamic disturbance term, a frequency analysis in the steady frame of reference produces a spectrum that is comparable to experimentally measured wall pressure spectrum. This is presented in Fig. 4.22a. Here the model was tuned on the blade mode which was involved in the most dominant NSV. It can be seen that the relevant frequency peaks (Engine Order 7.53 and 8.46) are correctly predicted by the model. As discussed in (Brandstetter et al., 2021a), other peaks in the measured spectrum are related to acoustic phenomena, which are obviously not present in the model. But most importantly, peaks present in both the model and the experiment are related to convective phenomena which are not in lock-in with structural vibration. These could be clearly identified through a comparison between the individual results.

The model was also used to revisit one of the seminal papers on non-synchronous vibration and "Rotating Instabilities" by Baumgartner et al. (1995). The paper analyses a spectrum as depicted in Fig. 4.22b, showing multiple peaks with a dominant peak at EO 13.46. The authors used two adjacent peaks to determine the propagation speed of the dominant mode to 0.62 Ω_a^S. Considering the blade vibration frequencies of two modes, the authors also determined possible interaction modes, and suspected a characteristic frequency of the "rotating instabilities" as the responsible phenomenon for the excitation of the vibration modes. This led to the definition of rotating instabilities as disturbances which have a frequency in their own frame of reference.

Using exactly the same calibration values for circulation generation and modal forcing as for the low-speed-fan (section 4.2.3), the semi-analytical model was applied to the case, merely the blade number (27), vibration eigenfrequency (EO13.44) and propagation speed were adapted to the values given in the paper. With pre-imposed random disturbance, the model develops the spectrum presented in Fig. 4.22b in comparison to the measurement results from Baumgartner et al. (1995). Clearly, all peaks observed in the measurements are well represented in the model results and can be associated to wave numbers of the aerodynamic disturbances. Coherent structural interaction (NSV) between aerodynamic disturbances of wave number N_a13 with the blade vibration mode in a pattern of N_v6 causes the dominant peak. Random excitation of multiple nodal diameters leads to further peaks

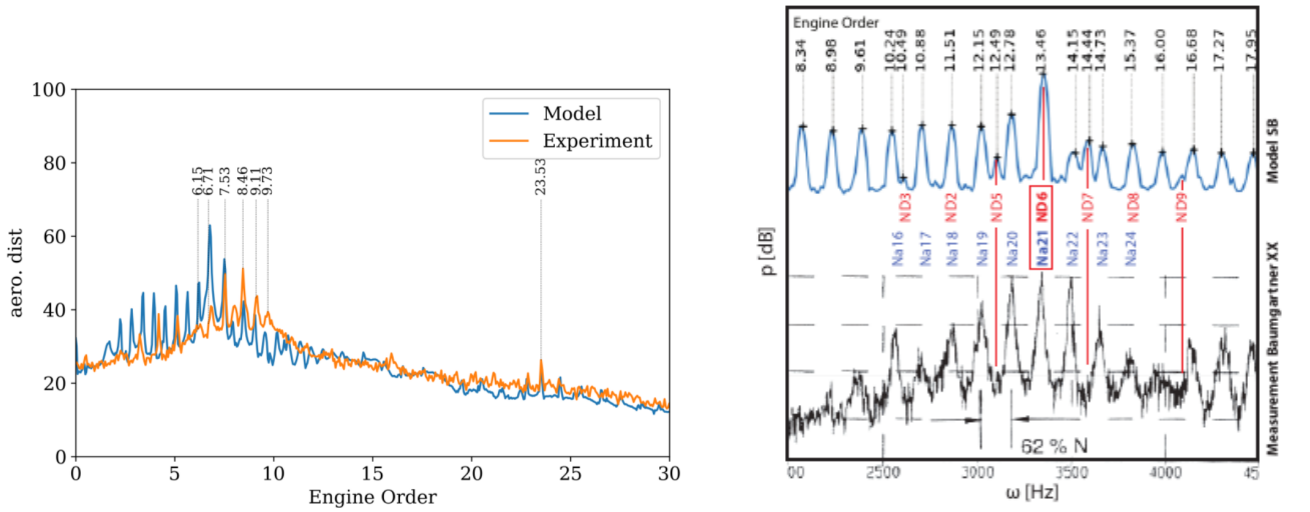

(a) Comparison of measurement and semi-analytic-model spectra for low-speed-fan, model tuned on torsional vibration mode, amplitudes normalized (Brandstetter et al., 2021a)

(b) Comparison of measured spectra from (Baumgartner et al., 1995) and Semi-analytic model (Brandstetter et al., 2021a)

Figure 4.22: Frequency spectra from aerodynamic disturbance term in semi-analytic model and experimental wall pressure measurements

which are not in resonance but visible in both, the model results as in the measurements (i.e. N_v5 and N_v7).

As the model only contains a disturbance term which propagates at a constant velocity and interacts with the blades, it is clear that a characteristic frequency of the disturbances (rotating instabilities) is not necessary to explain the phenomenon. All spectral peaks, the excitation of the critical vibration pattern and hence the emphasized peak at the coherent mode are present in the model. Moreover, the most coherent spectrum compared to the measurement was found for a propagation speed in the model set to $\Omega_a^S = 0.637\Omega_r$ deviating slightly from the peak spacing of 0.62 derived from the peak spacing and denoted in Fig. 4.22b.

This represents a great example how application of a reduced order model with physical background can help to comprehensively interpret experimental data.

4.6 Mistuning analysis

Experimental and numerical studies described in literature have shown significant effect of structural mistuning on classical flutter Srinivasan (1980); Corral and Martel (2012). The transferability to NSV is not evident. In the following section, the model will be used to analyse the influence of system asymmetry resulting from structural (frequency) or aerodynamic (geometric) mistuning. The coupled system is integrated in time and a circumferential Fourier transform on the blade displacement is used to determine the displacement history in each nodal diameter. An exponential fit is applied to derive the damping coefficient ζ for every N_v. This time-marching implementation was validated against the eigenvalue analysis presented for the tuned case. The full results were presented in (Stapelfeldt and Brandstetter, 2021).

4.6.1 Aerodynamic mistuning implementation

To introduce aerodynamic mistuning, we assume that there are different types of blades with different flow fields but we keep the force coefficients constant. This is a reasonable assumption since they were found to vary little between operating points and have little influence on stability Brandstetter and Stapelfeldt (2021). In the model described above this is represented by a modified attenuation coefficient $r_{a,n}$, which depends on the blade as illustrated in Fig. 4.23. Assuming that a disturbance travels through different passages with constant speed, the scaling coefficient for the aerodynamic

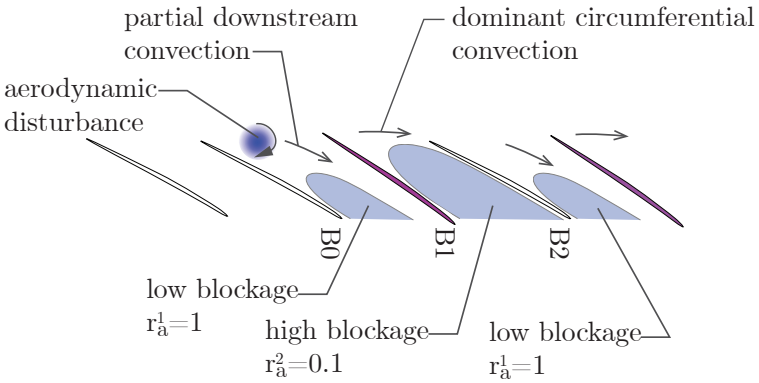

Figure 4.23: Schematic of disturbance propagation in a blade row with aerodynamic mistuning, for example alternating blade stagger angle, blade sweep or tip clearance causing inhomogeneous tip blockage.

force contribution from Blade n becomes:

$$\begin{aligned}\hat{C}_{a,n} &= \hat{C}_a^* \Pi^n e^{-r_{a,n}} \\ &= \hat{C}_a^* e^{\sum^n -r_{a,n}}\end{aligned} \tag{4.25}$$

which recovers Eq. 4.25 for a constant r_a. For an alternating mistuning pattern with attenuation coefficients r_a^1 and r_a^2:

$$\hat{C}_{a,n} = \hat{C}_a^* e^{-N_1 r_a^1 - N_2 r_a^2} \tag{4.26}$$

where N_1 and N_2 are the number of blades between preceding Blade n and Blade 0 with r_a^1 and r_a^2 respectively. For an arbitrary pattern, the expression for aerodynamic forcing then becomes:

$$F_a(t) = \sum_{n=0}^{N-1} \tilde{C}_a^* \hat{\alpha} e^{i\omega_v t} e^{-\sum^n r_{a,n}} e^{-i(n\sigma_v + n\sigma_a)} \tag{4.27}$$

Substituting this expression for the force resulting from the accumulated aerodynamic disturbance and the force resulting from vibration of the blade itself into the equation of motion 4.3 results in a linear system, the stability of which can be analysed using eigenvalue analysis.

Various patterns with blade individual attenuation coefficients varying between r_a^1 and r_a^2 are modelled as follows:

$$r_{a,n} = (A_n + 0.5) r_a^1 + (0.5 - A_n) r_a^2 \tag{4.28}$$

where A_n is the mistuning coefficient applied to Blade n. This defines the patterns (circumferential arrangement) which are shown in Fig. 4.24.

4.6.2 Structural mistuning implementation

Structural mistuning is incorporated into the model by considering a varying blade stiffness in the coupled model. According to the patterns of A_n from Fig. 4.24, the stiffness matrix K in eq. 4.3 is assembled as follows:

$$K_{n,n} = (\omega_v (1 + A_{smt} A_n))^2 \tag{4.29}$$

with ω_v being the reference eigenfrequency of the blade and A_{smt} representing the structural mistuning amplitude. The coupled system is integrated over time and the vibration pattern Fourier-transformed to derive the temporal evolution of each nodal diameter N_v. An exponential fit is applied to derive the damping coefficient ζ for every N_v. The time-marching implementation was validated against the eigenvalue analysis presented for the tuned case.

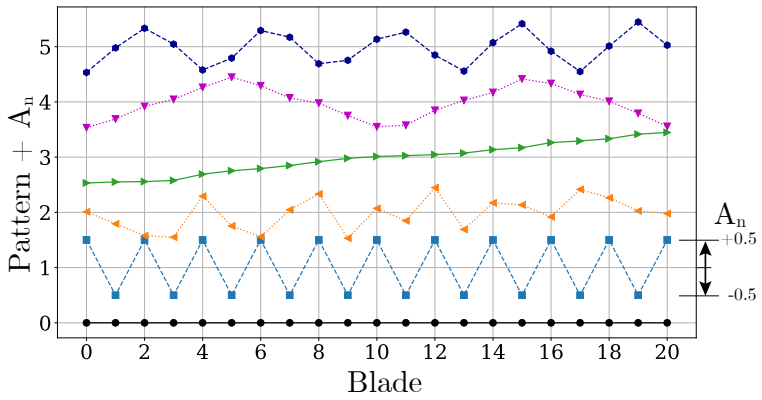

Figure 4.24: Frequency mistuning patterns, Mistuning coefficient A_n, Pattern 0 tuned, Pattern 1 alternating, Pattern 2 random, pattern 3 to 5 rearrangements of Pattern 2

To demonstrate the effectiveness of structural mistuning against NSV, a range of frequency mistuning patterns is tested using the model described above. The patterns are shown in Fig. 4.24. They were chosen to test a range of arrangements: alternating (P1), random (P2), linear (P3) and sinusoidal variations of two different wave lengths (P4 and P5). Patterns P2-P5 have the same blade-individual frequency, only their circumferential arrangement differs. In the case of bladed disks this allows the assessment of intentional arrangement of blades with random manufacturing tolerance.

Each pattern is tested with different mistuning amplitudes, defined as the fractional frequency deviation between the maximum and nominal blade frequency:

$$A_{smt} = \frac{\omega^R_{v,max} - \omega^R_{v,min}}{\omega^R_{v,nominal}} \tag{4.30}$$

Effect of structural mistuning on NSV

The influence of structural mistuning is studied at the experimentally and numerically tested unstable operating point, OP2. A damping curve for 1% mistuning amplitude in Pattern 2 is compared to the tuned case in Fig. 4.25 as an example. Without mistuning, only nodal diameter $N_v = 8$ is unstable, which agrees with the experiment (Brandstetter et al., 2018) where NSV was observed for $N_v = 8$. When mistuning is introduced, $N_v = 8$ remains the most critical mode but aero-damping has increased from approximately -2.5% to -1.75%.

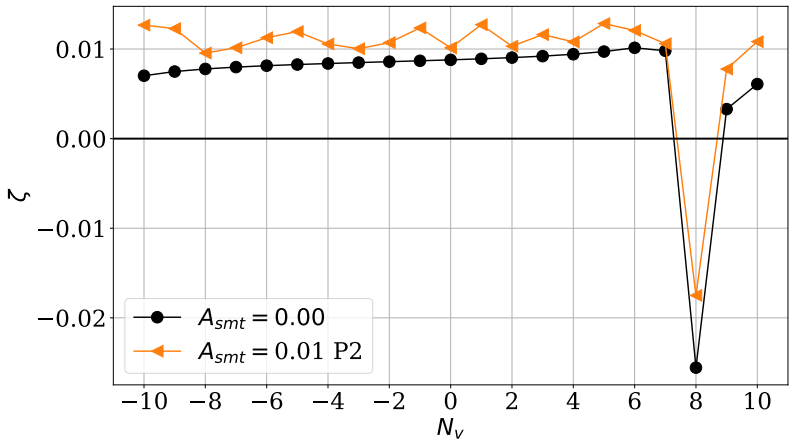

Figure 4.25: Aerodynamic damping versus nodal diameter for different frequency mistuning patterns with 1% mistuning amplitude

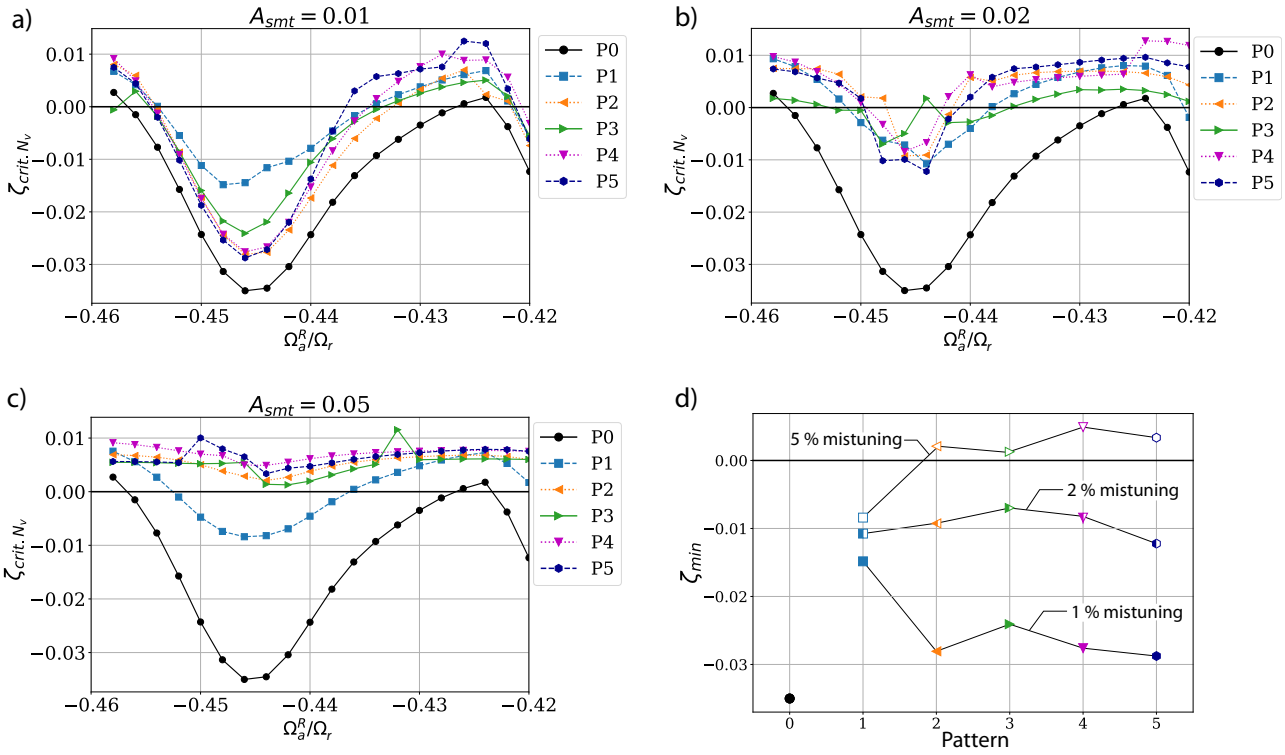

Figure 4.26: Variation of minimum aerodynamic damping with propagation speed for different structural mistuning patterns, a) 1% mistuning, b) 2% mistuning, c) 5% mistuning, d) Minimum aero-damping for different mistuning patterns and amplitudes. Full symbols 1%, half symbols 2%, empty symbols 5% structural mistuning amplitude

Since the design objective is to stabilise the compressor across the whole operating range, the model parameters are now varied to represent changes in operating condition and the minimum aerodynamic damping for each condition is extracted. Since only operating points with a low decay rate are unstable, the following analysis will concentrate on a variation of propagation speed while other model parameters are kept constant at values representative of the unstable operating point (OP2).

Figure 4.26 shows the minimum aerodynamic damping as a function of convective speed for different mistuning amplitudes. For the tuned case (P0), aero-damping is smallest at the resonance condition $\Omega_a^R/\Omega_r \approx -0.447$, where the free phase-speed of the aerodynamic disturbances matches that of the structural vibration. As shown in (Stapelfeldt and Brandstetter, 2020), the system can develop a single aeroelastic frequency through adaptation of the nodal diameter and, to a smaller extent, propagation speed. Therefore, lock-in can also occur when the phase-speed of the free aerodynamic disturbance deviates from that of the vibration but the magnitude of aerodamping changes. This can be seen in Fig. 4.26, where for the tuned case lock-in occurs over the whole range of free propagation speeds. Between $\Omega_a^R/\Omega_r = -0.460$ and -0.425 the aerodynamic wave number is constant at N_a =13 but the magnitude of aero-damping varies with propagation speed. At a higher free propagation speed the systems locks in to wave number N_a=14 (compare Fig. 4.21). All mistuning patterns and amplitudes improve stability compared to the tuned case. However, the patterns behave differently as mistuning amplitude is increased.

For 1% mistuning, shown in Fig. 4.26a, aero-damping increases but the shape of the curve does not change significantly. The alternating pattern (P1) is the most effective and more than halves the negative aero-damping at resonance condition. Off-resonance between $-0.435 < \Omega_a^R/\Omega_r < -0.420$, all patterns stabilise the rotor.

Figure 4.26b shows that doubling the mistuning amplitude has a large effect. The stable range is extended significantly but a small unstable range remains near resonance for all mistuning patterns. There is no longer a distinct advantage from the alternating pattern compared to the others. Increasing the mistuning amplitude to 5% (Fig. 4.26c) completely stabilises the rotor for four patterns. In this

case, the alternating pattern is the only one that remains unstable near resonance.

A shift in the location of minimum aero-damping can also be seen for some patterns in Fig. 4.26 (b) and (c). This is caused by the frequency of the aeroelastic system shifting from its tuned frequency when the mistuning amplitude is sufficiently high.

For a better comparison of patterns and amplitudes, the minimum aero-damping over the range of convection speeds is plotted in Fig. 4.26d. It shows that the effect of the alternating pattern (P1) does not vary much with amplitude, whereas varying the mistuning amplitude for the other patterns results in large changes (>100%) in aero-damping. As mentioned above, Patterns P2-P5 are all stable with 5% frequency mistuning.

4.6.3 Effect of aerodynamic (geometric) mistuning

Aerodynamic mistuning is modelled by changing the decay rate as described above. In the first experiment, the decay rate is doubled over part of the circumference, from $r_a^1 = 0.075$ on half of the blades to $r_a^2 = 0.15$ on the other half, and various patterns are tested. Pattern P0 represents the tuned case with an average decay rate, $\bar{r}_a$=0.1125 (see Eq. 4.28). As seen in Fig. 4.27a, attenuating the disturbance more over half of the circumference reduces the aero damping magnitude of the critical (most unstable) nodal diameter by approximately 50% compared to the tuned reference case. The influence of the pattern is marginal and the aero-damping is similar to that of the tuned case with an increased decay rate (P0). Fig. 4.27b shows the same curves but the decay rate over half of the blades has been increased. From a decay rate of $r_a^2 = 0.45$ the system becomes stable for Pattern P2. The other patterns remain marginally unstable at this decay rate but at $r_a^2 = 1.0$, corresponding to OP1, all patterns are stable.

4.6.4 Combined aero-structural mistuning

To assess the combined benefits of aerodynamic and structural mistuning, we choose the random structural pattern P2, which behaved similarly to Patterns P3-P5 and was completely stable with 5% mistuning amplitude, and vary aerodynamic mistuning. As before, the other model parameters are fixed at those for the unstable operating point, OP2.

The similar behaviour of the different aerodynamic mistuning patterns suggests that stability is not driven by local aerodynamic effects but by circumferentially averaged conditions. We therefore define an average decay rate for patterns with two blade sets to define the aero-mistuning amplitude:

$$\bar{r}_a = \frac{r_a^1 + r_a^2}{2} \tag{4.31}$$

To allow a more intuitive interpretation of this decay coefficient, we express it in terms of half-life of the aerodynamic disturbance, given by $t_h = log2/\bar{r}_a$.

Figure 4.28 plots the minimum aero-damping across the range $-0.46 < \Omega_a^R/\Omega_r < -0.42$ as the average decay rate is varied for three levels of structural mistuning. Without structural mistuning,

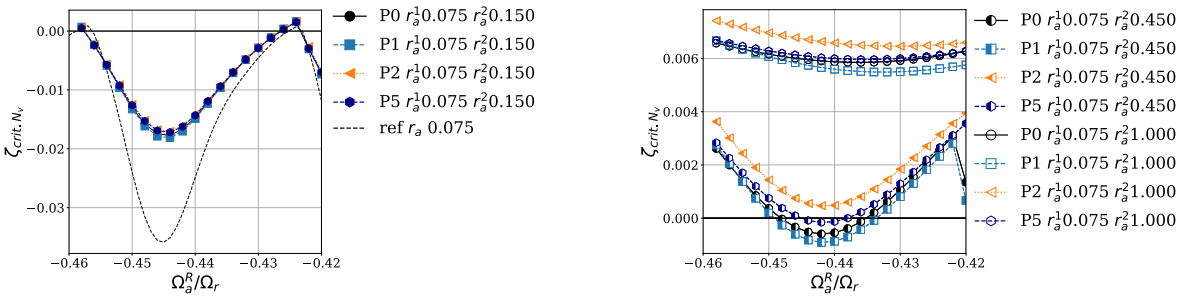

(a) $r_a^1 = 0.075$ and $r_a^2 = 0.15$. Tuned case $r_a = 0.075$

(b) $r_a^1 = 0.075$ and $r_a^2 = 0.45$ and $r_a^2 = 1.0$

Figure 4.27: Variation of minimum aerodynamic damping with propagation speed for different aerodynamic mistuning patterns

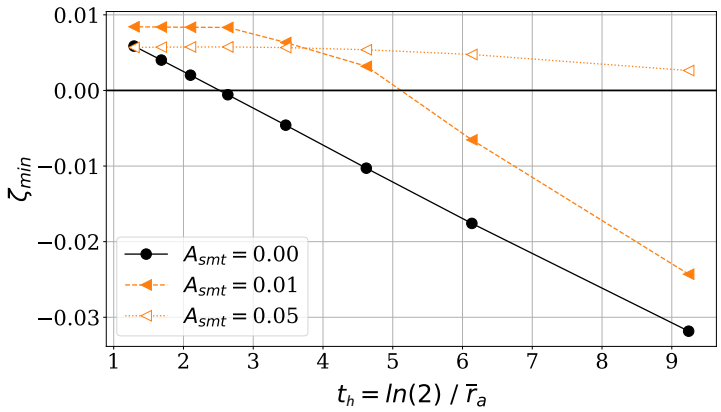

Figure 4.28: Variation of minimum aerodynamic damping with average decay coefficient for three levels of structural mistuning in Pattern 2, t_h represents half life decay time in blade passages

aerodynamic damping depends linearly on the half-life of the aerodynamic disturbance and the system becomes stable for an average $\bar{r_a} = 0.3$, or half-life $t_h = 2.3$ revolutions. When the decay of the aerodynamic disturbance is lower, the linear model predicts instability. Structural mistuning lowers the critical decay rate, or raises the critical half-life as seen by the orange curves in Fig. 4.28. For 1% structural mistuning, the system becomes stable at $\bar{r_a} = 0.14$ ($t_h = 5$), while for higher levels of structural mistuning, the aerodynamic effects diminish and the rotor is stable.

4.6.5 Conclusions on mistuning

A number of general results emerged from the presented mistuning study.

Frequency mistuning was found to be effective at increasing aero-damping but only at relatively large mistuning amplitudes. The variations necessary to stabilise the rotor under investigation were approximately 5%. This is well outside the range of manufacturing tolerances and the required amplitudes may cause problems of forced response. The pattern was found to play a role, with particularly the alternating pattern performing comparatively badly at large mistuning amplitudes. Furthermore, excessive structural mistuning is known to be detrimental for forced response behaviour.

Aerodynamic mistuning was also found to successfully suppress convective NSV. The most influential factor is the average decay rate of the aerodynamic disturbance. Its circumferential distribution played a negligible role. In a compressor, the change in decay rate is achieved by locally reducing the tip blockage to reduce the component of disturbance being convected in the circumferential direction. The change in decay rate necessary to stabilise the blade (from $r_a = 0.075$ to 0.30 without structural mistuning) appears large but it is helpful to put it into context by considering the changes in decay rate across a compressor operating range. Previous studies Stapelfeldt and Brandstetter (2020) measured a decay rate close to 1 at a stable operating point close to rotor peak pressure rise, compared to 0.075 at NSV conditions. This represents a more than ten-fold increase in decay rate between two close operating points. These results hint at the effectiveness of **casing treatments** in suppressing NSV as reported in Brandstetter (2015); Brandstetter et al. (2016b). Casing treatments are known to reduce disturbances occurring in the leading edge area close to the casing. For the compressor under investigation, the application of 18 flow recirculating nozzles significantly shifted the stability limit altering the average compressor performance. Reduction of the number of nozzles reduced the stabilizing effect in proportion. The results presented here indicate that such a feature to attenuate circumferential propagation of disturbances does not necessarily be homogeneous around the circumference, providing enormous design potential. These results from (Stapelfeldt and Brandstetter, 2021) represent the first systematic analysis of mistuning for NSV. The model can be calibrated from reduced-domain CFD simulations and is therefore a fast and cost-effective means of assessing the risk of NSV and mitigation measures, such as deliberate arrangement of blades with intentional and unintentional manufacturing differences, in engine design.

Chapter 5

Acoustic Resonance

5.1 Planar acoustic modes and modal stall inception

As described in section 2.2, the inception of rotating stall, providing an inevitable breakdown of stable operation, is typically preceded by aerodynamic precursors of different characteristic length-scales and propagation speeds (Camp, 1999). Short-length scale disturbances are known as 'spikes' whereas large length scale disturbances have been called 'modal' waves.

A study presented by Tryfonidis et al. (1995) on multiple low- and high-speed compressors showed that for low corrected speeds long length-scale, incompressible, circumferentially propagating modes are dominant whereas a compressible mode appears at transonic conditions. For the incompressible modes, which can be predicted with the Moore-Greitzer model (Moore, 1984) phase velocity typically amounts to a fraction of the rotor speed whereas the compressible mode is associated to a disturbance that remains fixed to the rotor. Comparable results have been obtained by Bright et al. (1999), who detected strong pre-stall disturbances travelling with the rotor speed already several thousand revolutions before stall.

The susceptibility of a specific machine to either modal or spike-type stall inception depends on the slope of the total-to-static compressor characteristic near stability limit, as presented by Camp and Day (1998). While spike-type stall inception has been associated with stall precursors such as the radial vortices described in Section 4.2.1, there is still relatively little understanding regarding the physical source of modal waves and their sensitivity towards engine and facility parameters.

5.1.1 Modal stall inception in composite fan

On the test facility at ECL described in section 4.2.3 we conducted a comprehensive study on this type of instability onset using a composite fan which is derived from the CFM International LEAP engine, reported in Brandstetter et al. (2019c). Repeated investigations of the fan stage were performed near the stability limit at different subsonic and transonic speedlines. For these, the stage was stabilized for several minutes at a highly loaded operating point whereupon the exit throttle was sequentially closed at a very low and constant rate until surge or rotating stall was acoustically detected, leading to the opening of emergency valves.

Results of synchronously recorded unsteady aerodynamic and structural measurement systems for these operating speeds are presented in the following. Figure 5.1 shows time-histories of unsteady wall pressure upstream of the rotor in the periods before and during rotating stall or surge at t=0, for operating conditions between 80% (N80) and 105% of design speed. The behavior of the machine after initiation of a rotating stall cell varies depending on the rotation speed. The period of rotating stall is followed by a low frequency oscillation of a characteristic (mild) surge shape for the speeds 90%, 100% and 105%. The frequency of surge oscillation approximates 10.5Hz for all measured speedlines. At 80%, 85% and 95% speed the stage there is no evidence for surge. For all speedlines, rotating stall is preceded by low frequency modal oscillations. Between 90% and 105% these are clearly visible as an envelope of the unsteady pressure signal (Fig. 5.1). The initiation of a rotating stall cell always occurs at a static pressure peak at t=0, corresponding to a minimum of axial velocity.

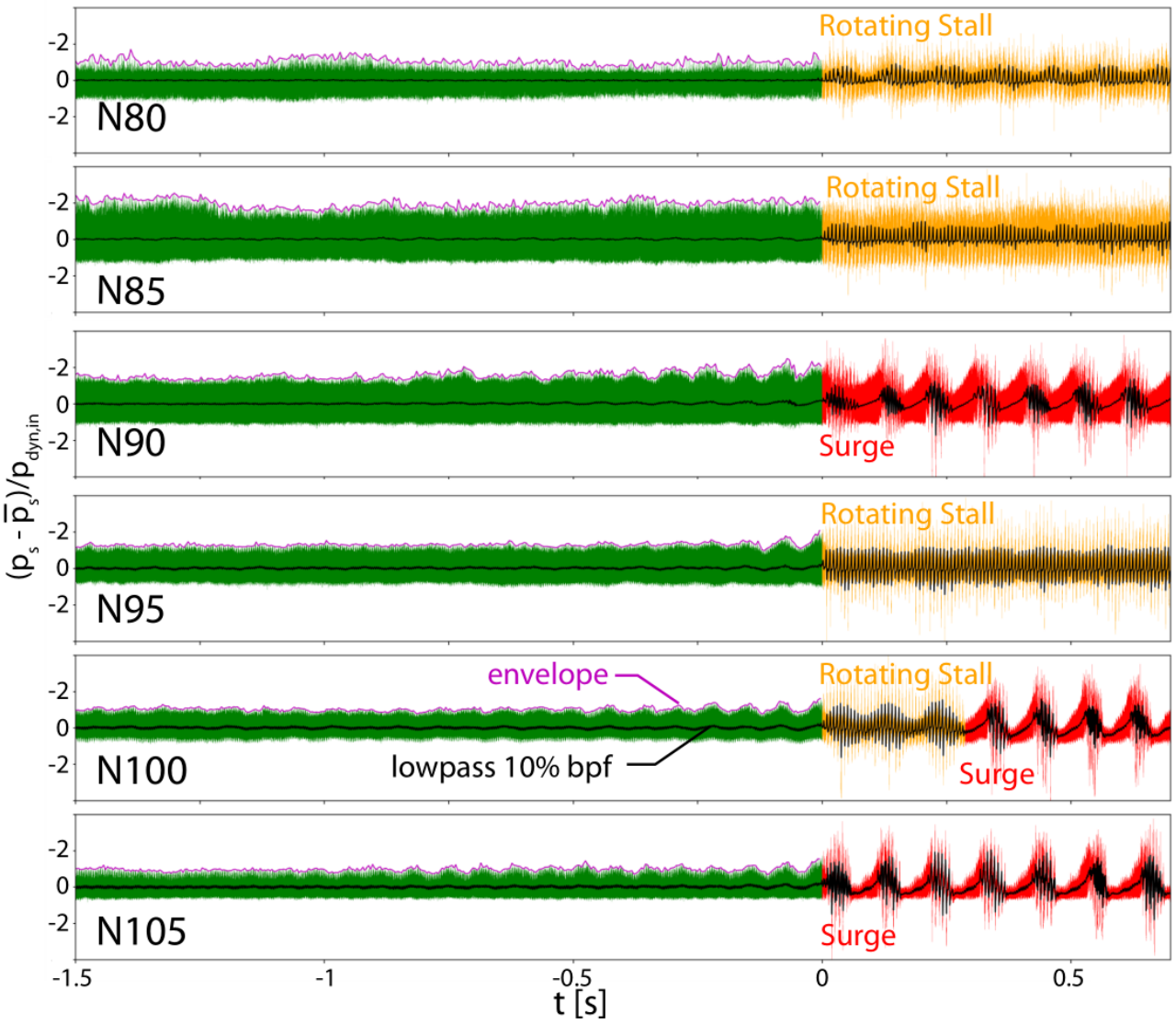

Figure 5.1: Time History of unsteady wall pressure upstream of the rotor for all measured speedlines, stall onset at t=0

The low frequency spectra of these wall pressure signals are shown in Fig. 5.2a, left column). A common behavior for the high speedlines 90% to 100% is apparent. Frequency peaks around 9Hz and 14 Hz as well as their harmonics are observed depending on the speedline.

During the last 2-4 seconds before the first rotating stall cell the amplitude of an oscillation at approximately 14Hz rises continuously from below 1% to 5% of the average dynamic pressure at the intake as can be seen in the modal amplitude graphs (Fig. 5.2a, right column). At N105% the oscillation already appears multiple seconds before stall with varying amplitude of up to 10% of the dynamic pressure at the intake.

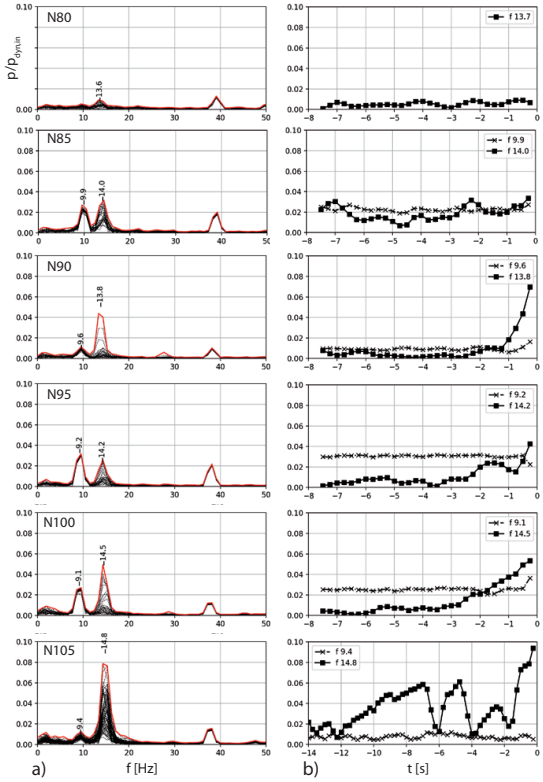

(a) Pre-stall spectrum and temporal evolution of selected modal amplitudes, sliding fft-window 0.8s, Hanning, 50% overlap

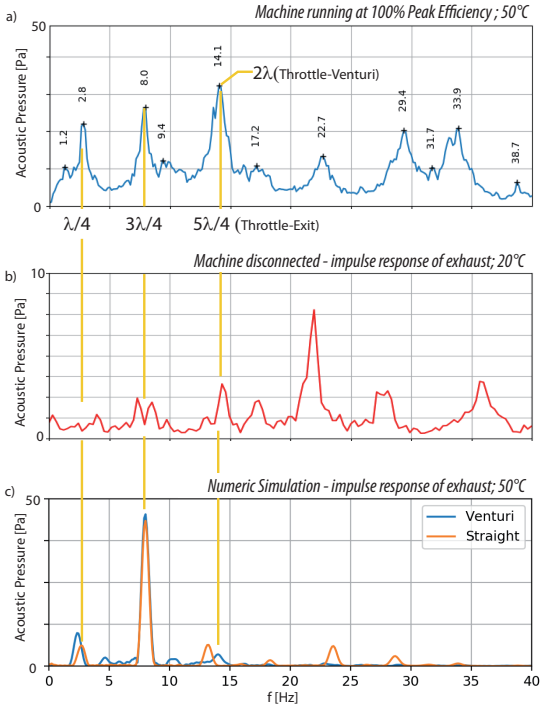

(b) Acoustic spectrum of exhaust, experimental and numerical results

Figure 5.2: Spectral signal analysis

5.1.2 Acoustic properties of exhaust system

To analyse the source of the unsteadiness, acoustic properties of the machines exhaust system, both experimentally and numerically have been characterised using a combination of experiments and numerics presented in Fig. 5.2b: a) acoustic measurements in the exhaust with the machine running at N100%; b) measurements of the response of the isolated exhaust and throttle system to an acoustic impulse generated by small explosive charges; c) numerical simulations of the exhaust system.

The frequency spectrum of a microphone downstream of the machine throttle at a stable operating point (100% speed) is shown in Fig. 5.2b, top graph. The first fundamental acoustic modes of the exhaust pipe are clearly visible at 2.8 Hz and 8 Hz, which correspond to a $\lambda/4$ and $3\lambda/4$ standing wave with an open termination at the exit and an approximately closed termination at the throttle. Higher modes attributed to the open exit termination of the system can also be determined from the spectrum. To confirm that the observed spectra are independent from the machine core, repeated impulse responses of the exhaust system using an explosive noise source have been recorded, showing the spectrum presented in Fig. 5.2b, middle graph. All modes observed with the machine running at 100% can be found in the isolated spectrum, particularly the 14Hz Mode, even though the frequency resolution is much lower because only segments of 3 seconds after each impulse could be used for the analysis.

The numerical results of the exhaust system confirm the analytical interpretation of the observed modes in the spectra depicted in Fig. 5.2b, bottom graph. The fundamental modes at $\lambda/4$ and $3\lambda/4$ observed in the measurements are well represented. The comparison of a simulation with and without Venturi nozzle shows that the $5\lambda/4$ resonance of the straight section appears around 13Hz and is shifted towards 14Hz with installed nozzle. The modeshape indicates a 2λ oscillation between throttle and Venturi-Nozzle and explains the broadness of the 14Hz peak. All fundamental mode shapes derived from the simulations are presented in Fig. 5.3a.

The comparison of different instrumentations in Fig. 5.3b shows that the relative amplitude of the

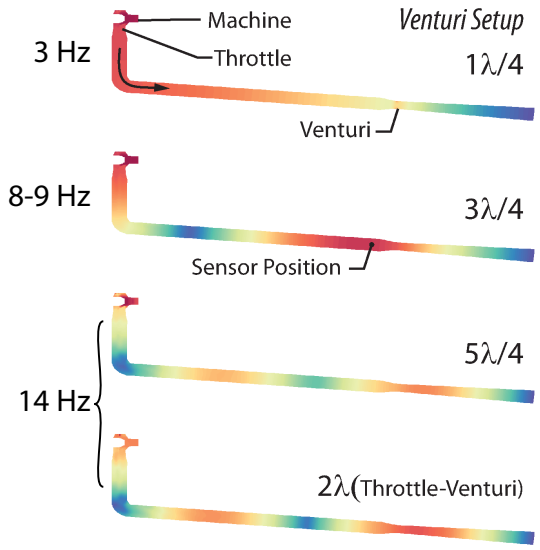

(a) Shape of low frequency acoustic modes (modal pressure amplitude); Numerical Results at design Mass flow

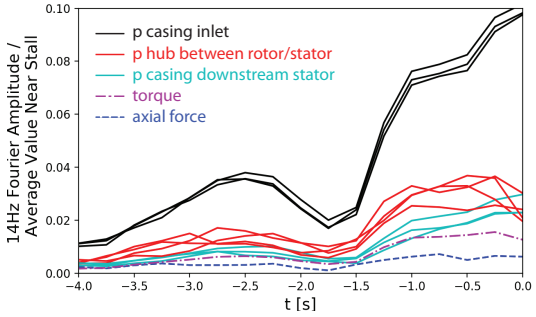

(b) 14HZ modal amplitude in different instrumentations, N105%

Figure 5.3: Analysis of 14Hz Mode

14Hz oscillation is dominant for the casing wall pressure, both upstream and downstream of the stage, representing a planar acoustic wave.

This analysis clearly demonstrates that the acoustic characteristics of the exhaust system determine the frequencies observed at near stall conditions because all peaks can be clearly attributed to fundamental acoustic modes. In order to investigate how the respective modes are excited and resonate with the fan stage a detailed analysis of the unsteady instrumentation of the fan stage was conducted.

5.1.3 Interaction between acoustic modes and fan aerodynamics

To characterize the aerodynamic disturbance developing in the fan, the position of each leading edge shockwave relative to the rotor blade has been extracted from wall-pressure signals. Therefore, the pressure signal during one revolution has been divided into equal parts for each blade passing. The arrival time of each shock could then be robustly detected by calculating the cross-correlation of individual blade passing signals with a median signal at steady near stall conditions. Results for the 105% speedline are presented in Fig. 5.4, with each line representing the shock arrival time for the respective blade. The dashed lines mark uniform spacing.

After a period of continuous shock detachment for all rotor blades between revolutions -500 and -390 a distinct low-frequency oscillation (14Hz) establishes around 390 revolutions (≈1.5s) before stall. The graph demonstrates that the average shock position and its variation is not homogeneously distributed over the rotor. Instead it is found that one section of the rotor is always working with a further recessed shock whose position is closer to the rotor blade (comp. sketch in Fig. 5.4). The effect is most severe for the blade numbers 9 to 16 which also suffer of the strongest fluctuations. It is also visible that Blade 15 already works with a further recessed shock before the onset of modal activity.

The comparison of all shown revolutions demonstrates the development of an asymmetrical load distribution that remains fixed with the rotor. In contrast to a spike type leading edge separation this disturbance is not propagating towards the subsequent blade before the onset of rotating stall but diminishes again periodically. The average, minimum and maximum shock position during the pre-stall phase is given in Fig. 5.5a. The strongest fluctuations occur in the rotor sector containing the blades with recessed shock position (Blades 9 to 16). When comparing the measurements at different speedlines, it is found that the same blades are most susceptible to fluctuations of the shock-position and associated blade loading. The most recessed position reaches values steadily observed at

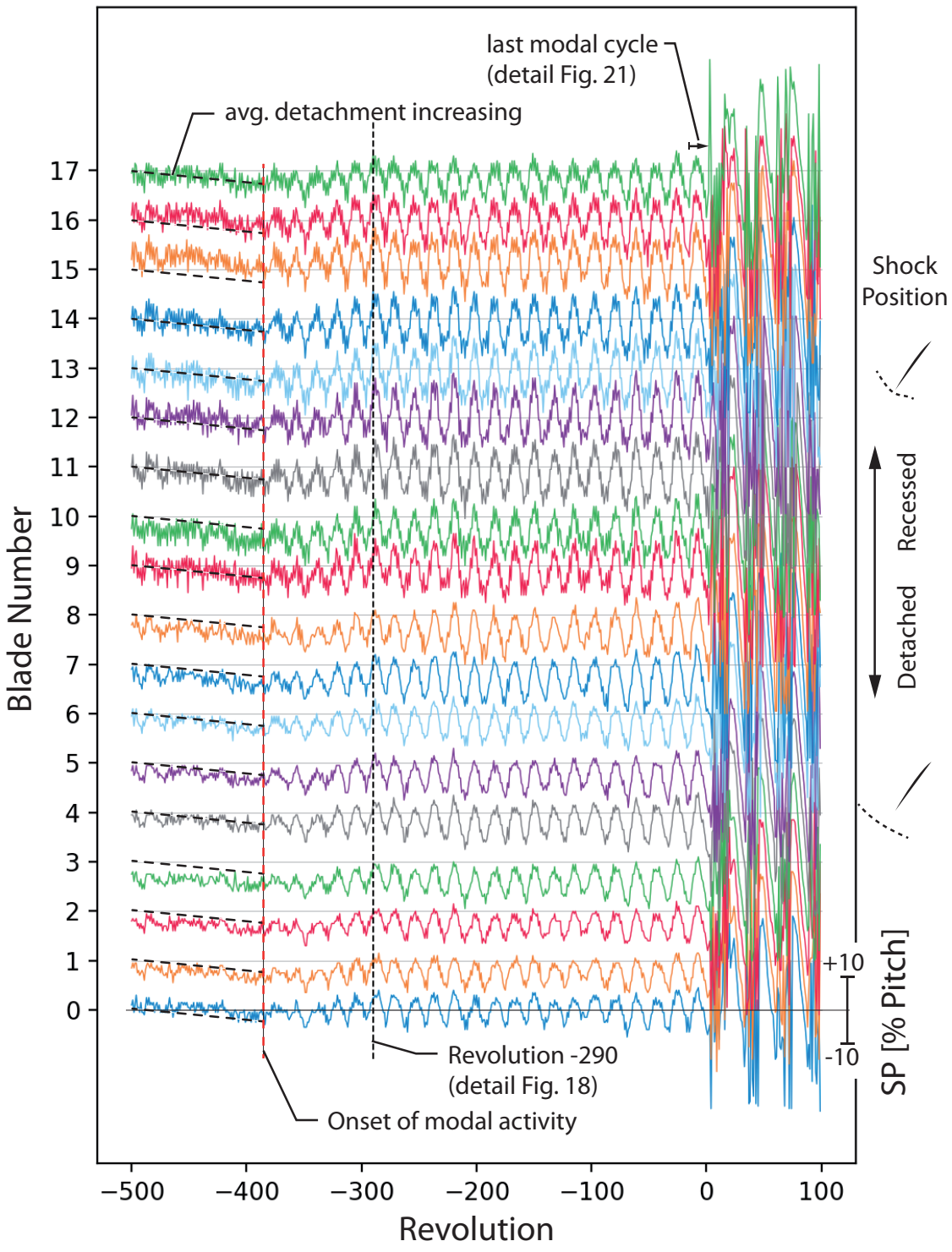

Figure 5.4: Variation of shock position for N105%; Detected with unsteady pressure sensor upstream of rotor leading edge

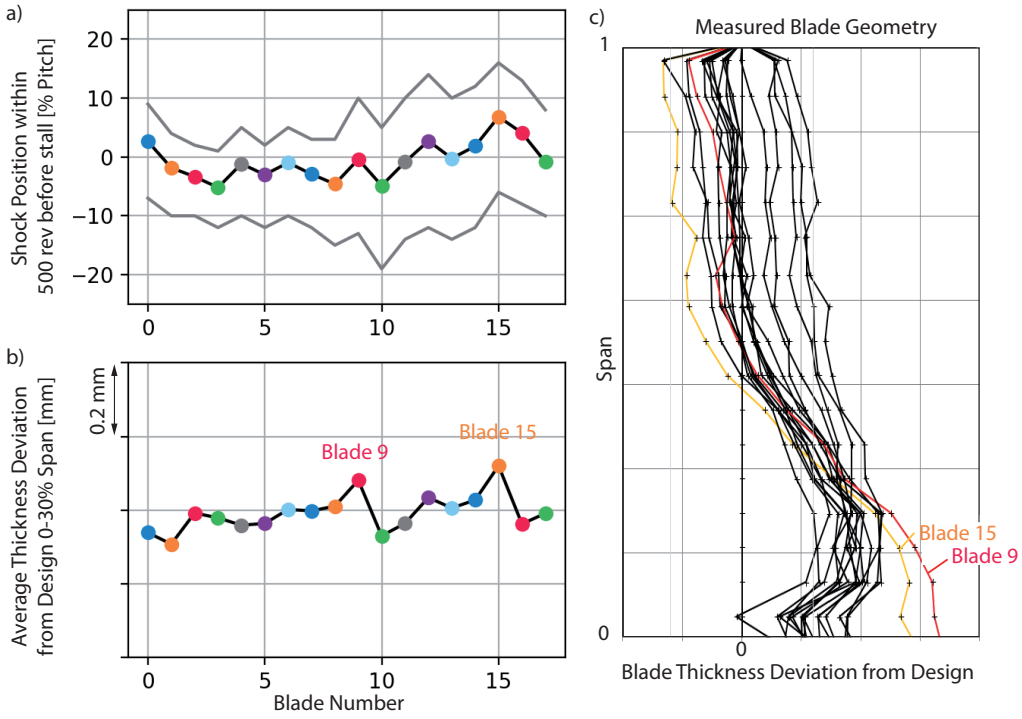

Figure 5.5: Comparison of shock position and blade geometry parameter

peak-efficiency operation, a condition that should be more stable from an aerodynamic point of view. Nevertheless the results clearly show that the blades with recessed shock are aerodynamically more unstable.

5.1.4 Role of geometric asymmetry in fan aerodynamic response

Since no signs of propagating flow separations are observed, the reason for the instability of this configuration was assumed to rely on a non-linear fluid-mechanical interaction that is similar to the one presented by Wilson et al. (2006), who have shown the influence of static stagger variability on the dynamic pressure untwist behavior of fan assemblies. At transonic conditions the untwist is essentially influenced by the position of the shock. If a blade works at started conditions with a swallowed shock and a supersonic zone around the leading edge, the untwist is significantly lower than for a detached shock configuration with subsonic flow at the pressure side. The divergence of the passages adjacent to the mis-staggered blade is asymmetric, influencing the lift distribution, particularly on the downstream blades (Lu et al., 2019b). Wilson et al. (2006) reported how a single mis-staggered blade provoked unstable conditions of the whole assembly with alternating started and unstarted passage flow.

The actual stagger angle at the blade tip depends on the static geometry and the resistance of the individual blades towards pressure untwist, whereupon possible influential geometrical parameters of the measured blades have been analysed.

A clear correspondence has been found between the shock position and the measured blade thickness of the lower 30% span, depicted in Fig. 5.5b. Here, the blades with maximum foot thickness work with a less detached shock that fluctuates more than ±10% of the rotor pitch. The two blades 9 and 15 who show deviations from the design value shown in Fig. 5.5c are clearly prominent in the aerodynamic asymmetry over the whole pre-stall process. Further geometrical parameters are similarly correlated but additional measurements that allow the identification of unsteady untwist and the actual position of the shock on the blade suction side are necessary to derive the sensitivity of respective values. Nevertheless, the results clearly indicate that the aerodynamic mistuning is sufficient to provoke a significant unstable asymmetry in the loading distribution of the rotor.

The amplitude of asymmetry is modulated with a clearly dominant frequency of the 14Hz mode for all speedlines as depicted in the spectrum in Fig. 5.6. Further peaks observed in the pressure spectra in Fig. 5.2 diminish, particularly the 9 Hz Mode.

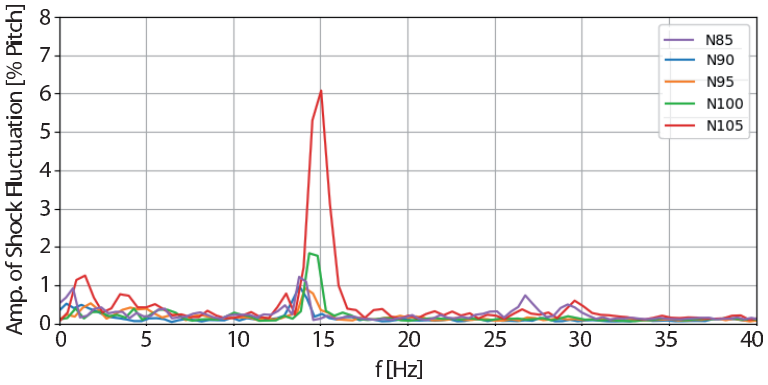

Figure 5.6: Spectrum of pre stall shock fluctuation for all transonic speedlines; average value for all blades during 2 seconds ($\approx$ 500 rev.) before rotating stall

5.1.5 Conclusions on Fan interaction with planar acoustic modes

Comparing the analysis of the asymmetric fan aerodynamics with the acoustic analysis of the exhaust, the pre-stall mechanism can be summarized as follows with an illustration in Fig. 5.7:

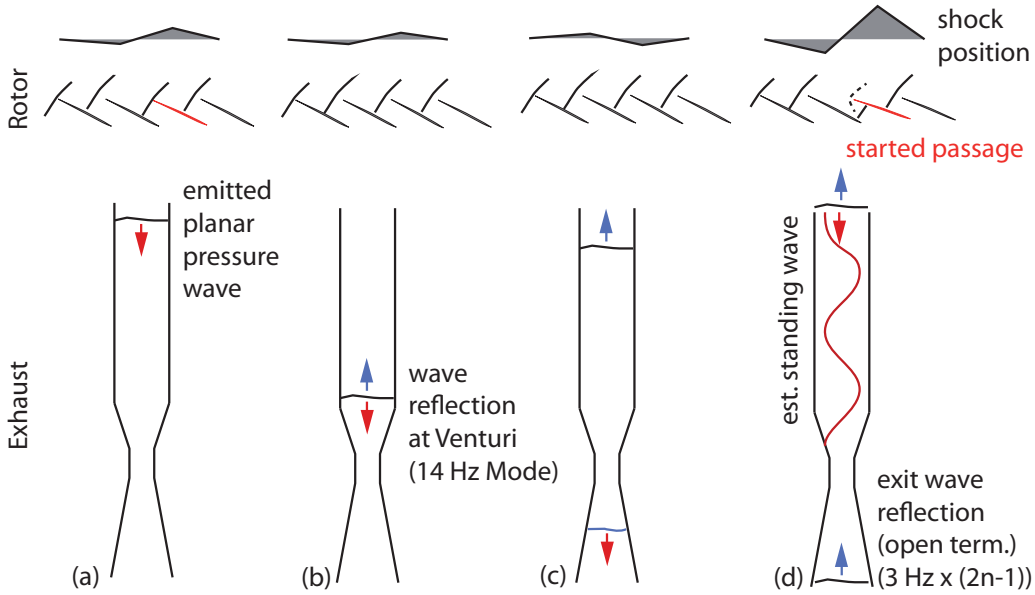

Figure 5.7: Feedback loop between rotor asymmetry and exhaust

1. At highly loaded conditions, small geometrical inhomogeneities of the rotor blades cause asymmetrical loading distribution.

2. The unsteady untwist of the rotor blades becomes eventually unstable for individual blades, in our case for those operating at unloaded conditions.

3. The asymmetry leads to a reduction of the average stage pressure ratio and a subsequent drop of the stage exit pressure that is emitted to the exhaust and develops to a planar wave. The circumferential asymmetry is reduced by the long tubing system.

4. The geometry of the exhaust system, specifically its acoustic property, causes a reflection of this pressure wave and determines a characteristic timescale (b).

5. With arrival of the reflected pressure wave in the fan stage remaining aerodynamic inhomogeneities in the rotor are amplified, leading to subsequent emissions of pressure waves to the exhaust (c)$\rightarrow$(d). At transonic conditions singular passages temporarily develop started flow

conditions with a supersonic zone at the tip of the pressure side (comp. Wilson et al. (2006) and Lu et al. (2019a)).

6. A closed feedback loop between the amplitude of aerodynamic asymmetry in the rotor and a standing pressure wave in the exhaust system establishes. The dominant frequency is according to the mode with highest eigenfrequency of the exhaust that is efficiently reflecting the incoming pressure disturbance. Obviously the amplification and reduction of aerodynamic asymmetry in the rotor requires a specific time, since the exhaust system might also resonate with higher order modes (comp. Fig. 5.2) but always locks on the 14Hz mode.

7. In the observed case the respective mode is associated to the section change at the Venturi-tube and a $5\lambda/4$ open exhaust termination resulting in a characteristic frequency of $\approx$14Hz (at 20°C).

8. The first two fundamental modes of the exhaust (3Hz and 9Hz) are also observed because of random excitation but are not in direct resonance with the rotor asymmetry.

9. Only planar waves are contributing to this process since the system geometry cuts off all modes with higher wave-numbers at the observed frequencies.

10. Immediately before rotating stall, a weak spike-type signature is observed within the last 2-5 revolutions to initiate the single stall cell.

11. This characteristic behavior has been observed at all transonic speeds from 90% to 105%.

The interpretation and evidence in the previous sections clearly demonstrate that an aerodynamic instability in a rotor stage can resonate witch planar acoustic modes in the exhaust system. It furthermore shows that this can cause an aeromechanical response of the rotor blades which is non-linear and asymmetric and governed by geometrical variations between the rotor blades.
While the frequencies measured in this study are specific to the test facility, the existence of this acoustic, aerodynamic and aeromechanical interaction phenomenon bears implications for engineering. Planar acoustic modes can develop in the bypass duct and combustion chambers of engines. If one of the associated frequencies matches the aerodynamic response time of the rotor, resulting fluctuations can cause an unsteady untwist behavior adversely affecting the aerodynamic or aeromechanical stability boundaries.
These findings are particularly interesting, as blade-to-blade variations (i.e. mistuning) are usually considered beneficial for aeromechanical stability (i.a. Srinivasan (1980); Castanier and Pierre (2002); Kielb et al. (2007); Corral and Martel (2012)). Through reduction of system symmetry the establishment of propagating modes leading to fan-flutter or NSV can intentionally be attenuated.

The asymmetric untwist behavior, which was first studied by Wilson et al. (2006), and its amplification by acoustic modes described in the current work, presents a case where mistuning can cause or exacerbate aeromechanical oscillations, specifically for low-speed-fans with a particularly flat characteristic.
Furthermore, the findings clearly show that the acoustic characteristics of the system must be considered to ensure transferability between computational predictions, rig tests and engine conditions. The authors generally suggest a thorough analysis of the acoustic properties of test-facilities used to investigate instability mechanisms in turbomachinery. Particularly concerning the low-frequent planar modes, reproducible spectra could be measured using explosive noise sources.

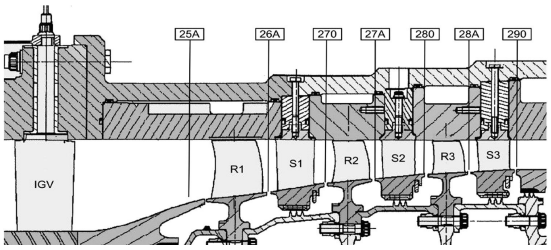

(a) Meridian View of the 3.5 Stage Compressor Create

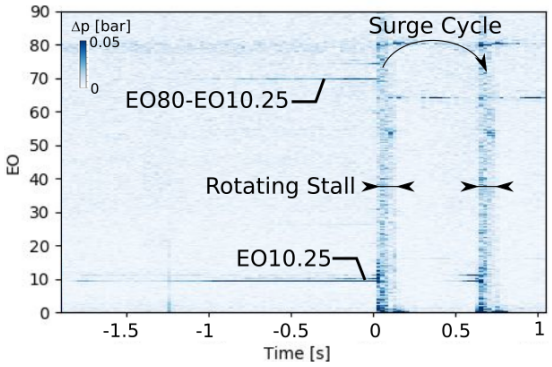

(b) Spectrogram during a throttling maneouver into rotating stall, non periodic fluctuations of the wall pressure upstream of Rotor 3 Leading Edge

Figure 5.8: Experimental setup and wall pressure spectrogram during stall approach

5.2 Spinning acoustic modes

5.2.1 CREATE Multistage compressor: Non-synchronous activity near stall

A different nature of acoustic resonance has been observed in a multistage compressor at ECL. The machine CREATE, schematically shown in Fig. 5.8a is representative of the rear stages of an high-speed 3.5 stage compressor. At different speedlines significant non-synchronous activity has been observed when approaching the stability limit. Figure 5.8b shows the spectrogram of a wall pressure sensor during a throttling maneuver, exhibiting a clear peak at a frequency of Engine Order $EO10.25$, rising over hundreds of revolutions before entering rotating stall and surge. At the same time, modulations of this mode with the blade passing frequency were observed. While previous studies on this phenomenon indicated a convective or rotating stall like disturbance as the source (Courtiade and Ottavy, 2013), a method of using correlations of multiple pairs of wall pressure sensors allowed the clear characterization as a spinning acoustic mode.

Experimental characterization of spinning modes

Using the circumferential distribution of sensors it is possible to derive the propagation speed of pressure waves by performing pairwise cross-correlations. The cross-correlation $p_1 \star p_2$ between sensors 1 and 2 for example, is given by eq. 5.1:

$$p_1 \star p_2(j) = \frac{1}{I} \frac{1}{\overline{\sigma}(p_1)\overline{\sigma}(p_2)} \sum_{i=0}^{I-j-1} \Delta p_1(i)\, \Delta p_2(i+j) \tag{5.1}$$

where I is the number of samples per revolution. Signals normalized with the average pre-stall standard deviation $\overline{\sigma}$. Each phase-shift, j, can be related to a propagation phase velocity Ω_a^S in the stationary frame of reference. Expressed as a fraction of the rotor speed Ω_r, this velocity becomes:

$$\frac{\Omega_a^S}{\Omega_r} = \frac{\Delta\Theta_{12}/360^\circ}{j/I} \tag{5.2}$$

To increase accuracy, pairwise cross-correlations of all circumferentially distributed sensors are calculated and mapped onto a common propagation velocity vector. Afterwards, the minimum of the individual correlations for each propagation velocity is derived to eliminate aliased correlation peaks (Brandstetter et al., 2018).

Using the derived propagation velocity Ω_a^S and the frequency of the pressure fluctuation in the stationary frame ω_a^S it is possible to calculate the circumferential wave number of the aerodynamic disturbance (N_a) according to eq. 5.3:

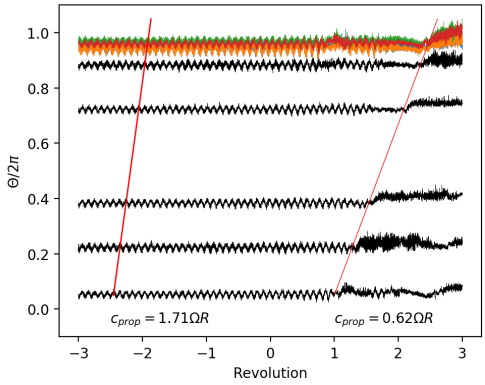

(a) Pressure traces near leading edge of Rotor-3 during stall onset, black lines Stage 280, colored lines above Rotor-3 LE

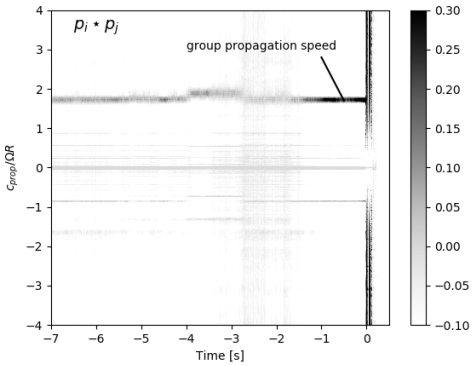

(b) Measured temporal evolution of dominant group velocity near leading edge of Rotor-3; Minimum of all pairwise cross correlation coefficients

Figure 5.9: Analysis of disturbance propagation speed before stall onset

$$N_a = \frac{\omega_a^S}{\Omega_a^S} \tag{5.3}$$

The transformation to the rotor-relative frame of reference leads to:

$$\frac{\omega_a^R}{\Omega_r} = (\frac{\Omega_a^S}{\Omega_r} - 1) \cdot N_a \tag{5.4}$$

To derive the propagation speed of the observed mode, the group velocity is analyzed using distributed sensors near the leading edge of Rotor-3. The time history during the last revolutions before rotating stall are presented in Fig. 5.9a. The black lines represent the measurements in stage 280 upstream of the LE, the colored above Rotor-3 near LE.

The stall cell propagates with 0.62 Ω_r as can be derived from these traces. For the periodic pre-stall signal pairwise cross-correlations of all these sensors have been calculated.

The minimum value of these correlations is presented in Fig. 5.9b, exhibiting a dominant co-spinning propagation speed around 1.7 Ω_r, coherently developing with the amplitude rise of the $EO^S10.25$ mode in the last second before stall, clearly indicating acoustic propagation. Secondary peaks (EO9.4) have been observed which could also be identified as spinning acoustic modes, and are described in detail by Brandstetter et al. (2019b).

Axial propagation of modes

The axial distribution of the acoustic pressure associated to the respective modes is presented in Fig. 5.10, showing a clear maximum near the leading edge of Rotor-3. Both modes decay rapidly downstream with evanescent amplitude near the trailing edge of Rotor-3. In contrast, the amplitude decays slowly in the upstream direction. This distribution is representative for both modes and for all repeated measurements at design speed.

To determine the cause for the amplitude decay a coarse approximation of the acoustic cut-off condition can be made as described in section 2.5 using the averaged values of probe measurements for total temperature, Mach number and swirl angle upstream and downstream of Rotor-3. For co-spinning modes the cut-on condition depending on the wave number is presented in Fig. 5.10b. For the measured peak at $EO^S10.25$ circumferential wave numbers between 6 and 8 satisfy the condition of being cut-on upstream and cut-off downstream. For the peak at $EO9.4$ the condition applies to N_a 5 to 7, with 5 being at the limit of being also cut-on downstream. Yet, the measured axial development of Mode $EO^S9.4$ (Fig. 5.10a) indicates cut-off conditions downstream due to the exponential amplitude decay in Rotor-3.

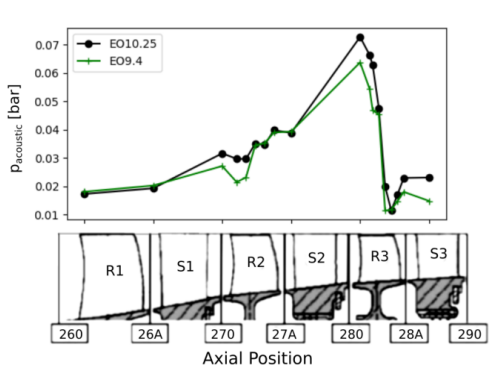

(a) Axial distribution of maximum pre-stall amplitude of the non-synchronous modes

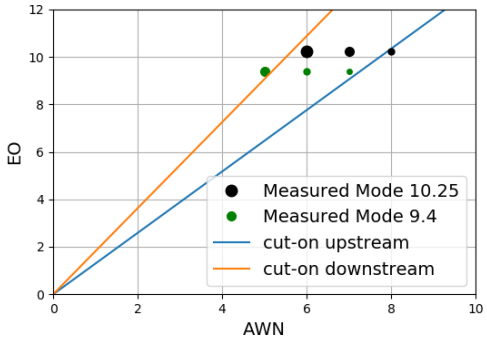

(b) Cut-on conditions up- and downstream of Rotor-3, Values calculated based on averaged probe measurements in section 280 and 28A

Figure 5.10: Acoustic mode analysis

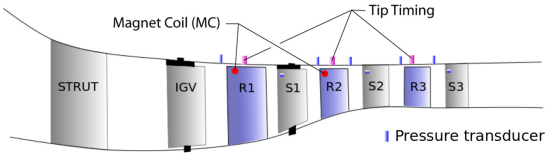

(a) Schematic of Safran Helicopter Engines test compressor

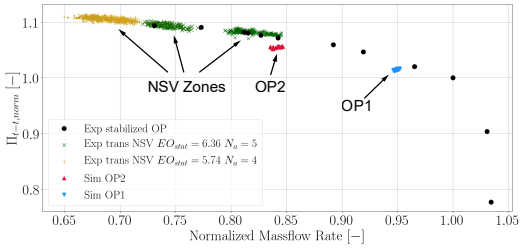

(b) Compressor characteristic from experiment; indicators for non-synchronous activity in transient experiment and simulation (Fiquet et al., 2019)

Figure 5.11: Test setup and compressor characteristic

In the publication (Brandstetter et al., 2019b) we show a deeper analysis into additional convective effects and coupling with blade vibration, but the most significant finding is that all acoustic modes which evolve are cut-on in the upstream direction and cut-off downstream of Rotor-3. As a source for the acoustic mode vortex shedding from the overloaded Rotor-3 is indicated. These results are in close correspondence with the study of A. Fiquet, which is described in the following section.

5.2.2 ASTEC2 Multistage compressor: Non-synchronous activity at stable operating conditions

A similar phenomenon of spinning acoustic modes was studied in the PhD research of Anne-Lise Fiquet under supervision of the author. Here, an axial multistage compressor for helicopter engines was experimentally investigated at part-speed conditions and showed significant non-synchronous acoustic signatures, which were coincident with excessive blade vibration[1]. The research compressor rig designed by Safran Helicopter Engines is composed of struts, variable inlet guide vanes (IGVs) and three axial compressor stages, as illustrated in Fig. 5.11a.

In contrast to all previously described phenomena, this machine suffered from non-synchronous activity far from the stability limit as indicated in Fig. 5.11b through the green and yellow symbols. First traces of non-synchronous activity were already detected between OP1 and OP2, and two dominant acoustic modes were observed during testing. The following describes the activity during a transient throttle manoeuvre.

[1]For the machine CREATE described in the previous section, blade vibrations were also assumed but could not be measured due to missing instrumentation

Experimental measurements

At a normalized mass-flow rate of 0.85, non-synchronous pressure signals are measured at frequency $EO^S 6.36$, as seen in Fig. 5.12, indicated by green markers in Fig. 5.11b. Throttling further towards stall, the pressure wave changes its frequency to $EO^S 5.74$ whereupon the blade vibration amplitude diminishes (corresponding to yellow markers 5.11b).

The temporal evolution of these modes, measured with a pressure sensor near rotor 2 is shown in Fig. 5.12. It can be seen that the switch between the two modes occurs without significant change in amplitude.

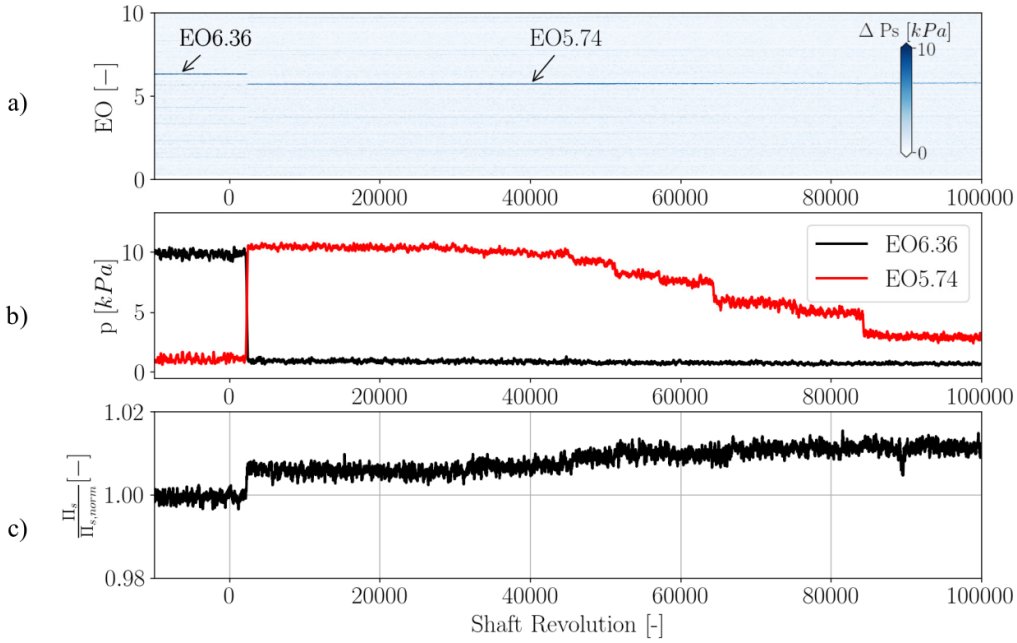

Figure 5.12: a) Frequency spectrogram of pressure fluctuation during transient test, Leading Edge of Rotor-2, b) Modal pressure amplitude, c) Static pressure rise of compressor; from (Fiquet et al., 2019)

Fig. 5.13a, left graph, shows the pressure spectrum at the leading edge of Stator-2 and the frequency spectrum of a 'Magnet-Coil' signal measured in Rotor-2, right graph, before the frequency switch occurs. The spectra reveal several non-synchronous frequencies. The strongest blade vibrations are measured at a frequency of $EO^R_{Rotor-2} = 2.72$, which corresponds to the first blade eigenmode. At this frequency, tip timing data presented in Fig. 5.13b indicates a dominant nodal diameter of $N_v = +10$. The 2^{nd} harmonic of the pressure mode at $EO^S = 12.72$ exactly coincides with the frequency of the blade vibration at $N_v = +10$ (in the stationary frame of reference). It is hence evident that the blade vibration is excited by the pressure wave and not responsible for it, as the fundamental pressure mode ($N_a = 5$) cannot be excited by an harmonic. This is confirmed by an off-resonant excitation of the blades measured at $EO^R = 1.34$, which coincides with the fundamental mode in the stationary frame of reference. Both pressure wave and structural nodal diameter are forward travelling (spinning in the same direction as the shaft) with a speed at the casing higher than the rotor speed ($\Omega^S_a = 1.27\Omega_r$), which hints at an acoustic nature.

As the machine is throttled, the circumferential wave number of the pressure disturbance changes to $N_a = 4$ (Fig. 5.14a) and blade vibration of Rotor-2 reduces significantly, shown in Fig. 5.14b. At this condition, neither the fundamental acoustic mode ($N_a = 4$, $EO^S 5.74$) nor its harmonic ($N_a = 8$, $EO^S 11.48$) are coherent with the blade eigenmode 1 in the relative frame of reference, explaining the reduced vibration. It is hence evident, that aerodynamic conditions are responsible for wave-number and frequency of the acoustic mode and blade vibrations result solely from excitation.

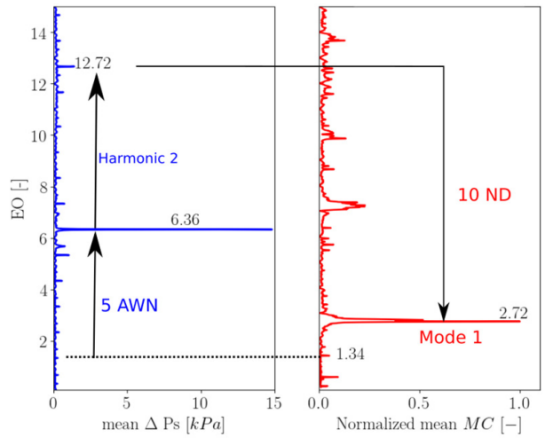

(a) Frequency spectra at OP2 of unsteady wall pressure (ΔPs) at leading edge of stator-2 in the stationary frame of reference and magnet-coil signal in rotor-2 in the relative frame of reference (MC)

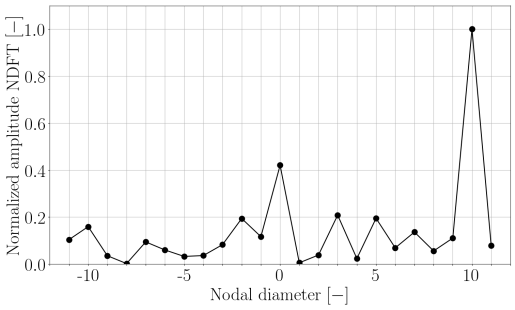

(b) Nodal diameter decomposition, estimated from tip-timing results in rotor-2 for the first blade eigenmode $eo_{rel} = 2.72$, operating point OP2

Figure 5.13: Waveform analysis of pressure wave and structural vibration before frequency switch from Fiquet et al. (2019)

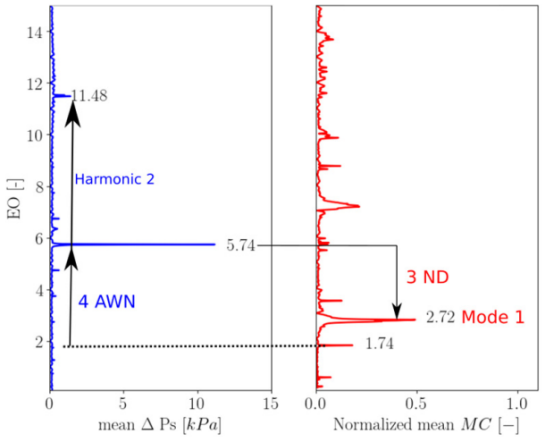

(a) Frequency spectra at OP2 of unsteady wall pressure (ΔPs) at leading edge of stator-2 in the stationary frame of reference and magnet-coil signal in rotor-2 in the relative frame of reference (MC)

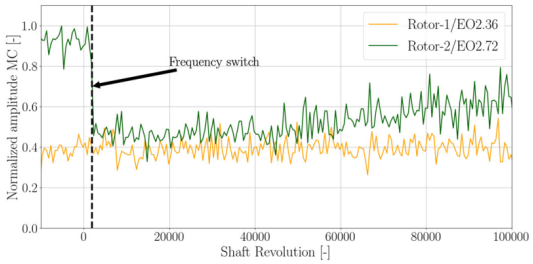

(b) Amplitude of the first eigenmode of Rotor-1 (EO2.36) and Rotor-2 (EO2.72) (from magnet-coil sensors)

Figure 5.14: Waveform analysis of pressure wave and structural vibration, a) after frequency switch from Fiquet et al. (2019)

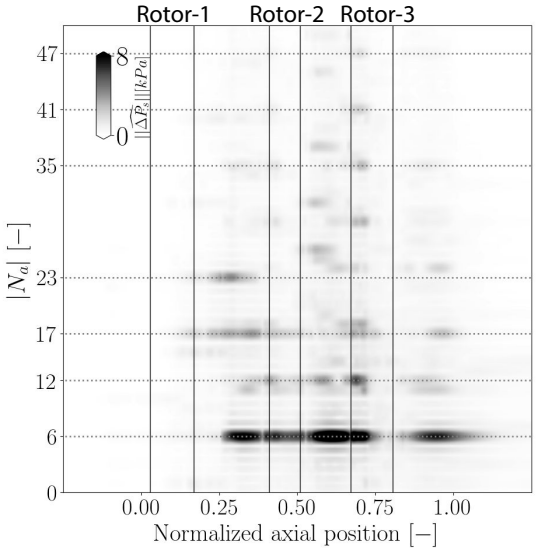

(a) Axial evolution of the circumferential wave number ($|n_a|$) based on static pressure signal at 99.5% of channel height, URANS OP2

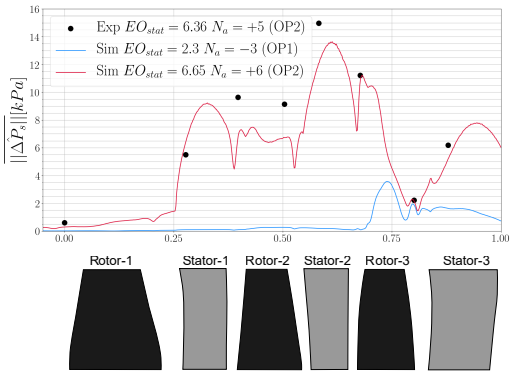

(b) axial distribution of the amplitude of non - synchronous pressure mode, experimental results at OP2, numerical results for OP1 and OP2

Figure 5.15: Amplitude of pressure mode in numerical simulations and comparison with experiments, (Fiquet et al., 2021a)

Numerical characterisation

In order to analyze the origins of this pressure mode a numerical simulation was conducted and reported in (Fiquet et al., 2021a) and (Fiquet et al., 2021b). The whole compressor was considered in a full-annulus simulation without axial mixing planes. Unsteady simulations have been performed at two operating points, depicted in Fig. 5.11b as OP1 and OP2.

The non-synchronous flow field at 99.5% of channel height is decomposed by applying a spatial filter of the circumferential signal for each individual time step depending on the modulus of the circumferential wave number $|N_a|$, and secondly by calculating the temporal Fourier transform of the spatially filtered data over 8 rotations. Applying the detailed decomposition in a rotor, the frequency in the relative frame of reference EO_{rel} is derived for a fixed circumferential wave number.

As shown in the pressure spectrum in Fig. 5.15a, a dominant circumferential mode order of $|N_a| = 6$ develops in the simulation at OP2. This mode ($|N_a| = 6$), its harmonic ($|N_a| = 12$) and their modulations with the blade number of Rotor-3 ($|N_a| = 23 - 12 = 11, |N_a| = 23 - 6 = 17, |N_a| = 23 + 6 = 29$) are clearly visible. Axially, the fundamental mode appears at high amplitude in both Stage-2 and Stage-3 with a maximum peak in Stator-2. Analysis of the propagation speed of this mode confirms that it is of acoustic nature. In Fig. 5.15b the amplitude is compared to the experimental measurements showing remarkable agreement of amplitude and axial evolution.

Origin of acoustic modes

To analyze the emergence of the pressure mode, the flow structure in all stages has been analysed in detail (Fiquet et al., 2021a). At different time instances, Fig. 5.16 shows the evolution of the boundary layer in Rotor-3, where a high amplitude of the acoustic mode was observed. The blue isocontour at $M_{rel} = 0.3$ in indicates the flow detachment near the leading edge close to the hub, extending radially towards the trailing edge. Instantaneous streamlines are shown to visualize radial migration in the downstream part of the blade. During one period of the $N_a = 6$ mode the shape of the separation fluctuates radically. However, this mechanism does not lead to a total breakdown of the compressor performance. The circumferential pattern of mode $N_a = +6$ in Rotor-3 does not propagate with a typical convective speed but rather follows a periodic resonance with the passing acoustic mode. This point is important, since it is effectively a modulation of flow separation zones and not a circumferential propagation in form of stall cells in the sense of Emmons (1955). With these

results, it is clear that a strong interaction between the acoustic mode and the flow separation zone occurs, which strongly modulates its shape and extension during one oscillation cycle. For the lower throttled point OP1 the same phenomenon was observed but with a backward traveling acoustic mode of order $N_a = -3$ and lower intensity (Fiquet et al., 2021a).

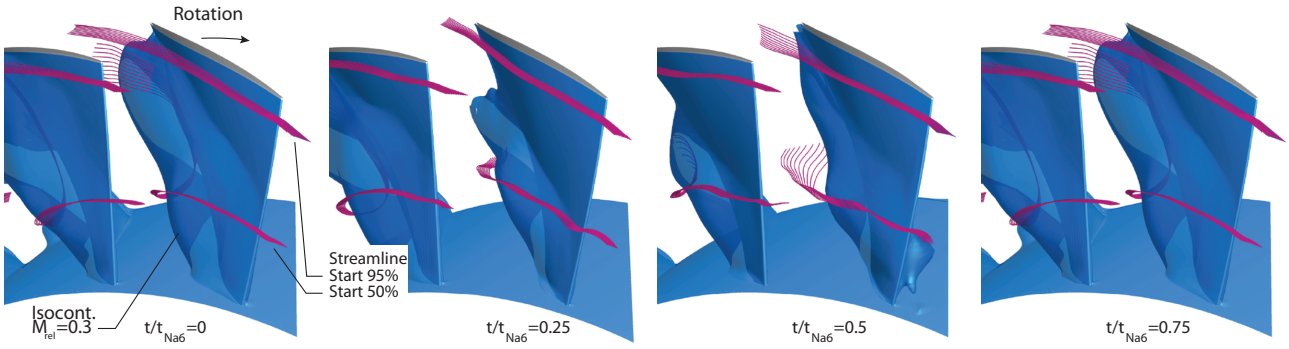

Figure 5.16: Fluctuation of flow structure on suction side of Rotor-3 during one cycle of Mode $N_a = +6$, Isocontours at relative Mach number M_{rel}= 0.3; values blanked above 98% of channel height; instantaneous streamlines starting near leading edge at 50% and 95% of channel height, URANS OP2, (Fiquet et al., 2021a)

Further comparison of the simulation results at OP1 and OP2 unveiled the mechanism responsible for the emergence of the acoustic modes. Fig. 5.17 presents an instantaneous distribution of the non-synchronous entropy signal at OP1. Emerging from Rotor-3, entropy waves are convected downstream and interact with Stator-3, forcing highly unsteady loading which is transformed into a pressure wave that can propagate upstream. The circumferential mode $N_a = -3$ is clearly apparent in Stage-3, circumferentially propagating against the rotor direction.

The analysis of the acoustic propagation conditions in Fig. 5.19 indicates that the observed counter rotating mode at OP1 of $N_a = -3$, $EO_{stat} = 2.3$ is cut-on only downstream of Rotor-3 while it is cut-off upstream.

Hence, the acoustic mode generated in Stator-3 can propagate upstream into Rotor-3 where it is cut-off due to the change in swirl velocity. Here, a strong interaction with the flow separation zone occurs and enforces a phase lock-in. Since this flow structure is the source for the entropy wave, which was necessary to produce the unsteady loading on Stator-3, a resonant system in the gap between the rotor and the stator establishes, We hence observe a circumferential coupling (lock-in) of flow separation zones in Rotor-3, whose wave characteristic is dominated by the acoustic propagation conditions.

Fig. 5.18 shows the non-synchronous entropy signal at OP2. The entropy signal is less organized compared to OP1 but the mode $N_a = +6$ is clearly visible in Stator-1 and Stage-2. In Stator-3 and downstream, the convective mode $N_a = +5$ is obvious. The same principal phenomenon observed at OP1 is present but in this case also involving Stage-2.

Through increased loading, flow separations in Rotor-2 develop and produce entropy waves which are convected downstream, leading to unsteady loading of Stator-2. In the same way as described above, an acoustic resonance establishes with a dominant mode, which is partially trapped in the compressor. At OP2, the mode is propagative upstream between the leading edge of Stator-1 and the trailing edge of Rotor-3 (see Fig. 5.15b). Through axial convection of the corresponding entropy waves the mode is observed also in Stator-3 but cannot propagate acoustically out of the stage.

In the analyzed configurations, the source for acoustic modes is identified not to be a typical vortex-shedding mechanism, but rather a flow separation zone which creates unsteady loading on downstream stators. The generated acoustic wave establishes at a circumferential mode order that fulfills the condition of being cut-on only in one direction.

The most important finding is that a pressure wave establishes due to a coupling of flow separation zones and spinning acoustic modes which only in one case coincides with a blade eigenmode and leads to critical vibration.

In all observed cases, the relevant acoustic mode was observed to decay rapidly in vicinity of

the highly loaded stage 3, indicating cut-off. To investigate the rapid decay of the pressure modes at certain axial positions the acoustic propagation conditions have been calculated as described in section 2.5.

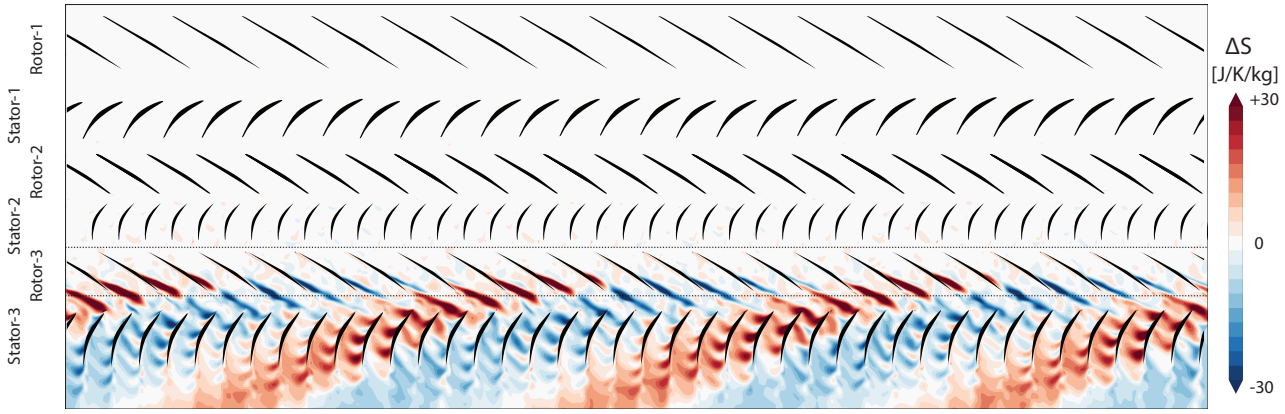

Figure 5.17: Unsteady non-synchronous entropy at OP1 for one time instant at 80% of channel height (Fiquet et al., 2021a)

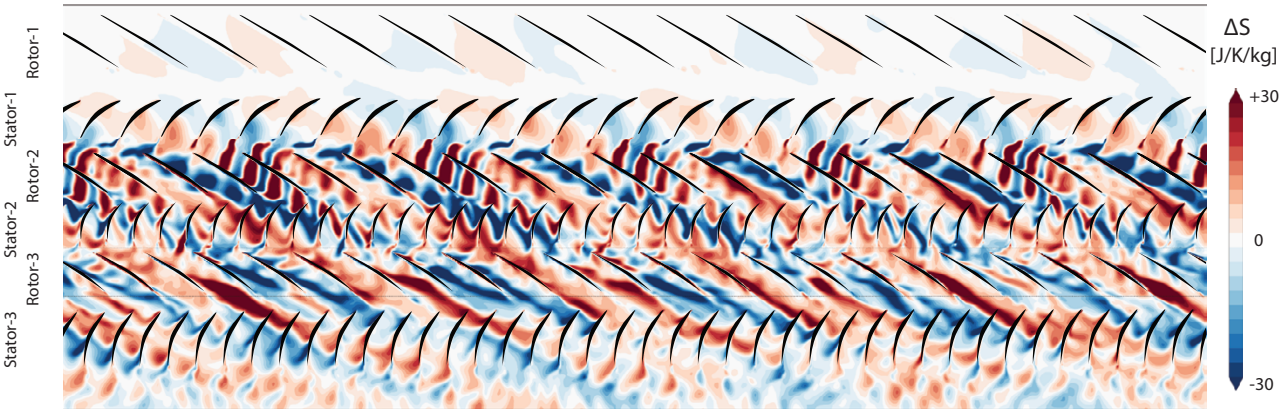

Figure 5.18: Unsteady non-synchronous entropy at OP2 for one time instant at 80% of channel height (Fiquet et al., 2021a)

Fig. 5.19 represents the cut-off condition upstream and downstream of Rotor-3 based on the URANS results at OP1 and OP2.

All observed modes in experiment and simulation are depicted as symbols, clearly showing their location at the limit of being propagative only in one axial direction of Rotor-3, both for co- and counter-rotating modes. The analysis furthermore explains the frequency switch from $N_a = 5$ to $N_a = 4$ in the experiment, as due to increased loading during the trottling maneuver the first mode eventually becomes cut-off (Fiquet et al., 2021a).

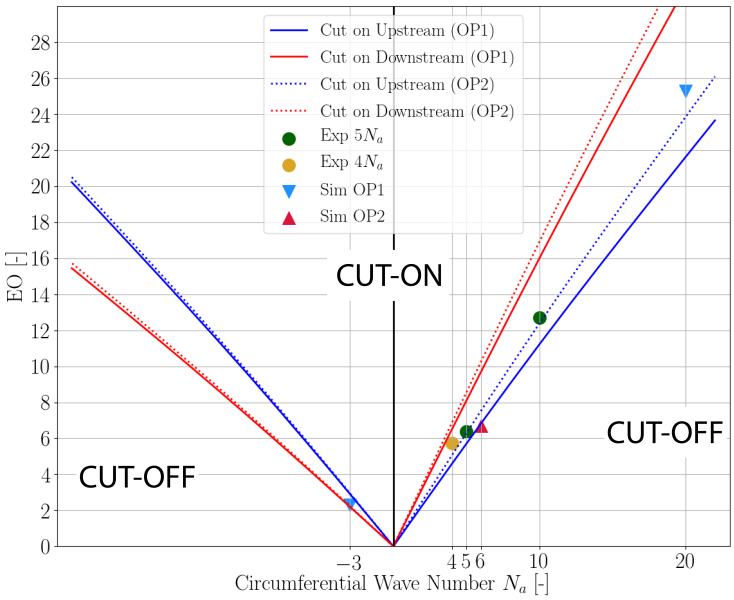

Figure 5.19: Frequency and circumferential wave number of acoustic modes in experiment and simulation, cut-on conditions upstream and downstream of rotor-3 (URANS simulations), (Fiquet et al., 2021a)

Conclusions on trapped acoustic modes

This study was of great interest for our phenomenological understanding because of the following points.

- The reason for the occurrence of non-synchronous blade vibration in a relevant application could be physically explained and identified as a non-synchronous forced response mechanism
- Trapped acoustic modes could be clearly characterized using multiple instrumentation systems
- A full annulus multi-stage numerical setup with moderate resolution was capable to reproduce the phenomenon without application of blade vibration
- The simulations clearly helped to understand the physical reason for the emergence of the acoustic modes
- It was shown that a simple analysis of acoustic propagation conditions is a suitable indicator for critical modes, as all observed pressure waves were at the limit of being cut-off in one axial direction of the highest loaded rotor

The last point is even more relevant, as comparison with the results from the machine CREATE shows very similar characteristics. Both machines are fundamentally different from their architecture, CREATE representative of rear stages of a turbojet compressor with 80 blades in the relevant rotor, the ASTEC2 machine much smaller in size and only comprising 23 rotor blades, representative of front stages of a helicopter engine. However, axial amplitude evolution as well as near cut-off condition of observed modes in Fig. 5.10 is in close agreement with the graphs shown in Fig. 5.15b and 5.19, indicating that the phenomenon may be of general nature but could not be explained before.

Chapter 6

Application of knowledge for signal interpretation

Based on the findings described in the previous sections, it is possible to interpret signals occurring in the pre-stall phase by decomposing them into different frequencies and circumferential modes and assigning them to physical mechanisms. This enables the interpretation of measurement signals even during strong aeromechanical interactions as we demonstrated in (Brandstetter et al., 2021a). In the following, the procedure is presented for the case of the composite low-speed fan which was previously discussed in Section 4.2.3. The fan suffered non-synchronous-vibrations, which were accompanied by measured pre-stall pressure spectra resembling those of commonly associated with "Rotating Instabilities". As already indicated, the fan vibrated in nodal diameter 3 ($N_v = 3$) at 85% speed, which was in resonance with an aerodynamic disturbance of wave number 13, aliasing on a 16-bladed rotor (comp. Fig. 4.14). The pressure spectra at during this event are shown in Fig. 6.1a, plotted against axial location. In Brandstetter et al. (2021a) we discuss in detail how these can be interpreted. Amplitude maxima for broadband noise and several frequency peaks near the rotor leading edge, which decay in both axial directions (for example EO3.22, 4.19 etc.) are clearly visible. Other peaks, such as EO8.46 or 12.76 remain at constant amplitude. Using the method to derive disturbance propagation speeds described in section 5.2 the values for Ω_a^S/Ω_r could be calculated for the bandpass filtered signals of individual frequency peaks, and these are presented in Fig. 6.1b. This allowed to determine the wave-number N_a of each mode. It can be seen that a group of modes propagate at an angular velocity of approximately 55% of the rotor speed. Specific modes propagate faster that the rotation speed (EO8.46, EO10.78 etc).

This table (Fig. 6.1b) shows that some of the spectral peaks can be assigned to consecutive wave numbers ($N_a = 11, 12, 13$ and $N_a = 17, 18$). The propagation speed of these modes differs by less than 10%. The highest amplitude at the leading edge position is measured for the peak at EO8.46 which has a propagation speed of $\Omega_a^S = 2.82\Omega_r^S$. This matches the phase speed of the structural vibration of Mode 3, $N_v = 3$ forward travelling, which has a frequency of EO5.46 in the rotating frame of reference. The peak at EO7.53 has the same frequency in the rotating frame of reference and a circumferential wave number N_a=13 which excites a forward travelling N_v=3 vibration on the 16-bladed fan. The relationship of the frequencies in the stationary frame of reference is given by:

$$N_b - \frac{\omega_a^S}{\Omega_r^S} = \frac{\omega_v^S}{\Omega_r^S} \rightarrow 16 - 7.53 = 8.46 \tag{6.1}$$

This resonance, or lock-in, of an aerodynamic disturbance with a structural vibration pattern is the "Non-Synchronous-Vibration", discussed in this manuscript. The acoustic wave generated by the blade vibration (EO8.46, $N_v = 3$) is propagative (cut-on) in both axial directions of the duct, explaining the non-decaying amplitude visible in Fig. 6.1a.

Further correspondence between structural modes and aerodynamic disturbances is found for the peaks EO3.22, EO4.19 and EO5.15, which can be associated with vibration patterns of the second blade eigenmode $\mathrm{EO}_{M2}^R = 3.8$ in nodal diameters $N_v = -7, 7$ and 8 as denoted in Column 5 of Fig. 6.1b. Negative values of N_v represent backward travelling nodal diameters. The peaks at EO10.78, EO11.79 and EO12.76 are acoustic signatures of these vibration modes. In contrast to the signature of peak EO8.46, those modes are cut-on only in the upstream direction with $\Omega_a^S/\Omega_r^S \approx 1.5$ and decay in the downstream direction. The peaks above the blade passing frequency correspond to scattered modes with the first and second blade passing harmonic, as denoted in Fig. 6.1b.

These relations between aerodynamic disturbances and blade vibration patterns are visualized in Fig. 6.2 where the measured propagation speed is plotted against the corresponding wave number

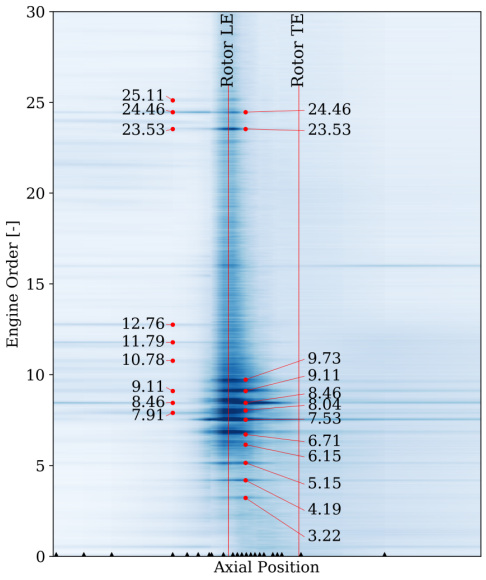

(a) Wall pressure spectrum of fan operating near stall, subtraction of ensemble average

EO^S	EO^R	N_a	$\frac{\Omega_a^S}{\Omega_r^S}$	Description	Decay Half life
3.22	3.78	7	0.460	NSV M2 N_v-7	0.5
4.19	3.81	8	0.524	NSV M2 N_v8	0.8
5.15	3.85	9	0.572	NSV M2 N_v7	0.7
6.15	4.85	11	0.559	free conv.	0.4
6.71	5.29	12	0.559	free conv./NSV	0.4
7.53	5.47	13	0.579	NSV M3 N_v3	1.8
8.04	6.96	15	0.536	free conv.	0.8
8.46	5.46	3	2.820	Acoust. M3 N_v3	2.7
9.11	7.89	17	0.536	free conv.	0.4
9.73	8.27	18	0.541	free conv.	0.6
10.78	3.78	7	1.540	Acoust. M2 N_v7	1.3
11.79	3.79	8	1.474	Acoust. M2 N_v8	1.1
12.76	3.76	9	1.418	Acoust. M2 N_v9	2.6
23.53	5.47	29	0.811	N_b16 + N_a13	0.7
24.43	5.43	19	1.286	2xN_b16 - N_a13	2.6
25.11	7.89	33	0.761	N_b16 + N_a17	0.6

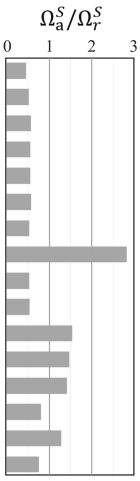

(b) Decomposition of spectral peaks, chart representing angular velocity of disturbance

Figure 6.1: Spectral analysis of pre-stall signature

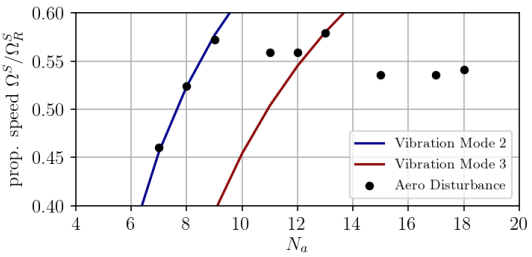

(a) mode propagation speed

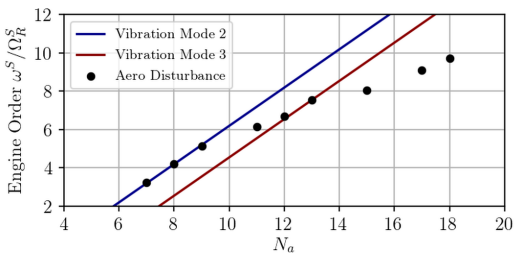

(b) mode frequency in dependence of wave number

Figure 6.2: Characteristics of individual modes

N_a and compared against the phase velocity of the blade vibration modes 2 and 3 (or that of the aliased mode $N_a = N_b - N_v$). It can be seen that wave number N_a=13 is in resonance with Mode 3 ($\frac{\Omega_a^S}{\Omega_r^S} = 0.579$). The speeds of aerodynamic disturbances N_a=7 to 9, however, all align with that of Mode 2 vibration modes. This correspondence is also visible in Fig. 6.2b, which plots frequency against wave number. The frequencies for wave numbers 7 to 9 are separated by integer engine orders.

In (Brandstetter et al., 2021a) we introduce a method to approximate the decay of disturbances by considering the cross-spectral coherence between circumferentially distributed sensors. The last column in Fig. 6.1b shows the half-life for the individual modes, indicating the number of revolutions in which the amplitude of the mode decays by 50%. The values for the convected modes which are not locked-in lie between 0.4 and 0.8 revolutions. This agrees with findings by Eck et al. (2020) who reports that rotating instability disturbances are still traceable after having travelled a quarter of the circumference. The acoustic and structural interaction modes in the present test case remain coherent for longer, with a half life of up to 2.7 revolutions. These results are particularly interesting when comparing the results concerning aerodynamic mistuning in Section 4.6.4, where instability was predicted by the NSV model for a convective disturbance half life of approximately 3 blade passages in a perfectly tuned case and about 5 passages for 1% structural mistuning on a 21-bladed rotor, representing values of 0.15 to 0.25 in column 6 of Fig. 6.1b. Hence, the values measured for the given low-speed fan are of the same order of magnitude, further indicating similarities between the low speed fan and high speed compressor concerning NSV.

Chapter 7

Open Test Case Fan ECL5

To pursue the research of the author and the turbomachinery group of ECL concerning multi-physical interaction mechanisms between aerodynamics, structure-dynamics and acoustics, an open-test-case fan stage has been developed. For its experimental investigation, the author is currently coordinating the European Cleansky-2 project CATANA (Composite Aeroelastics and Aeroacoustics) in cooperation with the Von-Karman-Institute for Fluid Dynamics in Brussels.

The rotor is fabricated from composite material and representative of near-future fans for Ultra-High-Bypass-Ratio turbofans, running at low transonic speed. The focus of the experimental investigations - which will start in 2022 - will be on the measurement of unstable aerodynamic phenomena and aeroelastic interaction. Particularly, synchronized measurements with time resolving measurement techniques and laser-optical methods are envisaged. The configurations comprise intentional structural mistuning and a variation of the engine intake. The ambition of project CATANA is to provide a substantial scientific basis for the advancement of multi-physical methods, necessary to enable the development of future UHBR composite fan engines. The scientific goal is to clearly understand the chain of cause and effect leading to instability in low-speed composite fans, particularly to identify and characterize the respective mechanism and to enable the scientific community to exploit the results through complete access to the test geometry and its structural properties.

7.1 Design

The general objectives for the design of an open-test-case that is relevant for multi-disciplinary fan-research comprise requirements concerning representativity with near future engine designs:

1. General aerodynamic design parameters need to be similar (Mach number, blade loading, solidity, aspect ratio, hub-to-tip ratio, mass flow density, etc.)

2. The aerodynamic flow structure should be comparable due to the influence on instability mechanisms. This applies particularly to shock patterns and secondary flow structures

3. The scaling of the rotor to facility size should maintain the representability

The most severe conceptual problem is that it is obviously not possible to design a stage that is representative for all families of modern aircraft fans. Thus, it has been decided to create a completely new fan stage whose design parameters are relevant for ultra-high bypass engine applications in the next decade. From the current point of view, the most promising research configuration is a UHBR low-speed fan stage with high subsonic design speed, designated to be installed in midrange aircraft, such as the Airbus A320neo.

Industrial low-speed fans For orientation, a selection of the state-of the art of High-Bypass-Ratio engines is presented in Fig. 7.1. The propulsion industry has focused on different strategies but all share common design trends: reduction of tip speed, reduction of number of blades and the reduction of individual blade weight.

General Electric started in the 1990s with the establishment of layered carbon fibre composite fan blades in the GE90 engine for wide body aircrafts and is the only manufacturer with in-service composite fans. The more recent GEnx shows a reduced blade number of 18. Following this development, the CFM LEAP engine was developed for the A320neo class, with 18 blades constructed from 3d-woven carbon fibres. Pratt&Whitney introduced the first Geared Turbofan with 20 (hybrid)-metallic blades, also for the A320neo class. In-service Rolls-Royce engines still comprise hollow titanium blades but technology demonstrators based on variants of the Trent1000 engine incorporate composite fibre fan blades. As an example for the Rolls-Royce family, the fan of the Trent XWB engine for the Airbus A350 with 22 metallic blades is shown in Figure 7.1 (the Trent 7000 has 20 blades).

Figure 7.1: Selection of established modern High-Bypass-Ratio Engines (**a**) **GE90 (2003)** (22 comp. blades, Ø 330cm, BPR 9, 2355rpm, M_r^{tip}1.2 (nom.) (**b**) **GEnx (2011)** (18 comp. blades, Ø 282cm, BPR 9.1, 2560rpm, M_r^{tip}1.11 (nom.) (**c**) **CFM LEAP (2015)** (18 metallic blades, Ø 198cm, BPR 11, 3894rpm, M_r^{tip} 1.19 (max.) (**d**) **PW1100G (2015)** (20 comp. blades, Ø 206cm, BPR 12, 3500rpm, M_r^{tip} 1.11(max.) (**e**) **RR XWB (2013)** (22 comp. blades, Ø 300cm, BPR 9.6, 2700rpm, M_r^{tip} 1.25 (nom.)

All of the shown fans comprise significant 3D-features, particularly forward sweep which is known to be beneficial for aerodynamic performance but emphasize aeroelastic sensitivity for torsional or chordwise bending modes and particularly NSV. Recent research (Goerke et al., 2012; Schmid et al., 2019) showed that the use of anisotropic properties of composite in fans could help to improve both mechanics and aerodynamics. Composites also present potential to control flutter by modification of eigenmodes (Reiber and Blocher, 2017).

Design strategy In order to enable further technological advancements into this direction, extensive research is necessary to identify and characterize the relevant instability mechanisms for the novel type of low-speed fans. Particularly the complex flow structure at part load and part speed is challenging for state-of-the-art numerical approaches and requires experimental benchmark data on representative geometries.

Under coordination of the author the open-test case ECL5v4 has been designed at ECL. The development has been described in detail by Brandstetter et al. (2021b), Pages et al. (2021) and the thesis of Valdo Pages which will be published in 2022. In the following, an overview of the objectives and numerically predicted characteristics is presented.

Based on an initial design by Rendu (2016), a fan stage geometry was obtained with the use of a modularly coupled design chain, including a parametric blade geometry generator, automatic meshing, a steady RANS solver, and structural FEM simulations.

The aerodynamic design point for the UHBR-fan has been defined at a minimum total pressure ratio of 1.36 at a mass flow density maximum of 200 kg/s/m² to be achieved at a high subsonic relative tip Mach number. The (numerical) rotor-only isentropic efficiency at the design point exceeds 94% with a stall margin of at least 10%. A secondary transonic design point has been defined at 110% nominal speed (110Nn), at which the rotor efficiency does not drop below 92%. This objective has been chosen to ensure the possibility for transonic experiments. Even though future UHBR Fans might be operated solely subsonic, it was desired to achieve a test-case that is adequately representative of current (low) transonic designs such as presented in Fig. 7.1. An optimization of the profiles only at nominal speed would lead to poor transonic performance. Based on these fundamental requirements, further design objectives result from the intended application on the test rig. This applies to geometrical dimensions,

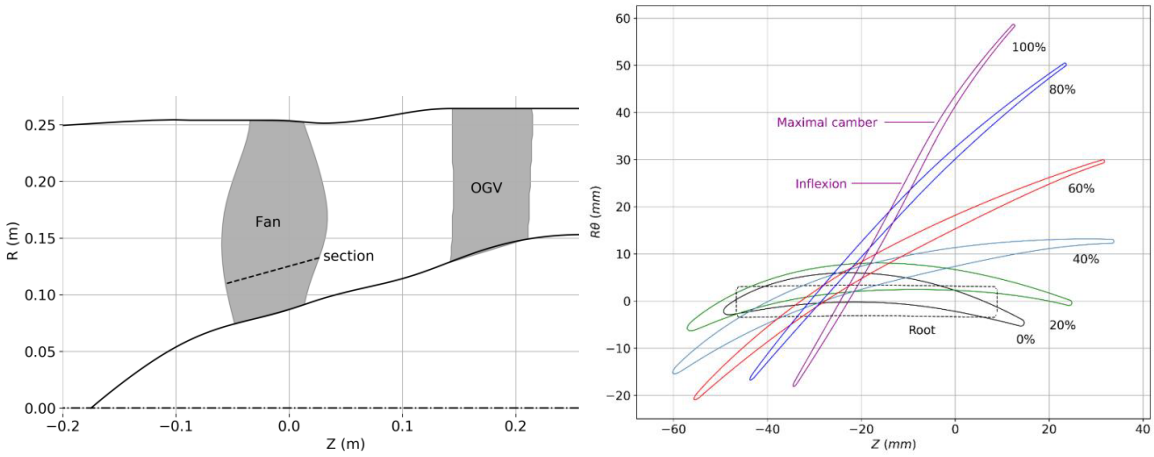

Figure 7.2: ECL5 fan stage view (**a**) Section of fan stage (**b**) Rotor profiles at different span heights from (Brandstetter et al., 2021b)

mechanical constraints and the intention to use a rotor disk available at the institute. The number of blades is fixed to 16, representing the lowest number realized in modern concepts. For the stator, no specific design criteria were set except for a minimization of (numerical) corner separation at highly loaded conditions and minimum losses at Design Point. The blade number was fixed to 32 in the optimization process and reduced to 31 for the final design to avoid the establishment of planar acoustic interactions.

The stage inlet and outlet geometries and the casing in the rotor section are similar to previous installations (Rodrigues et al., 2021). The OGV is located far downstream of the fan to minimize interactions as the focus of the research project lies on the rotor. As the facility comprises only a single flow channel, engine representative stator aerodynamics are not intended, merely axial stage outflow and homogeneous radial conditions are required to ensure detailed performance analysis and to enable future research projects with fundamental background on noise generation. A section of the stage design is presented in Figure 7.2a.

Figure 7.2b shows the blade profiles at different span heights, clearly emphasizing the transonic blade design at the rotor tip and the wide chord geometry around midspan. At the hub, the relative tangential velocity and the rotational speed have the same direction, which is necessary to meet the design criteria laid out above but creates a challenging flow field with high swirl velocities at the OGV inlet.

In Figure 7.3, a 3D model of is shown in comparison to the recently certified GE9x and the Rolls Royce UltraFan technology demonstrator.

Figure 7.3: Modern industrial low-speed composite fans and Open Test Case ECL5/CATANA (**a**) **GE9x** (certified 2020, 16 comp. blades, Ø 340cm). (**b**) **Rolls Royce UltraFan** (18 comp. blades / Ø est. 355 cm) (**c**) **ECL5** (16 comp. blades, Ø 50cm)

7.2 Aerodynamic Characteristics

Stage characteristics of steady RANS calculations, throttled via static pressure at the stage outled are presented in Figure 7.4. It can be seen that overall peak efficiency is located at the 100% speedline at a point where the total pressure characteristic is almost flat. For high speedlines above 100% of design speed, choke occurs in the rotor, otherwise it occurs in the OGV. Towards low mass-flow ratio the speedlines are rolled over (positive slope) and limited by numerical convergence. This is comparable to the case presented by Rodrigues et al. (2021), which has shown that through application of a choked nozzle far downstream the numerical stability limit can be further extended but still not reaching the stability limit of the experiment. At highly throttled conditions the performance in experiments significantly deviates from numerical results.

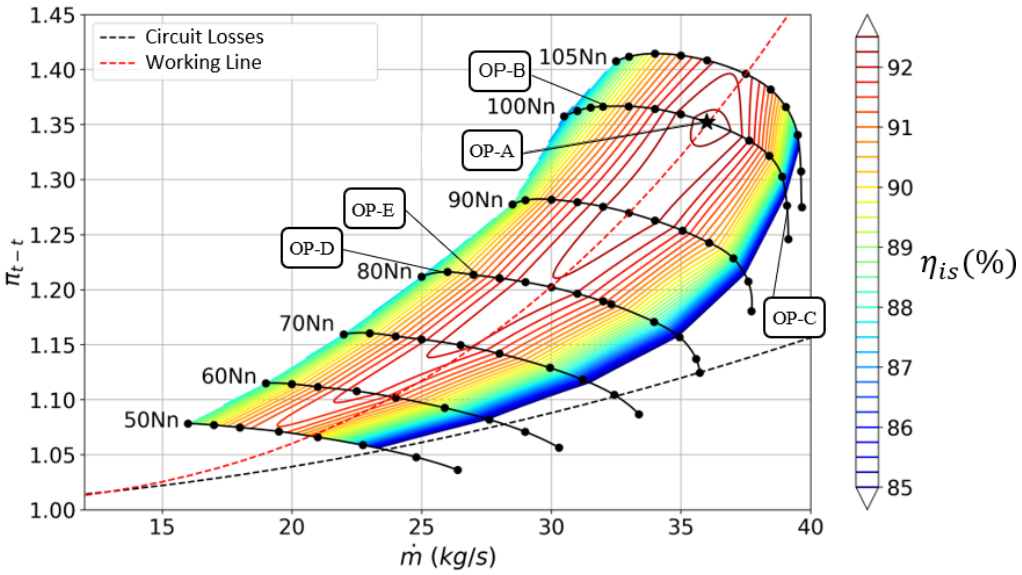

Figure 7.4: Compressor map with stability points of interest

A detail of the 100% speedline is given in Figure 7.5, showing pressure and efficiency characteristics as well as radial profiles at rotor exit. In a wide range between 32 and 38.9 kg/s (representing 19% of design mass flow, depicted green in Figure 7.5) the fan produces a flat efficiency characteristic above 88%. The evolution between the lowly throttled operating point OP-C and the higher throttled conditions shows that the rotor is barely affected between hub and midspan. The maximum pressure ratio is observed near midspan and throttling increases loading of the blade tip. At Design Point OP-A, the efficiency profile is almost constant between 20% and 80% span. Influence of tip-leakage flow is observed between 85% and 100% span for all shown conditions.

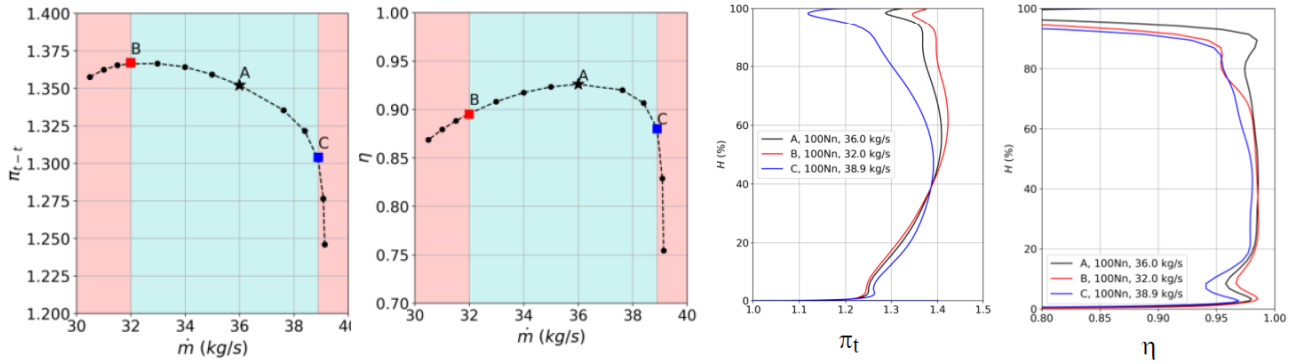

a) stage total pressure characteristic 100%

b) stage isentropic efficiency characteristic 100%

c) rotor exit profiles of total pressure

d) rotor exit profiles of isentropic efficiency

Figure 7.5: Detail of flow conditions at different operating points

7.3 Structural Characteristics

The fan needs to satisfy the aerodynamic specifications while assuring structural safety over the investigation range. Engine-Order crossings with blade and assembly modes need to be sufficiently separated from investigation speedlines.

Concerning synchronous excitation phenomena, intake distortions are the predominant sources Benichou et al. (2019). The potential effects of the OGV are negligible because of the axial distance from the fan, of more than one chord. Experience on similar configurations (Brandstetter et al. (2019c) and Rodrigues et al. (2021)) shows that above the 6^{th} engine order, forced response amplitudes are negligible. At 105% of nominal rotation speed, the 6^{th} engine order frequency is $1155Hz$. Mode 3 and Mode 4 frequencies are respectively around $900Hz$ and $1500Hz$ at maximal rotation speed so only the first three modes are considered in the following.

Mode shapes at ND2 are shown in Figure 7.6. ND2 is representative of all nodal diameters except ND1. In (Pages et al., 2021) we present differences of the Mode shapes for ND1 which can be attributed to a large contribution of the disk. Mode 1 is a bending mode with very low torsional component. The displacement is almost only circumferential without axial component. Mode 2 shows a pronounced torsional component at the blade tip which is known to be critical for fluid-structure interactions (Stapelfeldt and Brandstetter, 2020). Mode 3 represents a torsional mode with torsional center positioned at half-chord at midspan and at the leading edge at the tip.

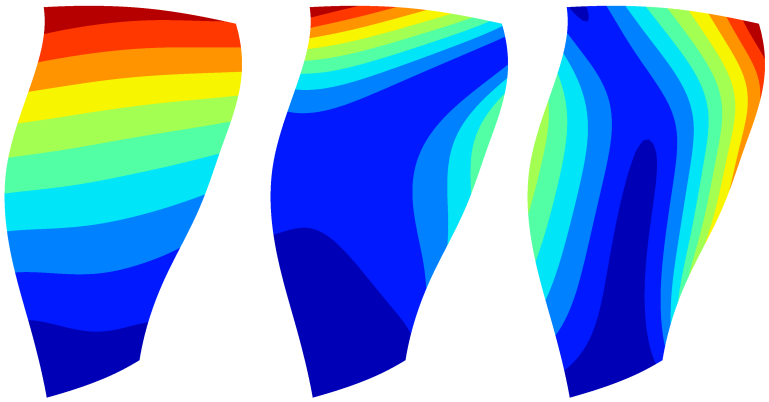

Figure 7.6: Normalized modal displacement amplitude at ND2 (**a**) Mode 1 (**b**) Mode 2 (**c**) Mode 3

The campbell diagram obtained of the fan is presented in Figure 7.7. The crossings of the different modes are highlighted. These are sufficiently distributed in frequency to enable tests at low part-speed (50%), high part-speed (80%) and full speed (100% and above). Experience shows that the measured frequencies on manufactured blades are systematically slightly lower than those predicted. For torsional modes, experience with fans produced by the same manufacturer (Brandstetter et al., 2019c; Rodrigues et al., 2021) indicates that the actual frequencies are nearly 5% lower than predicted. Moreover, in previous experimental campaigns, crossing with engines orders higher than 3 never prevented speedline exploration. Hence, the 80% speedline can be safely investigated if the frequency of Mode 3 will be slightly lower than predicted.

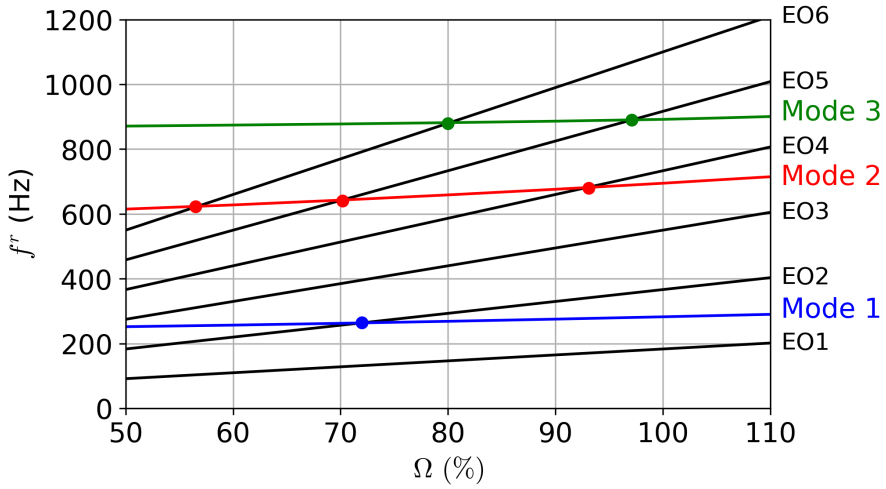

Figure 7.7: Campbell diagram at ND2

The blades of ECL5 are exclusively made of unidirectional carbon fibres and epoxy composite plies stacked into a laminate with intentional ply orientations, which were introduced in (Pages et al., 2021). At the time of manuscript preparation, the fabrication of the first blade prototypes, shown in Fig. 7.8 was completed. In the project manufacturing procedures and layer orientation are systematically investigated. Therefore, established procedures of the industrial partner Safran Aircraft Engines are applied. This concerns the methods of calculating static and dynamic structural deformations, treatments of interfaces, applications of material laws and guidelines for mode separations.

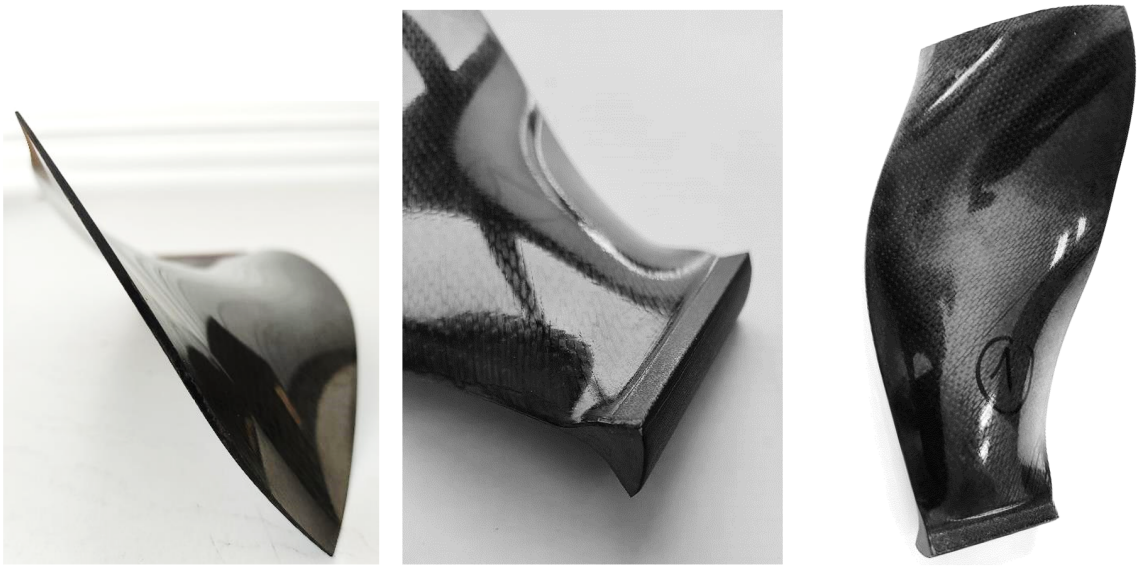

Figure 7.8: Prototype Blade of ECL5 open-test-case, fabricated from carbon fibre composite

The aeroelastic fan stability was systematically investigated over representative operating points with a time-linearized method (Pages et al., 2021). At nominal speed, no aeroelastic instabilities were detected. Thus it will be possible to investigate highly loaded operating conditions. At part-speed, a potential zone where NSV may occur was identified in the simulations. It was shown that the instability area remains located far from the operating line and will be in the focus of the planned experimental campaign which will be described in section 9.

Chapter 8

Summary of Contributions

As laid out in the previous sections, the research of the author focussed on aerodynamic and aeroelastic phenomena which limit the operating range of compressors and fans. As a result of this research, which relied on the support of doctoral students, fellow researchers and technical staff as well as external collaborators, aeromechanical and aeroacoustic mechanisms causing non-synchronous vibrations were identified and explained. This enabled a new classification of phenomena according to their underlying physical mechanisms. The main contributions are summarized in the following:

Convected vorticity disturbances, in interaction with blade vibrations

- For the first time, the direct measurement of pre-stall vortical disturbances, traveling around the circumference in the leading edge plane was realized using phase locked PIV in a high-speed compressor. Furthermore, a robust method to detect the propagation speed of randomly distributed disturbances was introduced (Brandstetter et al., 2018).
- It was proven, that erratic vortical disturbances propagate at constant speed, excite blade vibrations and eventually lock-in with assembly vibration patterns (Nodal Diameter), leading to extensive Non-Synchronous Vibrations (Brandstetter et al., 2018).
- A clear correlation between vibration phase and local flow patterns near the leading edge was derived through coherent analysis of tip-timing data, strain-gauge measurements and PIV (Brandstetter and Schiffer, 2017)
- The same phenomenon responsible for Non-synchronous Vibrations in high-pressure compressors was identified in a low-speed fan fabricated from composite materials. It was demonstrated that despite discrepancies concering performance prediction at throttled operating conditions, URANS methods are capable of predicing the propagation speed of vortical disturbances (Rodrigues et al., 2021).
- It was shown, that acoustic disturbances, resulting from assembly vibration can be clearly identified and separated from freely convecting disturbances using multi-sensor correlation. Furthermore, a method to determine disturbance decay, which was identified as the dominant factor influencing NSV, was introduced, and used to demonstrate that the established interpretation of so-called "Rotating Instabilities" must be revisited. (Brandstetter et al., 2021a)
- A semi-analytic model was build in cooperation with S. Stapelfeldt from Imperial College, using a combination of the experimental results and weakly-coupled URANS simulations to predict the onset of Non-Synchronous Vibrations due to convected disturbances. The model was validated for an HP-compressor and helped to clarify the lock-in mechanism responsible for NSV (Stapelfeldt and Brandstetter, 2020)
- The time marching model for NSV was linearized to perform stability analysis in the frequency-domain, demonstrating that the decay rate of convected disturbances is the dominant factor for system stability. It was shown, that specific aeroelastic parameters are independent from the respective machine, and that the model is generally applicable (Brandstetter and Stapelfeldt, 2021)
- A method to adapt the NSV-model to incorporate aerodynamic and structural mistuning was introduced and used to analyse the effect of different intentional or random geometric variations to suppress NSV. This method can be used to design an optimal mistuning pattern based on individual measurements of blade eigenfrequencies. (Stapelfeldt and Brandstetter, 2021)
- It was shown, that acoustic disturbances, resulting from assembly vibration can be clearly identified and separated from freely convecting disturbances using multi-sensor correlation. Furthermore, a method to determine disturbance decay, which was identified as the dominant factor

influencing NSV, was introduced, and used to demonstrate that the established interpretation of so-called "Rotating Instabilities" (RI) must be revisited. It was found that convected disturbances travel at constant speed independent of their spatial distribution and decay slowly at throttled conditions. If aero-mechanical interaction with blade vibrations occurs (lock-in), convections speed and spectral signatures are altered. Based on this interpretation, the typical RI-spectra can be fully explained without the necessity of disturbances with characteristic frequencies (Brandstetter et al., 2021a)

Acoustic modes, in interaction with blade vibration

- On a novel test facility for transonic fans, the role of the exhaust geometry on the onset of planar acoustic modes was identified. It was shown, that an asymmetric response of the aerodynamic flow field in the fan is in resonance with a dominant, low-frequency acoustic mode, occurring before rotating stall. Geometric variations of the composite blades were identified as influential on the dynamic untwist behavior responsible for the asymmetric aerodynamic field (Brandstetter et al., 2019c).
- Using the methods developed for the classification of convected disturbances, the characteristics of trapped acoustic modes in different multi-stage compressors was enabled. It was shown, how under certain conditions non-synchronous forced response may occur (Brandstetter et al., 2019b; Fiquet et al., 2021a).
- The source of the acoustic modes, developing in a highly mismatched multi-stage compressor was analysed using full annulus URANS simulations, clearly identifying unstable boundary layers in a downstream rotor to lock-in with upstream propagating pressure waves (Fiquet et al., 2019, 2021a,b).
- It was demonstrated, that signatures of aerodynamic disturbances in pressure spectra are strongly affected by the lock-in mechanism of convective and acoustic modes, and established methods to determine disturbance characteristics are misleading. Through multi-physical instrumentation and the method to determine disturbance propagation speeds, a clear identification of the physical phenomena behind spectral peaks in pressure spectra could be derived. (Brandstetter et al., 2021a)

Establishment of an open-test-case fan

- Based on preceding works at ECL a fan module made from carbon fibre composite was designed and established as test case for open research and is fabricated at the time of manuscript preparation. Numerical results indicate aerodynamic performance exceeding state-of-the-art industrial designs (Brandstetter et al., 2019a, 2021b; Pages et al., 2021)

Differentiation of physical phenomena The procedure lined out in this manuscript to determine propagation speeds of disturbances allows the clear determination and identification of the physical mechanisms behind pressure spectra. In modern turbomachines, multiple effects must be considered, including convective, acoustic, and aeromechanically interacting phenomena. For all non-synchronous phenomena discussed in this manuscript, the author proposes to consider the following differentiation in future works, which can be clearly determined according to the described procedures:

- freely convecting vortical disturbances (also formerly described as "Rotating Instabilities"), differentiated from propagating rotating stall cells (part-span, full-span, single- or multi-cell)
- lock-in of convected disturbances with blade vibration patterns (NSV), differentiated from flutter (purely self-excited vibration)
- acoustic duct modes, differentiated into planar or swirling modes, resulting from either acoustic resonance (cut-on/cut-off, trapped modes) or signatures of structural vibration
- non-synchronous forced response (due to rotating stall or acoustic duct modes)

Chapter 9

Future research plan

9.1 Motivation for future research

Throughout all experimental contributions described in this manuscript, the author demonstrated that synchronized multi-physical instrumentation is necessary to purposefully analyze coupled phenomena and instability mechanisms in turbomachinery. In different cases, advanced and customized measurement methods were applied, requiring extensive development efforts, from conception to post-processing. However, highly resolved optical methods near oscillating boundaries still remain challenging and will require further research, independent of the application. The ambition of the turbomachinery group at ECL is to advance in this direction with combined high-speed aerodynamic, structural and acoustic instrumentations in rotating and non-rotating experimental configurations.

Experimental efforts directed at explaining instability mechanisms have mostly relied on on so-called engine representative tests, which include all relevant physics. As accessibility and instrumentation in high-speed turbomachinery are limited, and experiments are typically costly and safety critical, the scientific depth they reach is inevitably restricted (Fiquet et al., 2019). The research initiative on the open-test-case fan ECL5 (Section 7), aims to provide a dataset with increased detail for integrated systems, but it will remain challenging to separate individual physical mechanisms, as vibrations cannot be controlled directly. The alternative to those engine representative experiments are highly simplified studies with controlled vibration but reduced complexity, typically not representative for flow conditions relevant for the dominant aeroelastic problems in turbomachinery. Examples of this include stationary cascades with low aerodynamic loading, subsonic profile shapes, and low reduced frequencies (Hill et al., 2021; Malzacher et al., 2019; Livva et al., 1968).

Hence, the envisaged research strategy aims to achieve a more fundamental understanding of aeroelastic mechanisms and improve prediction methods by working on the whole spectrum of experimental complexity: performing **engine representative studies** on rotating geometries with a high similarity to high-speed applications as well as fundamental studies on non-rotating, **vibrating blade profiles, either isolated or in cascade arrangement** but at relevant flow conditions, particularly involving flow separations. Combined with extensive instrumentation, insights into the characteristics of unsteady flow structures in vicinity of controlled oscillating profiles are expected to be of great value for future method development.

For the engine representative studies, the facilities at ECL and the development of an open test case fan are predestined for deep studies on all types of coupled aeroelastics in modern fan architectures. In section 9.2, the ambition to generate a multi-physical benchmark dataset based on a systematic parameter variation will be laid out. This will deliver results which can be used to develop semi-analytical methods, such as the model for Non-Synchronous-Vibration described in Section 4.3. The existing model is capable of identifying critical vibration patterns, but the prediction of amplitudes, particularly involving aerodynamic and structural non-linearities requires further research. This is particularly important, as studies on different types of composite low-speed fans (Rodrigues et al., 2021) indicate that system-asymmetry and limit-cycle oscillations due to aero-mechanical interactions will be inevitable in a wide range of the operating range of future designs. To develop an improved understanding and prediction methodologies, it is intended to further strengthen cooperations with our partner institutions, Imperial College, VKI and ONERA on integrated numerical/experimental campaigns on open-source geometries. The anticipated outcomes from project CATANA will be a significant milestone for these collaborative efforts towards open-science in turbomachinery aeroelasticity.

On a more fundamental level, the proposed research strategy aims to improve the understanding of complex flow structures around deforming rotor blades and their physical coupling mechanisms

with surrounding structures, as this is the origin of all types of aeroelastic instabilities. This could be enabled through research on unsteady aerodynamics of oscillating aerofoils, isolated or in cascade environments, using advanced experimental and numerical methods to develop physics-based prediction models. The resulting experimental data base can also be used to advance high fidelity numerical methods, are of great relevance for the design and analysis of future experiments but out of scope of the present manuscript.

These two research streams serve the long term ambition to enable intentional aeroelastic design, considering fluid-structural interactions less as a problem to mitigate but a means to improve technology. One example of advantageous fluid-structure interaction is the intentional exploitation of untwist of fan blades to improve part-speed efficiency. To this end, advancements in composite materials which allow anisotropic blade design could synergize with more accurate prediction methods for aeroelasticity. The following will describe the two research streams in more detail, define the research questions and outline the research plan.

9.2 Engine Representative Studies / Aeroelastics of Low Speed Fans

9.2.1 State of the Art / Arising Challenges

The main objective to increase propulsive efficiency in future engines is the augmentation of bypass-flow, either in ducted turbofans or in form of configurations with open-rotors. Due to significant technological challenges, the highly promising open-rotor concept is still not ready for application, today. ECL is participating in fundamental research initiatives on the advancement of open-rotor technology but significant impact is currently necessary on ducted architectures for the near future with far increased bypass mass flow. Enormous advancements can be achieved by employing low-speed fans which are connected with the turbine via a gearbox (Geared-Turbofan with Ultra-High-Bypass-Ratio (UHBR)). The potential of this technology is widely accepted in international aeronautical research for the past three decades. Merely insufficient technological possibilities impeded the successful establishment which requires rigorous application of advanced design, material and manufacturing methodologies, particularly lightweight composite structures. Consequent application of composite rotors enables disruptive design possibilities but demands for a fundamental understanding of the dynamic behaviour to ensure robust design and safe operation. Using modern fabrication technologies it is possible today to create lightweight carbon-fibre fan blades that allow additional design parameters and are structure-dynamically superior to advanced metallic components. This results from the intentional use of the anisotropic character of composite layers, enabling the purposeful placement and shaping of blade eigenmodes, allowing controlled structural damping and mistuning while reducing the weight compared to metallic blades. It is possible to aerodynamically use the tendency of the blades to untwist with rising rotor speed. Yet, the dynamic behaviour of composite blades is by far not sufficiently understood to fully exploit the potential.

The sensitivity to multi-physical resonance between aerodynamic, structure-dynamic and acoustic phenomena is amplified in modern rotor designs. Very thin blades, which are required to maintain high efficiency at transonic flow conditions, are flexible and prone to vibrations. As a result, aeroelastic and aeroacoustic problems increasingly set the stability limit for modern compressors and fans. Shorter engine intakes are essentially required to fully exploit UHBR concepts, resulting in stronger inlet distortions that can interact with the rotor and lead to safety critical conditions . The shorter intakes have different acoustic properties, amplify aeroacoustic interactions with the fan and reduce the possibility to attenuate noise emissions. Consequently, crucial design parameters from conventional engines with metallic rotors, longer intakes and higher rotation speed cannot be directly transferred.

9.2.2 Investigations planned in project CATANA

The fundamental knowledge gaps concerning these points currently prevent a robust prediction of instability. It is required to entirely understand the described physical interdependency between three dimensional aerodynamic flow structures, structural vibrations and acoustic modes, comprising all phenomena described in this manuscript. Project CATANA aims to close the following gaps for modern low-speed composite fans:

- The coupling mechanisms between aerodynamics, aeroacoustics and aeroelastics are still not sufficiently understood.
- The sensitivity of the coupling towards geometrical and structure-dynamic properties and asymmetry is not understood, particularly the role of structural damping and mistuning.

Thus, it is necessary to clearly identify, characterize and quantify the respective mechanism that limits the operating range, from part-speed to overspeed and from highly-loaded to unloaded operating conditions on a test case, representative for modern composite designs. Dynamic characteristics of propagating and non-propagating aerodynamic structures must be determined, particularly those of unstable phenomena like local flow separation zones. They need to be analysed towards coherence with external feedback mechanisms, both structural (blade or assembly vibrations) and acoustic (intake and exhaust, inter-blade reflections, rotor-stator interactions). Finally, sensitivity parameters like geometric, aerodynamic and structure-dynamic asymmetry and damping must be identified and quantitatively analysed concerning their influence on the critical coupling phenomena. These objectives present the core of the research program.

To achieve these goals a comprehensive approach is conducted in project CATANA under coordination of the author. Using the test case ECL5 described in Chapter 7, a detailed investigation of coupled instabilities is planned based on synchronized instrumentation, capable to physically characterize and quantify the coupled phenomena. It is intended to generate a substantial database at all limits of the operation map of a composite fan stage, reaching from NSV, subsonic and transonic stall flutter during highly-loaded operation until blockage flutter at unloaded transonic conditions. Particularly the fundamental parameters expected to influence the instability mechanisms: a) structural asymmetry and b) intake geometry need to be strategically analyzed to quantify the sensitivity with the goal to understand the relevant coupling phenomena and to enable more predictive simulation methods.

The ECL project to develop design methods for a low-speed transonic composite fan stage has led to a promising research configuration that has recently been opened to the aeroelastic community. Even though it is a purely academic development that can be openly shared, the design has been consequently analysed and validated by the industry partner Safran Aero Engines to confirm safe operation. With the available knowledge and methods, it is anticipated to strategically characterize and quantify multi-physical coupling with unprecedented resolution for composite fans.

In the following section, the planned parameter variation and the experimental strategy to investigate the fan stage ECL5 are presented. Based on current knowledge, dominant factors influencing non-synchronous instability mechanisms are the system symmetry and the intake geometry.

Rotor symmetry and mistuning It is known that aerodynamic and structural mistuning of a rotor can be very efficient to suppress or attenuate the development of propagating phenomena, both structurally and aerodynamically. State-of-the-art fabrication procedures for composite blades typically result in a more significant unintentional spreading of structural properties, particularly concerning mode-shapes and eigenfrequencies. Depending on the scale and the composite concept (layers, waeve, etc.) natural frequencies of the most relevant first modes can deviate in the order of one percent. It is planned to fabricate two specific configurations, a) one symmetric configuration consisting of the blades with the lowest deviation from the design and b) a mistuned configuration that will be assembled in a specific pattern intentionally to attenuate propagating modes. With these two configurations - investigated sequentially - it is possible to explore the impact of asymmetry without altering the aerodynamic design geometry.

Intake geometry Investigations from the past have shown that the intake length and geometry significantly influences the development of aeroacoustic interactions with the fan and can lead to flutter. The typically used experimental intakes are longer than a real engine intake to enable more accurate performance measurements. This results in shifted acoustic resonance frequencies and can attenuate the tendency to develop flutter. To strategically analyse the influence it is planned to investigate one rotor configuration in direct comparison between two intake geometries, a) a standard performance-test-intake (airmeter) and b) an engine-like shortened intake that is representative of a low-speed fan application.

Planned experimental campaign

For each of the described initiatives, a sequential investigation strategy is envisaged:

• In a first step, the structure of the manufactured rotor-blades will be characterized to ensure geometric similarity and structural integrity: Tomographic analysis of material inhomogeneity, 3D-Scan, surface roughness, mode shapes, dynamic spectra from non-rotating shaker test

• The respective rotor will be assembled, instrumented with strain gauges, balanced and integrated in the facility PHARE-2 (ECL-B3) for the main investigations (flow campaign). Using synchronized instrumentation for aerodynamics, structure dynamics and acoustics the steady operating map and the instability behaviour at all limits are explored.

• After the main measurement campaigns, piezo-excitation patches will be applied to individual blades and the rotor integrated in the PHARE-1 facility of LTDS to characterize the exact structure-dynamic properties including structure damping at realistic rotation conditions under vacuum (structure-campaign).

In order to derive a phenomenological structure of the instability mechanisms, reproducible tests of the highly coupled system with actively controlled steady and transient boundary conditions are required. Within the measurement campaigns, scientifically interesting operating points need to be identified and investigated repeatedly to achieve statistical significance. By application of multi-physical simultaneous instrumentation, a comprehensive image of the occurring phenomena can then be derived using advanced evaluation methods. The measurement objectives can be separated into a characterization of periodic or stochastic phenomena at steady operating points and transient investigations of instability mechanisms. At multiple investigation speeds several operating points from unloaded to loaded conditions are planned to be investigated thoroughly towards aerodynamic, acoustic and structural phenomena and their interactions. The derived database including detailed measurements of stage performance and emitted noise will be necessary to calibrate and validate numerical models. Transient investigations at the limits of the stable operating range (Fig. 9.1) are planned to identify and characterize the respective instability mechanisms. It is intended to perform repeated throttling manoeuvres as well as transient accelerations close to the instability limit.

The research focus of the transient investigations will be on the respective instability mechanisms since those are the most complicated and safety critical phenomena. As depicted in Fig. 9.1, it is expected for the stage to encounter non-synchronous effects at highly loaded conditions, which are typically dominated by convective disturbances leading to NSV but can be sustained by acoustic interactions with the intake (Pages et al., 2021). At overspeed or unloaded conditions acoustic phenomena are expected to dominate the instability process (supersonic/choke flutter, Rendu et al. (2020). Here, the main scientific interest lies in the accurate characterization of the interaction between the shock and the boundary layer which is still very hard to predict in numerical simulations, particularly if the structure is not rigid. The planned multi-physical instrumentation is expected to give a deeper insight into the physical processes and to allow the validation of advanced simulation approaches.

The planned experiments on rotor asymmetry and intake geometry will most probably affect the limits of the stable operating range. It is expected that structural mistuning has a strong influence on the stability and efficiency at unloaded conditions; the intake geometry is assumed to affect the stall / stall-flutter limit. For these points, the knowledge gaps are still enormous whereupon no clear prediction can be given even though the fundamental understanding is of great importance for future turbomachinery designs.

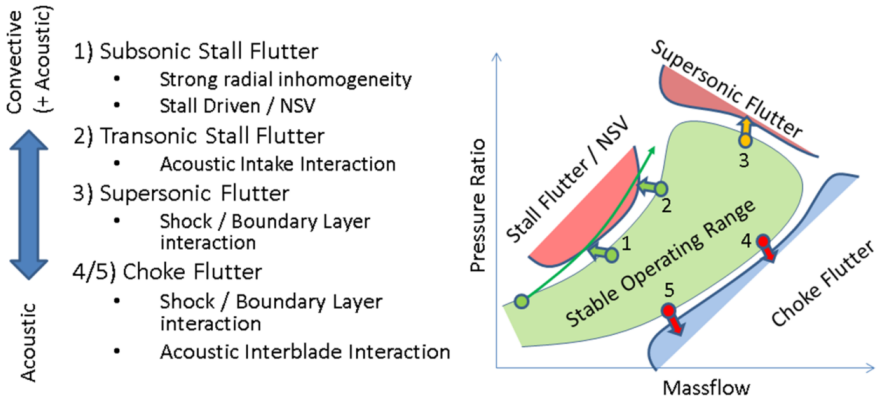

Figure 9.1: Anticipated non-synchronous instability mechanisms depending on operating condition

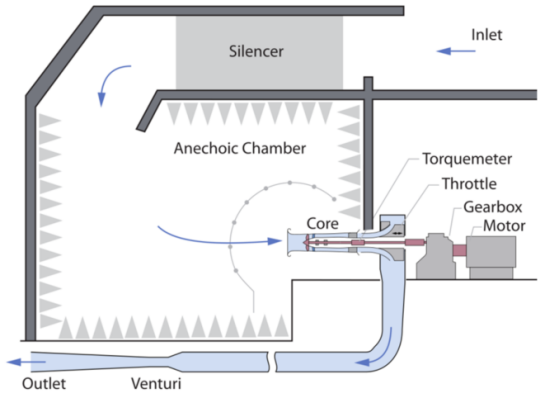

(a) Section of test facility ECL-B3

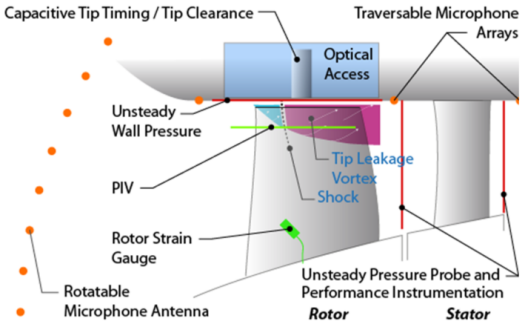

(b) Multi-physical instrumentation in the rotor section

Figure 9.2: Main instrumentation for fan stage investigation

Experimental Facility and Instrumentation Concept

Specifically designed for this purpose, the fan-test facility PHARE-2 (ECL-B3) with transient control mechanisms and accurate measurement systems for steady performance has been realized in a close cooperation between Ecole Centrale de Lyon and Safran Aircraft Engines as part of the ANR – EQUIPEX program (Brandstetter et al., 2019a). The facility, presented in Fig. 9.2) has been commissioned in 2017 and successfully used to for the investigation of a state-of-the-art fan stage. It currently contains a technology demonstrator for a modern UHBR Fan that is investigated within the European funded project ENOVAL (GA: 604999). The core section is embedded in an anechoic chamber, supplemented by a flow path, intentionally designed to minimize acoustic disturbances. The rotor is electrically driven and throttled to facilitate flexible operation, which is necessary to achieve reproducible transient conditions. The machine and test rig are instrumented with more than 600 sensors (pressure, temperature, vibrations) which will provide not only the global performance of the fan stage but also space- and time-resolved data. In addition to one hundred microphones implanted on the casing of the machine, an acoustic antenna with 19 microphones is installed in the anechoic chamber and will be rotated around the air intake of the machine in order to characterize the emitted noise (far field measurements and source localization).

To enhance the understanding concerning transient processes it is intended to significantly extend the instrumentation and evaluation methods. Independent and synchronized unsteady instrumentations as illustrated in Fig. 9.2b) will be integrated in the core section.

The intended instrumentation encompasses the following methods:

Measurement of aerodynamic phenomena in the rotor section

• Laser-Doppler-Velocimetry (LDV) to resolve the periodic flow field at different channel heights in the rotor (shock and tip-leakage-vortex structure, bladewise asymmetry, local 2-component velocity field).

• Laser-Optical Particle Image Velocimetry (PIV) to resolve the instantaneous velocity 3-Component field in the rotor tip region at approximately 95% Channel height, covering tip-leakage vortex and shock: The application has proven suitable to provide a high spatial resolution during transient maneuvers and allows the identification of time coherent aerodynamic phenomena.

• Unsteady traversable pressure probes to analyze the individual flow field downstream of each rotor blade

• Multichannel unsteady wall pressure measurements with custom miniaturized probes delivers time resolved information on shock structure, blade loading and vortex propagations.

Measurement of structural vibrations

• Rotor blade applied strain gauges with telemetrical data transfer: Time resolved measurement of individual blade movement – detection of non-harmonic movement.

• Capacitive Tip Timing measurement of blade tip deflection from steady reference frame allowing the detection of structural vibration patterns (Nodal Diameter) – time accurate measurement of local tip clearance resolving eccentricity and transient clearance development.

• Optical blade tip detection: The rotor tip deformation will be detected in the PIV images to derive time coherent correlations between flow structure and blade vibration phase.

Measurement of acoustic signatures

• A rotatable microphone antenna upstream of the intake section combined with microphone arrays in the vicinity of the fan stage are used to measure acoustic signatures and propagating waves, particularly cut-on conditions of specific helical modes that can be in coherence with structural vibration patterns.

• Distributed microphones and accelerometers in the exhaust system allow the decomposition of emitted waves and their reflections, specifically low frequent planar modes.

Advanced investigation methods

To achieve the anticipated research objectives a comprehensive combination of the individual measurement systems is anticipated. The proposed concept combines several measurement systems and enables the detection of interactive mechanisms and instability phenomena where individual systems are insufficient. As described, unstable aerodynamic phenomena like local flow separations and interactions between shock and tip leakage vortex or boundary layer are sensitive to external feedback mechanisms, either acoustic or structural. It is absolutely necessary to cover all physical contributions synchronously during transient experiments to clearly characterize the coupling mechanism. The schematic presented in Fig. 9.3 depicts the necessity of the multiple instrumentations to achieve the desired results. The axially and circumferentially distributed pointwise acoustic and aerodynamic measurements are required to detect and quantify propagating modes resulting from aeroacoustic interactions. The additional information from LDV (time resolving) and PIV (high-speed phase locked, synchronized with time resolving systems) will allow a time coherent identification of critical and interacting flow structures in the rotor. In case of structural interaction, the results from rotor tip-timing and strain gauges enables a clear characterization of aeroelastic phenomena, including the quantification of asymmetry and sensitivity parameters. Since both spatial and temporal waveforms and amplitudes (aero/structure/acoustic) as well as the local flow structures can be derived, it is expected to clearly distinguish the respective coupling mechanism at steady operating points and during transient maneuvers.

Supported by the extensive performance instrumentation of the facility that allows the determination and control of the steady operating conditions it will be possible to provide a comprehensive dataset for interdisciplinary method validation.

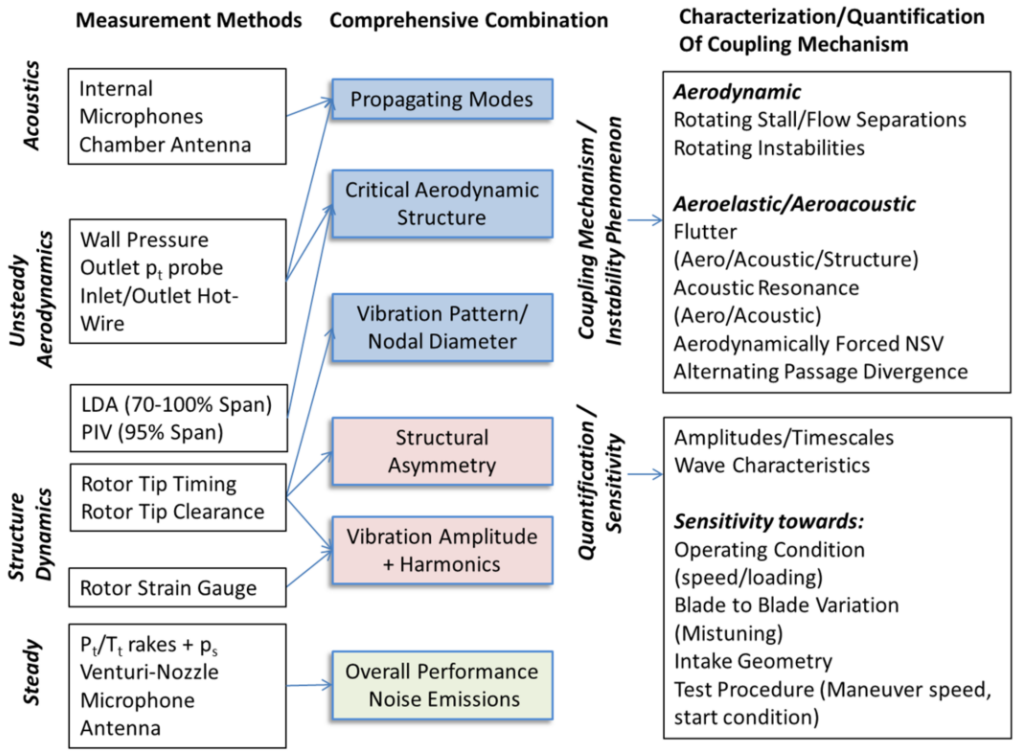

Figure 9.3: Research strategy to combine multi-physical instrumentations

In order to extend the analytical capabilities to characterize interactions and coupling mechanisms as laid out in Fig. 9.3, advanced methodologies will be implemented in the future. Particularly phased POD methods are promising to derive correlations between local flow structures measured with high-speed PIV and blade oscillation, synchronized with acoustic measurements.

As described, the measurements on the open loop fan test facility are expected to uncover the coupled phenomena depending on the flow conditions. It is yet not possible to derive the isolated structural characteristics of the rotor assembly. The structural damping of a specific mode is typically unknown, particularly due to the nonlinear connection between blade and disk but of great importance for the prediction of instability. In order to complete the characterization of the system with this parameter, the assembled fan will be integrated in the vacuum test facility PHARE-1 of LTDS to be analyzed under realistic rotation speed. Piezo-actuators applied to individual blades will be used to excite specific eigenmodes and nodal diameters. Using a laser-optical derotator it is possible to measure the vibration amplitude depending on the excitation and hence the modal damping. In comparison with the dynamic spectra, measured without rotation on a shaker-table, these results will be of great value for the global objective to make the aeroelastic behavior of composite fans more predictable.

The enormous experimental effort is justified by the exploitation of synergies resulting from the synchronized application of different complementary measurement systems. The envisaged entirety of multi-physical systems is unprecedented and particularly the customization and synchronization very demanding. The implementation strongly depends on optimal functional interaction of facility and instrumentation and operation of the test rig at safety critical conditions. Because of the associated risk of failure, the lack of concentrated expertise and the immaturity of experimental methods, such comprehensive investigations have not been performed in the past. However, they are crucial for future advancements for the reasons outlined above.

9.3 Fundamental Studies

The fundamental research aims to improve the physical understanding of the unsteady aerodynamics of vibrating blades and coupling mechanisms with the system. The author's previous research on NSV indicates that this approach is conducive to developing fast prediction methods: In (Stapelfeldt and Brandstetter, 2020), the authors demonstrated that it is possible to separate the blade aerodynamics from the rotor and wider system. In (Brandstetter and Stapelfeldt, 2021) we demonstrated that different blade designs share common aeroelastic characteristics and that prediction method developed on a particular machine can be of general applicability.

The NSV model still relies on several assumptions. It uses constant coefficients to correlate blade oscillation with the generation of disturbances and vice versa. Results presented in (Stapelfeldt and Brandstetter, 2020) already indicated that for high oscillation amplitudes, aerodynamic saturation causes non-linear behaviour, particularly, if the blade-boundary layer separates. For isolated aerofoils, extensive studies are reported in literature under the theme of dynamic stall have investigated this non-linear behaviour and developed semi-empirical methods for unsteady aerodynamic response (Cimarelli et al., 2021).

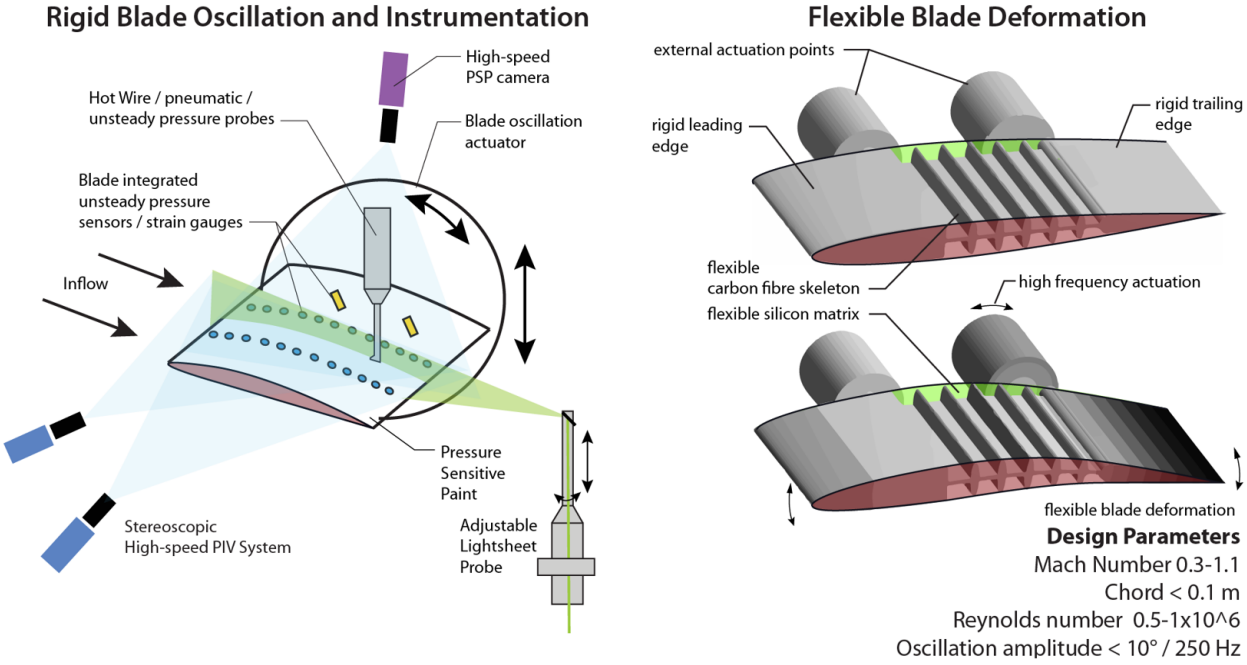

Figure 9.4: Planned experimental study on isolated, oscillating airfoils

Research on dynamic stall has demonstrated the value of high-fidelity aerodynamic investigations and of the use of semi-empirical models to predict unsteady aerodynamic loads under prescribed (modal) deformations. While the fundamental ideas and analysis methods from dynamic stall research are transferable, specific findings such as aerodynamic coefficients are not. In turbines, compressors and propellers, the aerodynamics are further complicated by the presence of neighbouring blades. Semi-empirical models will therefore need to account for complex steady flow structures (tip vortices, end-wall effects) as well as the influence of adjacent blades on aerodynamic coefficients. The inclusion of these effects, range of geometries across applications, as well as the flow regimes (high Mach and/or high Reynolds numbers) present a huge challenge which need to be overcome.

It is intended to increase the research efforts of the turbomachinery group with specifically designed experiments on isolated blades and cascade arrangements with controlled blade oscillation. The principal purpose of experiments is to resolve the aerodynamic flow structure and the associated forces around oscillating blades.

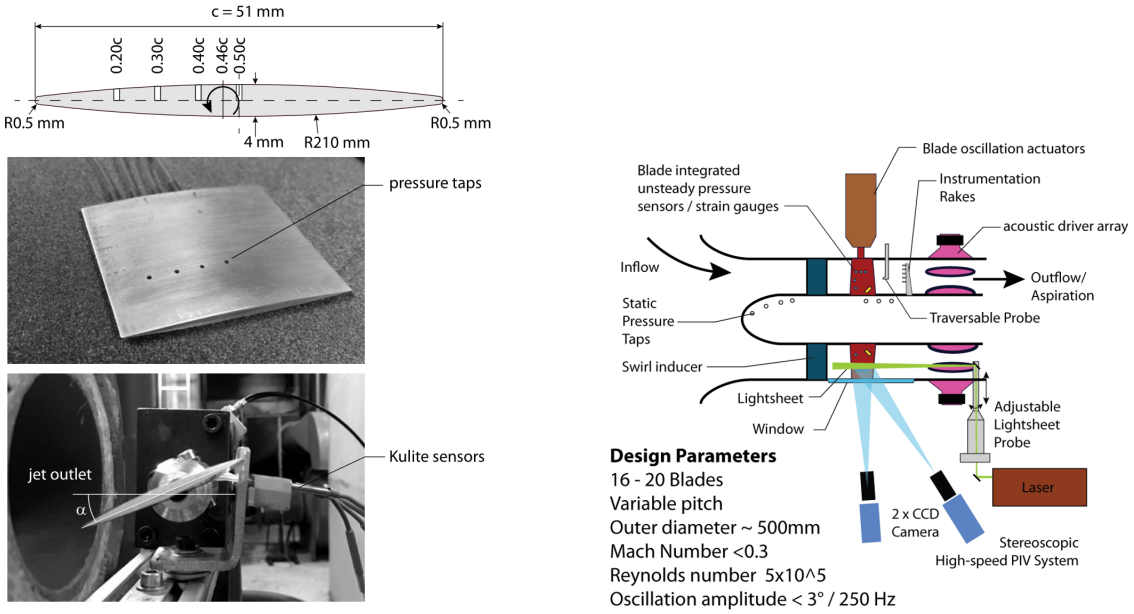

(a) Preliminary study on oscillating airfoil

(b) Planned annular blade cascade setup

Figure 9.5: Fundamental studies

This must be done on different levels of system complexity, which is extremely challenging for a number of reasons:

- Blade vibration is not limited to rigid oscillation, but high-frequency flexible deformation
- Highly time-resolved, synchronized measurements for aerodynamics, structural vibration and acoustics are necessary in spatially confined, and significantly vibrating environments.
- Relevant flow conditions comprise compressible regimes (transonic Mach-Numbers), and associated limitations concerning instrumentation access, safety measures and experimental costs.

The proposed research envisages studies on single aerofoils, undergoing prescribed rigid body and flexible blade deformation, as illustrated in Fig. 9.4. Feasibility-studies have been successfully conducted at ECL (Mattis, 2019), employing high-performant actuators capable of oscillating blades of the relevant size with significant amplitude (250Hz, $\pm 10°$), depicted in Fig. 9.5a.

In parallel to the single aerofoil study, an experiment will be set up to investigate the aeroelastic behaviour of selected profiles in an annular cascade, which enables the characterization of rotor system effects. This configuration provides an additional level of complexity and parameters which influence the local aerodynamic flow structure as well as physical coupling with neighbouring blades and the acoustic duct. The experiment will be designed to trigger sensitive and responsive flow structures, particularly detached boundary layers (Fiquet et al., 2021a) and controlled 3D-features such as radial migration governed by an upstream swirl generator, which will be the first time in a cascade.

Using multi-physical instrumentation, the characteristics of these flow structures will be investigated in the context of blade vibration. In the experiments, the vibration of individual blades is controlled via an external actuation system to generate single and travelling wave vibrations. In addition, the effect of trapped acoustic duct modes, generated with an annular array of high-performant acoustic drivers, will be investigated. This setup is novel in terms of aeroelastic cascade investigations, as it allows to provoke a specific type of disturbance propagation and directly measure the response of the local flow field. The module will be designed according to preliminary studies for a range of aerodynamic conditions which allow acoustic modes to be trapped in the machine, with axial Mach-numbers of approximately 0.3. The scale of the module will be chosen to allow for a maximum of instrumentation detail and enabling a systematic variation of aerodynamic profiles. The results are anticipated to reveal fundamental details on the characteristics of flow separations in blade passages

which are in resonance with blade vibrations, circumferential disturbance convection or acoustic duct modes. As described in this manuscript, these types of interactions are known to be the most safety critical for several types of ducted turbomachinery and validation datasets are highly necessary.

For both the isolated aerofoil and cascade studies, a very detailed instrumentation as depicted in Fig. 9.4 and Fig. 9.5b will be necessary to achieve the desired resolution of unsteady flow features. For aerodynamic measurements high-performance unsteady instrumentation will be integrated, including high-speed stereoscopic PIV, pressure sensitive paint, unsteady pressure sensor (microphone) arrays and traverses of pneumatic and hot-wire probes at various span and chord positions, all synchronized with vibration and acoustic measurements.

For both studies, intensive collaborations with partner institutes will be necessary.

9.4 Collaborations

For the past four years, the author has been involved in several collaborations between research groups at Ecole Centrale de Lyon, centered around the multi-physical investigation at the test facility PHARE. In project CATANA, the turbomachinery research group as well as the acoustic group of LMFA are participating in collaboration with the LTDS, which is responsible for structural measurements. This internal collaboration is complemented in a partnership with the VKI in Brussels, providing expertise on unsteady instrumentation. The proposed research strategy will help to sustain the position of the institute in the academic sector and complement the strong ties to the industrial partners of Groupe SAFRAN.

In the field of high-speed turbomachinery it is necessary to rely on strong industrial support to provide the safety-critical technology. Particularly the research on engine-representative geometries will build on the author's experience and expertise with various industrial partners (Rolls-Royce Germany/plc 2007-2017, MTU 2007-2013, Alstom 2009, Siemens 2010-2017, Safran AE/HE/TECH since 2017), to arrange strategic, interdisciplinary research campaigns.

To pursue combined numerical/experimental investigations, such as presented in the works of the PhD-Students A. Fiquet, M. Rodrigues and V. Pages, the strong link between the LMFA and ONERA, who are developing the numerical code used for turbomachinery applications, CERFACS for high-fidelity numerical applications and ISAE/Supaero concerning high off-design operation of turbomachines will be enforced.

The author has furthermore established a close academic collaboration with the aeroelastic group at Imperial College London with the aim to improve the methods to predict complex aeroelastic interactions in turbomachinery. This collaboration has already advanced understanding of convective non-synchronous vibrations and relevant parameters. By continuing the partnership within the proposed research programme, experiments and numerical methods can be used in synergy to prepare and analyse experimental data and develop fundamental understanding of complex aeroelastic phenomena. Concerning further and more general model developments, enhanced interactions with the turbomachinery groups at VKI in Brussels as well as Universidad Politécnica de Madrid are envisaged.

One general aim of the author is to increase research in European-funded projects, either within the application-related programmes of Cleansky, where several applications with academic and industrial partners have been deposed at the time of manuscript preparation or in more fundamentally oriented programs, particularly to enhance involvement in renewable energy turbomachinery.

9.5 Long Term Research Perspective

The multi-physical interactions described in this manuscript are found in many turbomachinery applications, from aviation to renewable energy, and the proposed research strategy can provide benefits to all of them.

In aviation, aeroelastic effects are expected to play an increasingly important role. This has already been discussed for UHBR fans, which are expected to enter service within the next decade, and open rotor architectures which are planned for the 2030s. The knowledge gained and methods developed in the proposed research strategy can contribute to the successful development and implementation of these technologies. They pave the way to multi-disciplinary design optimisation, maximising efficiency and component life, and reduce development risks. This not only aids evolutionary technology changes, such as increasing fan diameters, but also reduces the risk for the introduction of revolutionary technologies. In the short and medium term, it can find application in new technologies for urban air mobility and short-haul electric or hybrid-electric flight. In the longer term, it will benefit new propulsion concepts such as distributed propulsion and boundary-layer ingestion, where even stronger coupling between intake aerodynamics and fan/compressor aeromechanics and aeroacoustics can be expected.

The fundamental research stream can also deliver benefits outside of aerospace. It will investigate complex flow structures around deforming blades and the interaction with the surrounding system. This is relevant for all types of turbomachinery, from gas, wind and tidal turbines to marine and aerospace propulsion, and a profound scientific understanding would therefore have far reaching impact, benefiting renewable energies as well as aviation and marine propulsion. The ambition of the author is to extend the research focus of the turbomachinery group towards renewable energy applications, using and advancing methodologies established for aircraft components. To this end, collaborations with partners at Universität Duisburg-Essen concerning hydro-elastic marine applications and University of Sion for the improvement of vibration measurements in Pelton-turbines have partially been initiated.

In the proposed research program, high-speed turbomachinery is thus used as a technology carrier because of the strong and clear concentration of interaction phenomena. In this field it will be possible in a foreseeable future to exploit the developed methods to create more efficient engines whereas the long term research benefits extend to a much wider field of fluid-engineering, ranging from sustainable transport technologies to renewable energy converters.

REFERENCES

Armstrong, E. and Stevenson, R. (1960). Some practical aspects of compressor blade vibration. *The J. of the Royal Aeronautical Society*, 64(591):117–130.

Baumgartner, M., Kameier, F., and Hourmouziadis, J. (1995). Non-engine order blade vibration in a high pressure compressor. In *Proc. 12th ISABE (International Society for Air Breating Engines)*.

Benichou, E., Dufour, G., Bousquet, Y., Binder, N., Ortolan, A., and Carbonneau, X. (2019). Body force modeling of the aerodynamics of a low-speed fan under distorted inflow. *International J. Turbomach., Propulsion and Power*, 4.

Biela, C., Brandstetter, C., Holzinger, F., and Schiffer, H.-P. (2011). Influence of inlet guide vane wakes on performance and stability of a transonic compressor. In *Proc. 20th ISABE (International Society for Air Breathing Engines)*.

Bontemps, T., Aubert, S., and de Pret, M. (2021). Prediction of the acoustic reflection in a realistic aeroengine intake with three numerical methods to analyze fan flutter. *J. Turbomach.*, 143(10):1–20.

Brandstetter, C. (2015). Aerodynamische stabilisierung transsonischer axialverdichter: Eine experimentelle untersuchung der blattspitzenstroemung unter dem einfluss von gehausestrukturierungen / aerodynamic stability enhancement of transonic axial compressors: Experimental investigation of the blade tip flow with casing treatments. *PhD Thesis, Technische Universitaet Darmstadt, ISBN 978-3-8440-4463-8*.

Brandstetter, C., Biela, C., and Schiffer, H.-P. (2011). Piv measurments in a transonic compressor test rig with variable inlet guide vanes. *American Institute of Aeronautics and Astronautic*.

Brandstetter, C., Juengst, M., and Schiffer, H.-P. (2018). Measurements of radial vortices, spill forward, and vortex breakdown in a transonic compressor. *J. Turbomach.*, 140(6):061004.

Brandstetter, C., Ottavy, X., Paoletti, B., and Stapelfeldt, S. (2020). Interpretation of stall precursor signatures. In *Proc. XXV Biennial Symposium on Measuring Techniques in Turbomachinery*.

Brandstetter, C., Ottavy, X., Paoletti, B., and Stapelfeldt, S. (2021a). Interpretation of stall precursor signatures. *J. Turbomach.*, 143(12):121011.

Brandstetter, C., Pages, V., Duquesne, P., Ottavy, X., Ferrand, P., Aubert, S., and L., B. (2021b). Uhbr open-test-case fan ecl5/catana, part 1 : Geometry and aerodynamic performance. In *Proc. 14th European Conference on Turbomachinery Fluid dynamics and Thermodynamics, ETC2021-626*.

Brandstetter, C., Pages, V., Duquesne, P., Paoletti, B., Aubert, S., and Ottavy, X. (2019a). Project phare-2 : A high-speed uhbr fan test facility for a new open-test case. *J. Turbomach.*, 141(10):101004.

Brandstetter, C., Paoletti, B., and Ottavy, X. (2019b). Acoustic and convective mechanisms contributing to non-synchronous-vibrations in a multistage compressor. In *Proc. ASME. GT2019, Volume 7A: Structures and Dynamics, GT2019-91514*, page V07AT36A019.

Brandstetter, C., Paoletti, B., and Ottavy, X. (2019c). Compressible modal instability onset in an aerodynamically mistuned transonic fan. *J. Turbomach.*, 141(3):031004.

Brandstetter, C. and Schiffer, H.-P. (2017). Piv measurements of the transient flow structure in the tip region of a transonic compressor near stability limit. *J. Glob. Power Propuls. Soc.*, 1:303–316.

Brandstetter, C. and Stapelfeldt, S. (2021). Analysis of a linear model for non-synchronous vibrations near stall. *Int. J. Turbomach., Propulsion and Power*, 6(3):26.

Brandstetter, C., Stapelfeldt, S., Vahdati, M., Holzinger, F., and Schiffer, H.-P. (2016a). Near stall behavior of a transonic compressor rotor with casing treatment. In *Proc. ASME. GT2016, Volume 2D: Turbomachinery, GT2016-56606*, page V02DT44A013.

Brandstetter, C., Wartzek, F., Werner, J., Schiffer, H.-P., and Heinichen, F. (2016b). Unsteady measurements of periodic effects in a transonic compressor with casing treatments. *J. Turbomach.*, 138(5):051007.

Bright, M. M., Qammar, H. K., and Wang, L. (1999). Investigation of pre-stall mode and pip inception in high-speed compressors through the use of correlation integral. *J. Turbomach.*, 121(4):743–750.

Camp, T. R. (1999). A study of acoustic resonance in a low-speed multistage compressor. *J. Turbomach.*, 121(1):36–43.

Camp, T. R. and Day, I. J. (1998). A study of spike and modal stall phenomena in a low-speed axial compressor. *J. Turbomach.*, 120(3):393–401.

Carter, A. and Kilpatrick, D. (1957). Self-excited vibration of axial-flow compressor blades. *Proc. Institution of Mechanical Engineers*, 171(1):245–281.

Castanier, M. and Pierre, C. (2002). Using intentional mistuning in the design of turbomachinery rotors. *AIAA Journal*, 40(10):2077–2086.

Cimarelli, A., Franciolini, M., and Crivellini, A. (2021). On the kinematics and dynamics parameters governing the flow in oscillating foils. In *J. Fluids and Structures*, pages 1–20.

Cooper, A. J. and Peake, N. (2000). Trapped acoustic modes in aeroengine intakes with swirling flow. *J. Fluid Mechanics*, 419:151–175.

Corral, R. and Martel, C. (2012). Mistuning effects on flutter margin. In *NATO RTO-EN-AVT-207*.

Courtiade, N. and Ottavy, X. (2013). Study of the acoustic resonance occurring in a multistage high-speed axial compressor. *Proc. Institution of Mechanical Engineers, Part A: J. Power and Energy*, 227(6):654–664.

Cumpsty, N. (2001). Discussion : Rotating instabilities in an axial compressor originating from the fluctuating blade tip vortex (mailach, r., lehmann, i., and vogeler, k., 2001, j. turbomach., 123, no. 3, pp. 453-460),. *J. Turbomach.*, 123(3):461–461.

Cumpsty, N. and Whitehead, D. (1971). The excitation of acoustic resonances by vortex shedding. *J. of Sound and Vibration*, 18(3):353–369.

di Mare, L., Vadati, M., Mueck, B., Smith, N. H., and Birch, N. (2009). Aeroelastic instability of fan blades at high altitudes. In *Proc. ASME Turbo Expo 2009*, pages 1765–1772.

Dodds, J. and Vahdati, M. (2015). Rotating stall observations in a high speed compressor—part i: Experimental study,. *J. Turbomach.*, 137(5):51002–51010.

Eck, M., Rueckert, R., Peitsch, D., and Lehmann, M. (2020). Prestall instability in axial flow compressors. *J. Turbomach.*, 142(7).

Emmons, H. (1955). Compressor surge and stall propagation. *Trans. of the ASME*, 77(4):455–467.

Fiquet, A.-L., Aubert, S., Buffaz, N., Vercoutter, A., and Brandstetter, C. (2021a). Acoustic resonance in an axial multistage compressor leading to non-synchronous blade vibration. *J. Turbomach.*, 143(9):91014.

Fiquet, A.-L., Aubert, S., Buffaz, N., Vercoutter, A., and Brandstetter, C. (2021b). Non-synchronous forced respones due to trapped acoustic modes in an axial multistage compressor. In *Proc. 14th European Conference on Turbomachinery Fluid dynamics and Thermodynamics, ETC2021-522*.

Fiquet, A.-L., Brandstetter, C., Aubert, S., and Philit, M. (2019). Non-synchronous aeroacoustic interaction in an axial multi-stage compressor. *J. Turbomach.*, 141(10):101013.

Franke, D. and Juengst, M. (2020). Influence of pre-swirl, rotor speed and blade count on aeroelastic coupling mechanisms during stall inception of a transonic compressor. In *Proc. the ASME Turbo Expo 2020: Turbomachinery Technical Conference and Exposition.*

Furukawa, M., Inoue, M., Saiki, K., and Yamada, K. (1999). The role of tip leakage vortex breakdown in compressor rotor aerodynamics. *J. Turbomach.*, 121(3):469–480.

Goerke, D., Le Denmat, A.-L., Schmidt, T., Kocian, F., and Nicke, E. (2012). Aerodynamic and mechanical optimization of cf/peek blades of a counter rotating fan. In *Proc. ASME Turbo Expo 2012*, pages 21–33.

Graftieaux, L., Michard, M., and Grosjean, N. (2001). Combining piv, pod and vortex identification algorithms for the study of unsteady turbulent swirling flows. *Meas. Sci. Technol.*, 12(9):1422.

Graham, R. and Guentert, E. (1965). Compressor stall and blade vibration. In *NASA Technical Report ID 19650013755.*

Grondin, J. (2019). Analysis of the aerodynamic instabilities and restabilization of a centrifugal impeller at partial regime. *PhD Thesis, Ecole Centrale de Lyon, http://www.theses.fr/2019LYSEC019.*

Hellmich, B. and Seume, J. R. (2008). Causes of acoustic resonance in a high-speed axial compressor. *J. Turbomach.*, 130(3).

Hill, G., Gambel, J., Schneider, J., and Stapelfeldt, S. (2021). Aeroelastic stability of combined plunge-pitch mode shapes in a linear compressor cascade. In *Proc. of 14th European Conference on Turbomachinery Fluid dynamics and Thermodynamics, ETC2021-618.*

Horcas, S. G., Barlas, T., Zahle, F., and Sorensen, N. (2020). Vortex induced vibrations of wind turbine blades: Influence of the tip geometry. *Physics of Fluids*, 32(6).

Inoue, M., Kuroumaru, M., Tanino, T., and Furukawa, M. (2000). Propagation of multiple short-length-scale stall cells in an axial compressor rotor. *J. Turbomach.*, 122(1):45–54.

Kameier, F. and Neise, W. (1997). Rotating blade flow instability as a source of noise in axial turbomachines. *J. Sound Vib.*, 203(5):833–853.

Kielb, R. E., Barter, J. W., Thomas, J. P., and Hall, K. C. (2003). Blade excitation by aerodynamic instabilities: A compressor blade study. In *Proc. ASME Turbo Expo 2003*, pages 399–406.

Kielb, R. E., Feiner, D., Griffin, J. H., and Mizakozawa, T. (2007). The effect of unsteady aerodynamic asymmetric perturbations on flutter. In *Proc. ASME Turbo Expo 2007*, pages 649–654.

Lee, K.-B., Wilson, M., and Vahdati, M. (2017). Numerical study on aeroelastic instability for a low-speed fan. *J. Turbomach.*, 139(7).

Livva, J., Davenport, F., Gray, L., and Walton, I. (1968). Two-dimensional tests of aerofoils oscillating near stall. In *U.S. Army Aviation Material Laboratories.*

Lu, Y., Green, J., Stapelfeldt, S., and Vahdati, M. (2019a). Effect of geometric variability on running shape and performance of a transonic fan. *J. Turbomach.*, page 101012.

Lu, Y., Lad, B., Green, J., Stapelfeldt, S., and Vahdati, M. (2019b). Effect of geometry variability on transonic fan blade untwist. *Int. J. Turbomach., Propulsion and Power*, 4(3):24.

Maerz, J., Hah, C., and Neise, W. (2002). An experimental and numerical investigation into the mechanisms of rotating instability. *J. Turbomach.*, 124(3):367–374.

Mailach, R., Lehmann, I., and Vogeler, K. (2001). Rotating instabilities in an axial compressor originating from the fluctuating blade tip vortex. *J. Turbomach.*, 123(3):453–460.

Malzacher, L., Schwarze, C., Motta, V., and Peitsch, D. (2019). Experimental investigation of an aerodynamically mistuned oscillating compressor cascade. *J. Turbomach.*, 141(7).

Mattis, M. (2019). Study on dynamic stall on compressor blades. In *MSc Thesis, Ecole Centrale de Lyon, RWTH Aachen*.

Miles, J. (1944). The reflection of sound due to a change in cross section of a circular tube. *J. Acoustical Society of America*, 16(14).

Moore, F. (1984). A theory of rotating stall of multistage axial compressors: Part i–small disturbances. *J. Eng. Gas Turbines Power*, 106(2):313–320.

Moore, F. and Greitzer, E. (1986). A theory of post-stall transients in axial compression systems: Part i–development of equations. *J. Eng. Gas Turbines Power*, 108(1):68–76.

Pages, V., Duquesne, P., Ottavy, X., Ferrand, P., Aubert, S., Blanc, L., and Brandstetter, C. (2021). Uhbr open-test-case fan ecl5/catana, part 2 : Mechanical and aeroelastic stability analysis. In *Proc. 14th European Conference on Turbomachinery Fluid dynamics and Thermodynamics, ETC2021-625*.

Parker, R. and Stoneman, S. A. T. (1989). The excitation and consequences of acoustic resonances in enclosed fluid flow around solid bodies. *Proc. Institution of Mechanical Engineers, Part C: Mechanical Engineering Science*, 203(1):43709.

Passrucker, H., Engber, M., Kablitz, S., and Hennecke, D. K. (2003). Effect of forward sweep in a transonic compressor rotor,. In *Proc. Institution of Mechanical Engineers, Part A: J. Power and Energy*, pages 357–365.

Pullan, G., Young, A. M., Day, I. J., Greitzer, E. M., and Spakovszky, Z. S. (2015). Origins and structure of spike-type rotating stall. *J. Turbomach.*, 137(5):51007–51011.

Reiber, C. and Blocher, M. (2017). Potential of aeroelastic tailoring to improve flutter stability of turbomachinery compressor blades. In *Proc. 12th European Conference on Turbomachinery Fluid dynamics and Thermodynamics*.

Rendu, Q. (2016). Modelling of transonic separated flows for fluid-structure interaction studies. *PhD Thesis, Ecole Centrale de Lyon, http://www.theses.fr/2016LYSE1328*.

Rendu, Q., Aubert, S., and Ferrand, P. (2020). Numerical identification of mechanisms triggering 2d choke flutter in transonic fan. *J. of Fluids and Structures*, 97:102879.

Rodrigues, M., Soulat, L., Paoletti, B., Ottavy, X., and Brandstetter, C. (2021). Aerodynamic investigation of a composite low-speed fan for uhbr application. *J. Turbomach.*, 143(10):101004.

Schlechtriem, S. and Loetzerich, M. (1997). Breakdown of tip leakage vortices in compressors at flow conditions close to stall. In *Proc. ASME Turbo Expo 1997, GT-1997-41*.

Schmid, T., T., L.-K., Schidt, T., and Nicke, E. (2019). Optimization of a carbon-fiber composite blade of a counter-rotating fan for aircraft engines. In *Proc. 13th European Conference on Turbomachinery Fluid dynamics and Thermodynamics*.

Srinivasan, V. A. (1980). Influence of mistuning on blade torsional flutter. In *NASA CR-165137(1)*.

Stapelfeldt, S. and Brandstetter, C. (2020). Non-synchronous vibration in axial compressors: Lock-in mechanism and semi-analytical model. *J. Sound and Vibration*, 488:115649.

Stapelfeldt, S. and Brandstetter, C. (2021). Suppression of non-synchronous-vibration through intentional aerodynamic and structural mistuning. *J. Turbomach.*

Theodorsen, T. (1949). General theory of aerodynamic instability and the mechanism of flutter. *NACA Technical Report 496*.

Thomassin, J., Vo, H. D., and Mureithi, N. W. (2011). The tip clearance flow resonance behind axial compressor nonsynchronous vibration. *J. Turbomach.*, 133(4):41030.

Tryfonidis, M., Etchevers, O., Paduano, J., Epstein, A., and Hendricks, G. (1995). Pre-stall behaviour of several high-speed compressors. *J. Turbomach.*, 117(1):62–80.

Tyler, J. M. and Sofrin, T. G. (1962). Axial flow compressor noise studies. *SAE Transactions*, 70:620532.

Vahdati, M. and Cumpsty, N. (2016). Aeroelastic instability in transonic fans. *J. Eng. Gas Turbines and Power*, 138(2):22604.

Vo, H. D., Tan, C. S., and Greitzer, E. M. (2008). Criteria for spike initiated rotating stall. *J. Turbomach.*, 130(1):11023–11029.

Wilson, M. J., Imregun, M., and Sayma, A. I. (2006). The effect of stagger variability in gas turbine fan assemblies. *J. Turbomach.*, 129(2):404–411.

Yamada, K., Kikuta, H., Iwakiri, K.-i., Furukawa, M., and Gunjishima, S. (2013). An explanation for flow features of spike-type stall inception in an axial compressor rotor. *J. Turbomach.*, 135(2):21023.

Young, A., Day, I., and Pullan, G. (2012). Stall warning by blade pressure signature analysis. *J. Turbomach.*, 135(1):11033.

Zhao, F., Dodds, J., and Vahdati, M. (2018). Poststall behavior of a multistage high speed compressor at off-design conditions. *J. Turbomach.*, 140(12).

Zhao, F., Dodds, J., and Vahdati, M. (2020). Influence of blade vibration on part-span rotating stall. *J. Glob. Power Propuls. Soc*, 4:285–295.